

Level Set Segmentation of Retinal Structures

Submitted by

Chuang Wang

for the degree of Doctor of Philosophy

of the

Department of Computer Science
Brunel University London

April 2016

Declaration

I hereby declare that this thesis is solely completed by the candidate, Chuang Wang. The original research work has not been presented for the award of any other degree in the past. Some work in it has been published previously and that is stated in the text where relevant. All sources of material have been properly acknowledged and references have been provided.

List of Publications

Part of the work included in this thesis has been previously published in the following papers:

1. Chuang Wang, Yaxing Wang and Yongmin Li “Automatic Choroidal Layer Segmentation Using Markov Random Field And Level Set Method.”, (under review).
2. Chuang Wang and Yongmin Li “Blood Vessel Segmentation from Retinal Images Using the Level Set Method.” (under review).
3. Chuang Wang, Djibril Kaba and Yongmin Li “Level Set Segmentation of Optic Discs from Retinal Images.” *Journal of Medical and Bioengineering*, Vol. 4, No. 3, pp. 213-220, June 2015.
4. Chuang Wang, Yaxing Wang, Djibril Kaba, Zidong Wang, Xiaohui Liu and Yongmin Li, “Automated Layer Segmentation of 3D Macular Images Using Hybrid Methods.” *The 8th International Conference on Image and Graphics (ICIG)*. Springer International Publishing, 2015, 614-628.
5. Chuang Wang, Yaxing Wang, Djibril Kaba, Haogang Zhu, Zidong Wang, Xiaohui Liu and Yongmin Li “Segmentation of Intra-retinal Layers in 3D Optic Nerve Head Images.” *The 8th International Conference on Image and Graphics (ICIG)*, Springer International Publishing, 2015, 321-332.
6. Chuang Wang, Djibril Kaba and Yongmin Li “Level Set Segmentation of Optic

Discs from Retinal Images.” International Conference on Biomedical and Bioinformatics Engineering (ICBBE 2014).

The author of this thesis has also published the following papers during the PhD period, but the contents are not included in this thesis:

1. Djibril Kaba, Yaxing Wang, Chuang Wang, Yongmin Li, Xiaohui Liu, Haogang Zhu and Ana G. Salazar-Gonzalez “Retina Layer Segmentation Using Kernel Graph Cuts and Continuous Max-Flow.” *Optics Express*, 2015, 23(6): 7366-7584.
2. Djibril Kaba, Chuang Wang, Yongmin Li, Ana Salazar-Gonzalez, Xiaohui Liu, and Ahmed Serag. “Retinal blood vessels extraction using probabilistic modelling.” *Health Information Science and Systems*, 2, no. 1 (2014): 2.

To my parents and brother

Abstract

Changes in retinal structure are related to different eye diseases. Various retinal imaging techniques, such as fundus imaging and optical coherence tomography (OCT) imaging modalities, have been developed for non-intrusive ophthalmology diagnoses according to the vasculature changes. However, it is time consuming or even impossible for ophthalmologists to manually label all the retinal structures from fundus images and OCT images. Therefore, computer aided diagnosis system for retinal imaging plays an important role in the assessment of ophthalmologic diseases and cardiovascular disorders. The aim of this PhD thesis is to develop segmentation methods to extract clinically useful information from these retinal images, which are acquired from different imaging modalities. In other words, we built the segmentation methods to extract important structures from both 2D fundus images and 3D OCT images.

In the first part of my PhD project, two novel level set based methods were proposed for detecting the blood vessels and optic discs from fundus images. The first one integrates Chan-Vese's energy minimizing active contour method with the edge constraint term and Gaussian Mixture Model based term for blood vessels segmentation, while the second method combines the edge constraint term, the distance regularisation term and the shape-prior term for locating the optic disc. Both methods include the pre-processing stage, used for removing noise and enhancing the contrast between the object and the background.

Three automated layer segmentation methods were built for segmenting intra-retinal layers from 3D OCT macular and optic nerve head images in the second part of my PhD project. The first two methods combine different methods according to the data characteristics. First, eight boundaries of the intra-retinal layers were detected from the 3D OCT macular images and the thickness maps of the seven layers were produced. Second, four boundaries of the intra-retinal layers were located from 3D optic nerve head images and the thickness maps of the Retinal Nerve Fiber Layer (RNFL) were plotted. Finally, the choroidal layer segmentation method based on the Level Set

framework was designed, which embedded with the distance regularisation term, edge constraint term and Markov Random Field modelled region term. The thickness map of the choroidal layer was calculated and shown.

Acknowledgement

I would like to thank my supervisor, Dr. Yongmin Li (Brunel University), for the guidance, support and patience throughout my PhD research and also appreciate his encouragement and carefulness while editing my papers. I could not finish my PhD on time without his guidance. I would also like to thank Djibril Kaba, Nick Rixon and Martin for proofreading drafts and providing suggestions and support. I would also like to thank the Department of Computer Science of Brunel University London for the funding of my research project.

Special thanks go to all the members of my PhD jury, Professor Steve Maybank (Department of Computer Science and Information Systems, Birkbeck, University of London), Dr. George Ghinea (Department of Computer Science, Brunel University) and Dr. Panos Louvieris (Department of Computer Science, Brunel University) who managed to take time off their busy schedules; go to all the lab members of Intelligent Data Analysis (IDA) group of the Department of Computer Science including Valeria Bo, Neda Trifonova, Moshina Ferdous, Miqing Li, Liang Hu, Izaz Rahman, Khalid Eltayef, Azerikatoa Ayoung, Hafedh Alrahbi and Almed Al-Madi, for friendship, interesting discussions and valuable comments through my PhD study.

Sincere thanks go to J.J. Staal and A. Hoover for publishing their retinal photographs publicly; go to Dr. Yaxing Wang (Tongren Hospital, Beijing, China) and Haogang Zhu (Department of Optometry and Visual Science, City University, London, United Kingdom) for advices and providing the 3D retinal data both on macular and optic nerve head area. It is impossible to finish the work in the thesis without the data from these different institutes. I would like to thank Chunming Li et al. for providing the source code of the level set method, Quan Wang et al. for providing the source of the Markov Random Field method and Yuan Jing et al for providing the source of the continuous max-flow algorithm

Finally, a deep thanks to my parents, brother, sister-in-law (Xiaofeng Wang, Chungxia Huang, Qiang Wang and Peiqi Liao) and all the other relatives in my big family in China

for their support and understanding during my "PhD Journey".

Contents

1	Introduction	1
1.1	Retinal Structure Analysis	1
1.2	Aims and Objectives	5
1.3	Thesis Overview	6
2	Background	9
2.1	Eye Anatomy	9
2.2	Retinal Imaging Techniques	13
2.2.1	Fundus Imaging	14
2.2.2	Optical Coherence Tomography (OCT) Imaging	18
2.3	Retinal Diseases	27
2.3.1	Glaucoma	27
2.3.2	Diabetes	29
2.3.3	Age-Related Macular Degeneration (AMD)	31
2.3.4	Cardiovascular Diseases (CVD)	33
2.4	Level Set Method	35
2.4.1	Region Based Model	35
2.4.2	Edge Based Model	37
2.5	Retinal Image Analysis	40
2.5.1	Fundus Image Analysis	40
2.5.2	OCT Image Analysis	42

3 Bayesian Level Set Method Based Retinal Blood Vessels Segmentation	45
3.1 Introduction	46
3.2 Methods	48
3.2.1 Pre-processing	49
3.2.2 Hybrid region terms based segmentation	51
3.2.3 Post-processing	55
3.3 Results	55
3.3.1 Performance of blood vessel segmentation	58
3.4 Conclusions	62
4 Level Set Segmentation of Optic Discs from Retinal Images	64
4.1 Introduction	65
4.2 Optic disc centre detection	67
4.3 Optic Disc Extraction	69
4.3.1 Shape prior Term	71
4.3.2 Distance Regularisation Term	71
4.3.3 Energy minimisation	72
4.4 Experimental Results	73
4.4.1 Dataset	73
4.4.2 Performance measures	74
4.4.3 Results	76
4.5 Conclusions	77
5 Automated Layer Segmentation of 3D Macular Images	81
5.1 Introduction	82
5.2 Methods	85
5.2.1 Preprocessing	86
5.2.2 Vitreous and choroid boundaries segmentation	87

5.2.3	NFL, GCL-IPL, INL, OPL, ONL-IS, OS, RPE (See Page xx)	
	boundaries segmentation	88
5.3	Experiments	93
5.3.1	Results	93
5.4	Conclusions	98
6	Segmentation of Intra-retinal Layers in Optic Nerve Head Images	101
6.1	Introduction	102
6.2	Method	103
6.2.1	RNFL and RPE layers segmentation	104
6.3	Experiments	107
6.4	Conclusions	111
7	Automatic Choroidal Layer Segmentation Using Level Set Method	114
7.1	Introduction	115
7.2	Methods	119
7.2.1	Pre-processing step	119
7.2.2	Level Set Method	120
7.2.3	Partial Differential Equation based Energy Minimisation	124
7.3	Experiments	126
7.4	Conclusions	131
8	Conclusions and Future Work	133
8.1	Retinal Structures Extraction from Fundus Images	134
8.2	Retinal Structures Extraction from OCT images	136
8.3	Contributions of the Project	140
8.4	Comparison of Proposed Methods	142
8.5	Limitations and Future Work	145
	Bibliography	147

List of Figures

1.1	The overview of my Ph.D. Work.	4
2.1	Schematic diagram of the cross-sectional view of eye and its major structures copied from [eye, 2015]. The retina and choroid are the yellow tissue and reddish tissues with blood vessels inside, respectively.	10
2.2	Photograph of retina structures: blood vessels, optic disc, optic cup, macula and fovea	11
2.3	Illustration of ten cellular layers of the retina from Berne [Berne et al., 2008].	12
2.4	First human fundus image drawn by Van Trigt in 1853 [Van Trigt, 1853].	15
2.5	Three different angle views of fundus images [Saine and Tyler, 2002]. . .	16
2.6	Some example images obtained from different fundus imaging techniques. (A)Fluorescein Angiogram, (B) Scanning Laser Ophthalmoscopy, (C) Colour Fundus Photography, (D) Red-Free Photography, (E) Two retinal images taken from two different viewpoints for Stereo Fundus Photography.	17
2.7	OCT scanner system schematic [Kraus et al., 2012]. Left: A-scan. Backscattered intensity along the axial direction is measured and formed a single depth profile. Middle: B-scan. The OCT beam is measured in transverse direction. Right: Volumetric image. Multiple B-scans are acquired and formed into a 3D volumetric image.	19

2.8	The setup of the time domain OCT (TD-OCT) imaging system [Schuman, 2008].	20
2.9	The setup of the spectral domain OCT (SD-OCT) imaging system [Schuman, 2008].	22
2.10	The SD-OCT example images captured by using the RTVue-100 system around the ONH area.	23
2.11	The SD-OCT example images taken by using the Spectralis HRA+OCT system around the macular area.	24
2.12	The SD-OCT example images taken by using the Spectralis HRA+OCT system around the ONH area.	25
2.13	The setup of the swept source OCT (SS-OCT) imaging system [Schuman, 2008].	26
2.14	Glaucomatous damage shown on fundus images [Gao et al., 2015]. (A) Healthy fundus example, (B) Angle-closure Glaucoma fundus example, (C) Open-angle Glaucoma fundus example.	28
2.15	Some examples of fundus images which are affected by diabetes retinopathy, including exudates, cotton-wool and drusen [Niemeijer et al., 2007].	30
2.16	Some examples of AMD damage shown on B-scan macula and fundus images [mac, 2015]. (A) Dry AMD example for both B-scan macular and fundus images, (B) Wet AMD example both on B-scan macula and fundus images.	32
3.1	Block diagram of the proposed blood vessel segmentation method. (a) The original retinal image. (b) The grey level image (I_g) of the original image. (c) The closing operation of I_g (I_c). (d) The difference image I_d is obtained from the absolute difference between I_g and I_c . (e) The matched filtering response of I_d (I_m). (f) Final output of the proposed method.	49

3.2	The DRIVE dataset: (a, d) Retinal images. (b, e) Our segmentation results. and (c, f) Ground truth image.	60
3.3	The STARE dataset (Normal): (a, d) Retinal images. (b, e) Our segmentation results. and (c, f) Ground truth images.	60
3.4	The STARE dataset (Abnormal): (a, d) Retinal images. (b, e) Our segmentation results. and (c, f) Ground truth images.	61
4.1	The process to locate the optic disc centre. (a) Rescaled image. (b) The I channel image. (c) Closing operation of I channel. (d) The template with the size of 201×201 . (e) The Fourier correlated image. (f) The mask of rescaled image. (g) The border eroded image. (h) The convoluted image. (i) The optic disc centre located image. (j) The cropped image from F_r with the size of 201×201 . (k) The blood vessel segmented image. (l) Open operation of vessel segmented image. (m) The optic disc centre reseted image.	68
4.2	Morphological close operation on the cropped retinal images. The first row contains the input images, the second row contains the closed images.	70
4.3	The DRIVE dataset: (a, d, g, j) The cropped retinal images. (b, e, h, k) The optic disc centre reseted images. (c, f, i, l) Our segmentation results (Red is our segmentation result, blue is the ground truth).	79
4.4	The DIARETDB1 dataset: (a, d, g, j) The cropped retinal images. (b, e, h, k) The optic disc centre reseted images. (c, f, i, l) Our segmentation results (Red is our segmentation result, blue is the ground truth). . . .	79
4.5	The DIARETDB0 dataset: (a, d, g, j) The cropped retinal images. (b, e, h, k) The optic disc centre reseted images. (c, f, i, l) Our segmentation results (Red is our segmentation result, blue is the ground truth). . . .	79

5.1	Block diagram of retinal layers segmentation process. (NFL: Nerve Fiber Layer, GCL: Ganglion Cell Layer, IPL: Inner Plexiform Layer, INL: Inner Nuclear Layer, OPL: Outer Plexiform Layer, ONL: Outer Nuclear Layer, IS: Inner Segment, OS: Outer Segment, RPE: Retinal Pigment Epithelium)	85
5.2	a) Original 3D macular image. b) The filtered image by nonlinear anisotropic diffusion. c) The filtered image by ellipsoidal averaging. . .	86
5.3	a) The de-noised 3D macular image. b) The segmented object image. c) The lower part of the segmented image across the IS boundary. d) The upper part of the segmented image across the IS boundary.	89
5.4	a) Graph construction for continuous max-flow and min cut with two labels; b) Graph construction for max-flow and min-cut with n labels. .	90
5.5	Illustration of eight intra-retinal layers segmented result on an example B-scan from top to bottom: 1. Vitreous, 2. NFL, 3. GCL-IPL, 4. INL, 5. OPL, 6.ONL-IS, 7. OS, 8. RPE, 9. Choroid.	96
5.6	Three examples of 3D visualisation of eight surfaces.	97
5.7	Twelve B-scan segmentation results from an example 3D segmented macular, (a)-(m) are 10th, 30th, 50th, 70th, 90th, 110th, 130th, 150th, 170th, 190th, 210th, 230th B-scans, respectively.	98
5.8	Examples of thickness maps of 7 retinal layers, layers exclude choroid layer and total layers. The seven layers are 1. NFL, 2. GCL-IPL, 3. INL, 4.OPL, 5.ONL-IS, 6. OS, 7. RPE	99
6.1	Block diagram of retinal layers segmentation process for 3D optic nerve head images.	103

6.2	Illustration of three intra-retinal layers segmented results of two cross-sectional B-scans from a 3D OCT optic nerve head image. (a) the 60th B-scan, which includes the optic disc region, (b) the 10th B-scan. Layer 1: retinal nerve fiber layer (RNFL), Layer 2 includes Ganglion Cell Layer, Inner Plexiform Layer, Inner Nuclear Layer and Outer Nuclear Layer (GCL, IPL, INL and ONL), Layer 3: retinal pigment epithelium layer (RPE).	109
6.3	Three examples of 3D OCT optic nerve head image layers segmentation results. Four segmented layer surfaces of 3 different 3D images are visualised in 3D. The shape of the surfaces are hypothesised to be related with eye diseases.	110
6.4	Ten B-scan segmentation results from an example 3D segmented optic nerve head image, (a)-(k) are 10th, 20th, 30th, 40th, 50th, 60th, 70th, 80th, 90th, 100th B-scans, respectively. According to the segmentation results on B-scans from the 3D retinal images around the optic nerve head, the efficiency and accuracy of our method are shown.	111
6.5	The thickness maps of retinal nerve fiber layer (RNFL) from two 3D optic nerve head image examples. The RNFL thickness map is useful in discriminating for glaucomatous eyes from normal eyes. (a) a healthy subject (b) a glaucomatous patient.	112
7.1	The challenge of the choroidal layer segmentation. (a) The original macular B-scan. (b) The inhomogeneous texture from the B-scan. (c) The inseparable histogram distribution of the background and object from the B-scan. (d) The ground truth of the B-scan.	117
7.2	Block diagram of automatic choroidal layer segmentation. (a) The original macular OCT image. (b) The de-noised OCT image by using the 3D anisotropic diffusion method. (c) The chopped OCT image.	119

7.3	The segmentation error of the bottom choroidal layer boundary of the dataset. (a) The signed mean and standard deviation(sd) difference between the ground truth and the proposed segmentation results for the bottom choroidal boundary (b) The unsigned mean and sd difference between the ground truth and the proposed segmentation results for the bottom choroidal boundary.	127
7.4	The Dice's coefficient of the choroidal layer between the proposed method and the ground truth.	128
7.5	The mean segmentation error of the bottom choroidal layer boundary of the different methods, including the proposed method (A), GMM and MRF based Level Set Method (LSM) (B), MRF (C), Graph Cut method (D), Canny Edge detection (E), K-means algorithm (F), and Chan-Vese LSM (G). (a) The mean signed mean and standard deviation (sd) difference between the ground truth and the segmentation results (b) The mean unsigned mean and sd difference between the ground truth and the segmentation results.	128
7.6	The mean Dice's coefficient of the choroidal layer between the methods and the ground truth, including the proposed method, GMM and MRF based LSM, MRF, Graph Cut, Canny Edge detection, K-means algorithms, and Chan-Vese LSM.	129
7.7	A choroid layer segmented example. (a)-(l) are the 10th, 30th, 50th, 70th, 90th, 110th, 130th, 150th,170th, 190th, 210th, 230th B-scans with the segmented choroidal bottom boundary marked in red, respectively.	129
7.8	Choroidal thickness map of the choroidal layer from this segmented example.	130
7.9	3D view of the segmented choroidal bottom boundary from this example.	130

List of Tables

3.1	Performance of the segmentation methods on the DRIVE and STARE datasets	57
3.2	Performance of vessel segmentation method on the STARE dataset (normal versus abnormal images)	58
4.1	The optic disc detection performance on the DRIVE, DIARETDB0 and DIARETDB1 datasets.	76
4.2	The optic disc segmentation performance on DRIVE, DIARETDB0 and DIARETDB1 datasets.	78
5.1	Signed and unsigned mean and SD difference between the ground truth and the proposed segmentation results for the eight surfaces, respectively.	94
5.2	Average thickness of the 7 layers and overall of all the 30 volume images, absolute thickness and relative thickness difference between the ground truth and the proposed segmentation results of the 7 layers and overall from all the data.	95
6.1	Signed and unsigned mean and SD difference between the ground truth and the proposed segmentation results for the four surfaces, respectively.	108

List of Abbreviations

OCT	Optical Coherence Tomography.
DR	Diabetes Retinopathy.
AMD	Age-Related Macular Degeneration.
DEM	Diabetic Macular Edema.
CNV	Choroidal Neovascularisation.
DRIVE	Digital Retinal Images for Vessel Extraction.
DIARETDB0	Diabetic Retinopathy Database 0.
DIARETDB1	Diabetic Retinopathy Database 1.
STARE	Structured Analysis of the Retina.
SD-OCT	Spectral Domain Optical Coherence Tomography.
MRF	Markov Random Field.
HMMRF	Hidden Markov Random Field.
LSM	Level Set Method.
EM	Expectation Maximisation.
GMM	Gaussian Mixture Model.
HSI	Hyper-spectral imaging.
SLO	Scanning Laser Ophthalmoscope.
cSLO	confocal Scanning Laser Ophthalmoscope.
TD-OCT	Time Domain Optical Coherence Tomography.
CCD	Charge-coupled device.
ONH	Optic Nerve Head.
SS-OCT	Swept- source Optical Coherence Tomography.
IOP	Intraocular pressure.
CDR	Cup-to-disc ratio.
ALT	Argon Laser Trabeculoplasty.
VEGF	Vascular Endothelial Growth Factor.
AREDS	Age-Related Eye Disease Study.
CVD	Cardiovascular Diseases.
CHD	Coronary Heart Diseases.
NHS	National Health Service.
PAD	Peripheral Arterial Disease.
PVD	Peripheral Vascular Disease.
RHD	Rheumatic Heart Disease.
CHD	Congenital Heart Disease.

DVT	Deep Vein Thrombosis.
k-NN	k Nearest Neighbor.
SDF	Signed Distance Function.
CV	Chan-Vese.
TPR	True Positive Rate.
FPR	False Positive Rate.
ACC	Accuracy Rate.
RNFL	Retinal Nerve Fibre Layer.
FOV	Field of view.
MAD	Mean Absolute Distance.
GCL	Ganglion Cell Layer.
IPL	Inner Plexiform Layer.
INL	Inner Nuclear Layer.
OPL	Outer Plexiform Layer.
ONL	Outer Nuclear Layer.
IS	Inner Segment.
OS	Outer Segment.
REP	Retinal Pigment Epithelium.
WHO	World Health Organisation.
SD	Standare deviation.
FT	Fourier Transformation.
GT	Ground Truth.
MLE	Maximum Likelihood Estimators.
MRI	Magnetic Resonance Image.
PCA	Principle Component Analysis.
RMSE	Root-Mean Square Error.
ROI	Region of Interest.
SVM	Support Vector Machine.

Chapter 1

Introduction

Changes in the retinal structure, such as the area of the optic disc cup and optic disc, the thickness of retinal layers and so on, manifest many important eye diseases as well as systemic diseases, which originate either in the eye, the brain or the cardiovascular system. Much research in retinal structure analysis has been done to diagnose some of the most prevalent ocular diseases including glaucoma, diabetes, diabetic retinopathy, cardiovascular disease and age-related macular degeneration, most of which are common causes of irreversible blindness in the world. It is necessary and important to extract the retinal structure from retinal images, which are acquired from different imaging modalities, to assist the ophthalmologists in diagnosing eye diseases accurately and provide efficient treatment and management systems. In order to understand how retinal diseases affect the retinal structure, retinal structure analysis is introduced in Section 1.1. Section 1.2 introduces the aims of the Ph.D project. Finally, a thesis overview is briefly introduced in Section 1.3.

1.1 Retinal Structure Analysis

Retinal structure analysis has attracted more and more researchers and ophthalmologists over the past 20 years. During this period retinal imaging technology has rapidly

developed and enabled greater visibility of structures behind the retina and choroid. Retinal structure analysis has become an essential part of detecting and diagnosing eye diseases, and preventing loss of sight or blindness. Fundus imaging and optical coherence tomography (OCT) imaging modalities are two of the most widely used imaging systems in clinics and eye hospitals, used to aid ophthalmologists in obtaining a diagnosis. Therefore, we mostly focus on retinal structure analysis using both the fundus images and OCT images.

Fundus imaging is an essential part of diagnosing and treating diabetic retinopathy (DR) and Age-related Macular Degeneration (AMD), which are the two most common forms of vision loss and blindness across the world. Almost all patients diagnosed with diabetes will develop diabetic retinopathy. AMD is the leading causes of vision loss among the elderly. It is non-reversible with undetectable early symptoms and eventually may destroy sharp central vision. As diagnoses of diabetes are increasing and the percentage of the world's elderly population is continuing to rise, both DR and AMD are becoming more serious health problems [Abràmoff et al., 2010]. However, both diseases are manageable with a range of treatments available if patients are examined at least once a year [Ouyang et al., 2013]. The fundus image taken during such an examination is analysed by ophthalmologists for signs of abnormality or further deterioration within the retina area. Based on the data analyse from the fundus images, diagnoses and treatments can be made and prescribed to the patient before the condition can deteriorate beyond a state where it can be managed.

Fundus photography can be used to diagnose other medical conditions in the body [Abràmoff et al., 2010]. Often, cardiovascular conditions such as stroke, myocardial infarction and hypertension can change the structure of the retina, affecting the diameter of retinal arterioles and venules [Wong et al., 2004]. For example, when the ratio of the diameters of arterioles and venules becomes unbalanced, this can indicate an abnormality in the arterioles and venules, which is often associated with myocardial infarction. The ability to view such abnormalities from fundus images by using

some retinal structure analysis tools can help to detect symptoms and diagnose the diseases earlier, enabling proper treatment to prevent deterioration or even non-reversible blindness.

OCT imaging provides more information about the retinal morphology, which makes it possible for this imaging technique to be used for close monitoring of retinal status and guidance of retinal treatment strategies [Abràmoff et al., 2010]. OCT imaging is successfully used as an image guided diagnosis and treatment system in ophthalmology, especially in diabetic macular edema (DME) and choroidal neovascularization. DME is a form of diabetic retinopathy, while choroidal neovascularization (CNV) is the wet form of age related macular degeneration. The DME causes vision loss through fluid leakage into the macula. By using the OCT imaging technology, the thickness of the central retina can be measured and used as an important indicator for diagnosing DME [Murakami and Yoshimura, 2013]. CNV is the creation of new blood vessels in the choroid layer which can rupture and bleed because they are weaker than normal blood vessels. The CNV may produce extreme myopia, myopic degeneration, or age-related developments, which may cause a sudden degeneration of central vision. The parameters of the cystoid spaces, diffuse intra-retinal fluid, sub-retinal fluid, sub-retinal hyper-reflective material, or a change of fluid measured from OCT images is important to indicate CNV [Mokwa et al., 2013].

OCT photography is widely used to diagnose glaucoma, which is the second most common cause of blindness all over the world [Resnikoff et al., 2004]. The structural changes in the optic nerve head and retinal nerve fiber layer are measured from OCT images for early glaucoma diagnosis and aid in providing proper treatment to prevent visual loss. The cup-to-disc ratio calculated from 3D optic nerve head OCT images is an important indicator for glaucoma. The thickness of the retinal nerve fiber layer is calculated for aiding a glaucoma diagnosis.

Retinal structure analysis is increasingly important in clinical applications for assisting ophthalmologists in diagnosing eye diseases, especially during early diagnosis

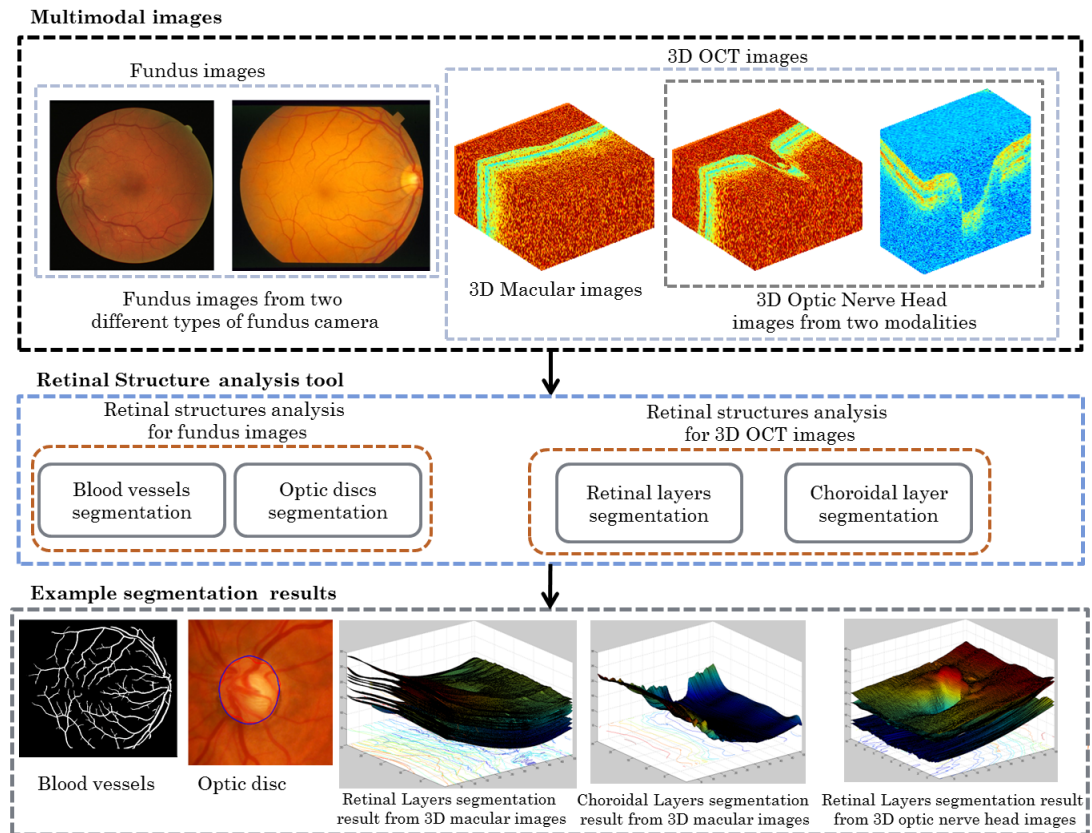


Figure 1.1: The overview of my Ph.D. Work.

and management for eye diseases. The aim of my Ph.D project is to build a structure analysis tool for extracting important retinal structures from both 2D and 3D retinal images, which are obtained from different imaging modalities including fundus cameras and OCT imaging systems, for assisting ophthalmologists in diagnosing eye diseases and providing the proper treatment strategies in advance to prevent serious deterioration. Figure 1.1 shows the framework of this Ph.D project. The first part of this project mainly focused on fundus image analysis to segment out the blood vessels and optic discs. The second part of this project focused on OCT image analysis, and the images involved in this project are acquired from two different imaging modalities and taken around different retinal areas including the optic nerve head area and macular area.

1.2 Aims and Objectives

Retinal imaging technology has developed dramatically during the last few decades. This has enabled ophthalmologists to capture a clearer view of the structure and tissues of the retina or even the choroid. However, it is time consuming or even impossible to hand label all the retinal structures to detect the tiny changes in the captured images. Therefore, the aim of this thesis is to develop retinal image analysis tools for images obtained from different imaging modalities. The tools are used to detect the retinal structure changes and extract useful information, which enable ophthalmologists to precisely diagnose diseases especially in their early stages and give proper treatment to prevent future deterioration.

The specific objectives of the Ph.D. project, as described in this thesis, are summarised as follows:

- **Blood vessels** : Develop an automated segmentation method for extracting blood vessels from retinal images and evaluate the performance of the segmentation using two public datasets DRIVE and STARE.
- **Optic disc** : Develop an automated optic disc segmentation method for retinal images and evaluate the performance of the segmentation method using three public datasets DRIVE, DIARETDB0 and DIARETDB1.
- **Macular** : Develop a fully automated segmentation method for extracting seven intra-retinal layers from 3D macular images and evaluate the performance of this method using a dataset collected from Tongren Hospital, Beijing, China by using the imaging modality SD-OCT Spectralis HRA+OCT (Heidelberg Engineering, Germany).
- **Optic nerve head** : Develop a method for intra-retinal layers segmentation from 3D optic nerve head images and evaluate the performance of the method on images obtained from Moorfield Eye Hospital by using the imaging modality

RTVue-100 SD-OCT (Optovue, Fremont, CA, USA).

- **Choroidal layer** : Develop a method for detecting the choroidal layer from 3D macular images and validate the performance of the method through a dataset from Tongren Hospital by using the imaging modality SD-OCT Spectralis HRA+OCT (Heidelberg Engineering, Germany).

1.3 Thesis Overview

This thesis includes 8 chapters. The rest of the thesis is organised as follows:

- **Chapter 2** provides some relevant background and explains the major challenges of this project. It includes an introduction to the anatomy of the eye. This is followed by a description of the fundus and Optical Coherence Tomography (OCT) imaging techniques. Then, some of the most prevalent retinal diseases including glaucoma, diabetes, diabetes retinopathy, age-related macular degeneration, and cardiovascular disease are discussed. Two classical models of the level set method are discussed. Finally, some major topics and challenges in fundus and OCT image analysis are described.
- **Chapter 3** describes an automated and unsupervised blood vessel segmentation method from fundus images by using the level set method, which combines Chan-Vese's region based term with the Gaussian Mixture term and distance regularisation term. The morphological closing operation and matched filtering are used as a preprocessing process to keep the vessels inside the optic disc, remove the noise of the optic disc boundary, and enhance the blood vessel information. The proposed method is tested and compared with the state-of-the-art methods on two public datasets namely DRIVE and STARE. It achieves an average accuracy greater than 95%.
- **Chapter 4** introduces an automated optic discs segmentation method obtained

from digital fundus images. The template matching method is used to approximately locate the optic disc centre, and the blood vessels are extracted to re-locate the centre of the optic disc. This is followed by applying the level set method, which incorporates the edge term, distance regularization term and shape-prior term, to segment the shape of the optic disc. Seven measurements are used to evaluate and compare the performance of our proposed methods with the state-of-the-art methods on three public datasets: DRIVE, DIARETDB0 and DIARETDB1.

- **Chapter 5** presents an automated segmentation method to detect intra-retinal layers in OCT macular images acquired from a high resolution SD-OCT Spectralis HRA+OCT (Heidelberg Engineering, Germany). The algorithm starts by removing all the OCT imaging artifacts including the speckle noise and enhances the contrast between layers using both 3D nonlinear anisotropic and ellipsoid averaging filters. Eight intra-retinal boundaries of the retina are detected by using a hybrid method which combines the hysteresis thresholding method, level set method, and multi-region continuous max-flow approaches.
- **Chapter 6** introduces an intra-retinal layer segmentation method from SD-OCT images around the optic nerve head acquired from a high resolution RTVue-100 SD-OCT (Optovue, Fremont, CA, USA). This method starts by removing all the OCT imaging artifacts including the speckle noise and enhances the contrast between layers using the 3D nonlinear anisotropic diffusion filter. Afterwards, we combine the level set method, k-means and Hidden Markov Random Field (HMRF) method to segment four surfaces of the retinal images around optical nerve head.
- **Chapter 7** presents a choroidal layer segmentation method from 3D macular images by using the level set method, which adopts the Markov Random Field term with the distance regularisation and edge constraint terms. Before that, the

3D nonlinear anisotropic diffusion filter is used to remove all background noise. The segmented results are compared with the manual segmented cross-sectional B-scans. The experimental results show that our method can accurately estimate the choroidal boundary.

- **Chapter 8** provides conclusions for this Ph.D project in this thesis and highlights some potential future research directions under investigation.

Chapter 2

Background

This chapter describes the background of this Ph.D. project. In order to understand the structure of the eye, Section 2.1 briefly discusses the eye anatomy. Some typical retinal diseases are introduced in Section 2.2. This is followed by a description of the retinal imaging techniques in Section 2.3. A simple discussion of the retinal image analysis is given in Section 2.4. Two famous level set models are introduced in Section 2.5.

2.1 Eye Anatomy

It is important to understand the structure and functions of the eye to help the diagnosis and treatment of eye diseases. The diagram of the cross-sectional view of the eye and its major structures [eye, 2015] is shown in Figure 2.1. The eye works similar to a camera with many parts of the eye working together to produce clear vision. The white part of the eye is called the sclera, which is used to protect the eyeball. The black dot at the centre of the eye through which the light enters the eye is called the pupil. The coloured iris, which is brown, green, blue or a mix of these colours is part of the eye, and surrounds the pupil and adjusts the size of the pupil to control the amount of light entering the eye. The curved shape of the cornea is the “front window” of the

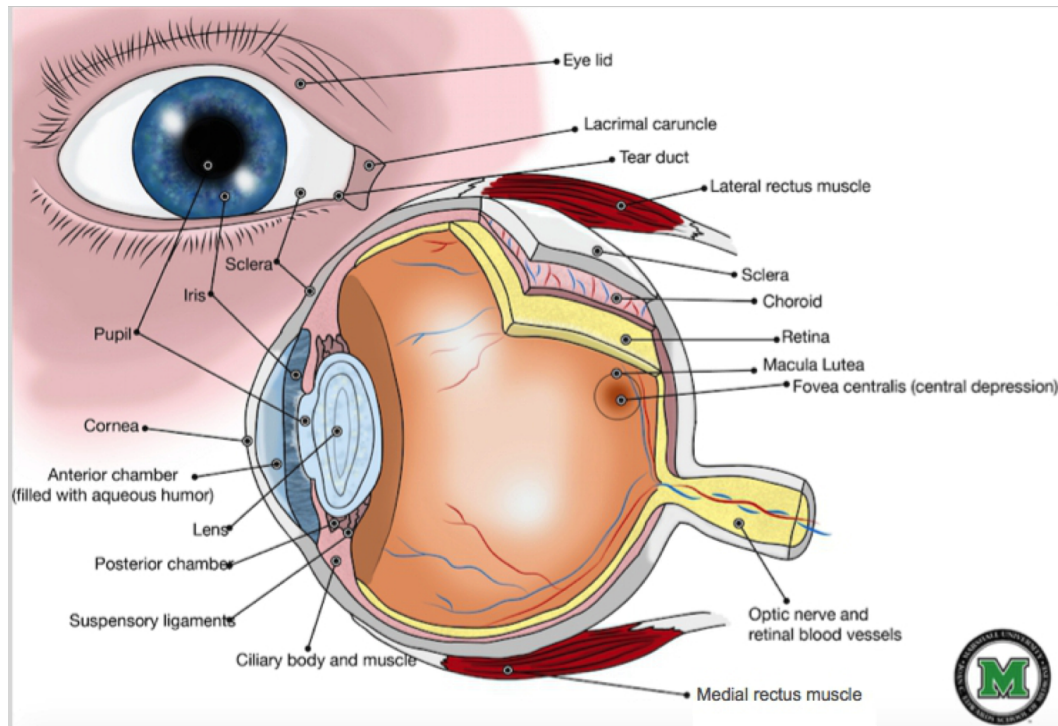


Figure 2.1: Schematic diagram of the cross-sectional view of eye and its major structures copied from [eye, 2015]. The retina and choroid are the yellow tissue and reddish tissues with blood vessels inside, respectively.

eye and transmits and focuses light onto the lens underneath. The curve of the cornea can determine if someone has near or long sight as well as other vision impairments. Corrective laser surgery works by reshaping the cornea to change the focus.

The lens is located behind the pupil and acts similarly to a camera lens by focusing light onto the retina. The retina is the yellow part of the eye and contains two types of photoreceptor: rods and cones. There are approximately 6 million cones within the macula area of the retina and are the most densely spaced together in the Fovea. Cones primarily process light and colour. Rods are positioned in the outer edge of retina and are responsible for sight during low light and peripheral vision. Through the photoreceptor cells, the retina absorbs and converts light to electrical impulses, which are transferred to the brain along the optic nerve. The optic nerve is located in the centre of the retina. The choroid is located between the retina and the sclera and

provides oxygen and nourishment to the retina.

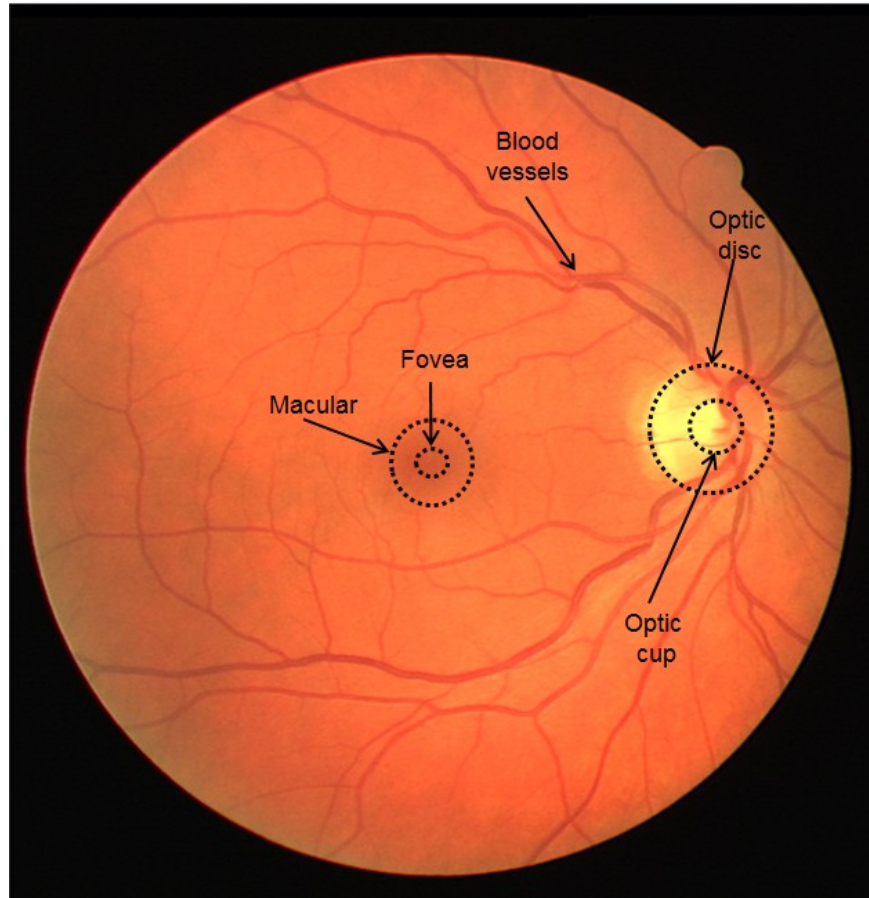


Figure 2.2: Photograph of retina structures: blood vessels, optic disc, optic cup, macula and fovea

Figure 2.2 shows the digital fundus image with retinal structures marked, which includes retinal blood vessels, the optic disc, and macula. The macula area is the dark region located roughly at the centre of the retina, which is responsible for the vision needed for daily activities such as reading and writing. At the centre of the macula is the fovea, which contains the greatest concentration of cone cells in the eye. The fovea is responsible for central, sharp vision and is necessary for reading, driving and other activities. The optic disc is the visible part located at the front of the optic nerve, which is known as the blind spot because it contains no rods and cones. The optic cup is located at the centre of the optic disc. The ratio between the diameter of the optic

cup and the diameter of the optic disc is important in the diagnosis of glaucoma.

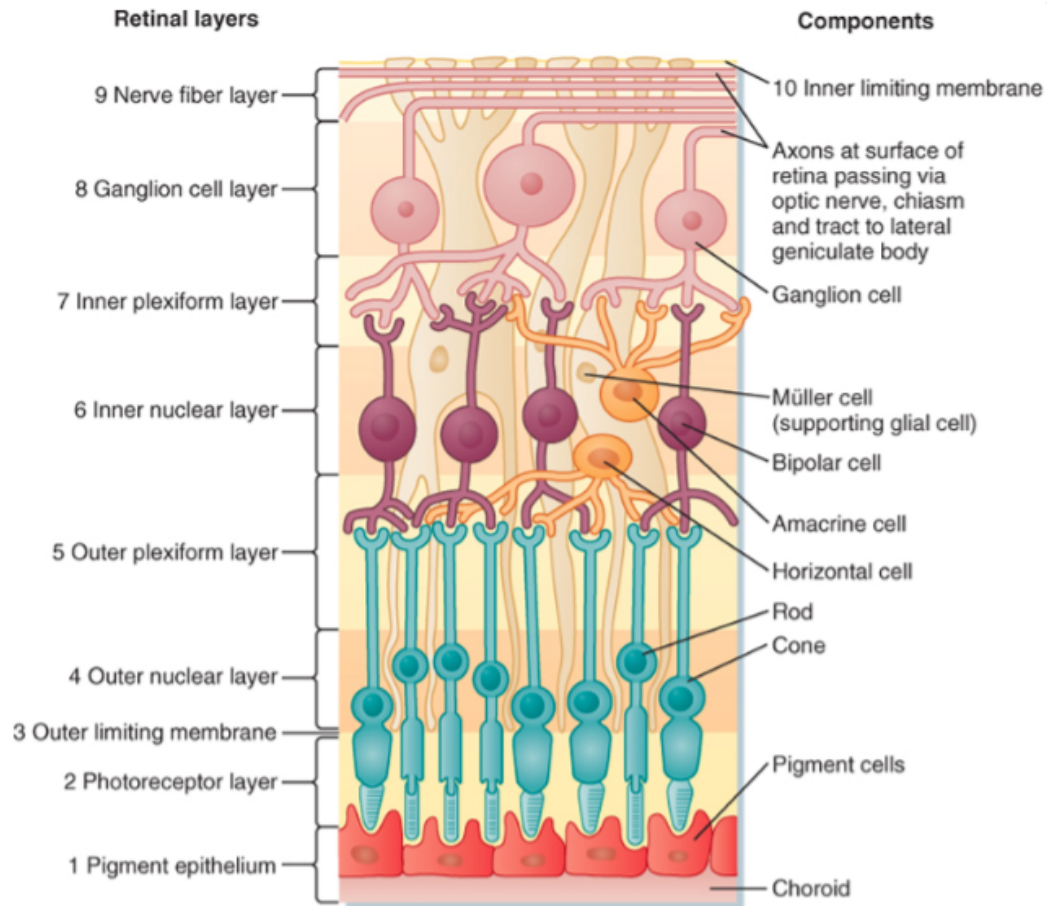


Figure 2.3: Illustration of ten cellular layers of the retina from Berne [Berne et al., 2008].

Ten cellular layers of the retina from [Berne et al., 2008] are illustrated in Figure

2.3. The retina is divided into the following layers:

1. The pigment epithelium: the main function is to maintain the quality of an image through absorbing the stray light and preventing scatter;
2. Photoreceptor layer: composed of photoreceptor (rods and cones), which receive light from a particular part of the visual field;
3. The external limiting membrane: it forms intercellular connections with the photoreceptors, Müller cells and photoreceptors;

4. The outer nuclear layer: it includes the cell bodies of rods and cones;
5. The outer plexiform layer: formed of the synapses between the photoreceptors (rods and cones) and retinal horizontal and bipolar cells;
6. The inner nuclear layer: made up of the nuclei, cell bodies of the horizontal cells, the bipolar cells and Müller cells;
7. The inner plexiform layer: the synaptic formation between the bipolar cells axons and ganglion cells dendrites;
8. The ganglion cell layer: formed by the cell bodies of the ganglion cells;
9. The retinal nerve fibre layer: composed of axons of the ganglion cells, through which the electrical impulses are transmitted to the visual cortex;
10. The inner limiting membrane: it contains the Müller cells and is located within the innermost layer of the retina.

Below the retina is the choroid, which supplies blood to the retina. The structure of the choroid consists of the following layers:

1. The Bruch's membrane: separates the choroid from retina;
2. The choriocapillaris;
3. The Sattler's layer: contains the medium diameter blood vessels;
4. The Haller's layer: composed of larger diameter blood vessels and is located at the outermost layer of the choroid.

2.2 Retinal Imaging Techniques

Retinal imaging is used by optometrists to take pictures of the retina, blood vessels and the optic nerve inside of the eye. These pictures help ophthalmologists to diagnose and

manage eye diseases including glaucoma, diabetes, macular degeneration and so on. This method is a non-invasive imaging technique, which captures a more detailed view of inside of the eye compared to conventional methods. Retinal disorders are detected in their early stages by using retinal imaging techniques. This early detection makes it possible to prevent serious disease progression or even vision loss. Retinal images are captured and stored giving a permanent and historical record of the eye, and make it easier for ophthalmologists to discover minor changes in the eye by comparing images taken over time. Nowadays, retinal imaging modalities, such as fundus photography and optical coherence tomography (OCT) machines, are widely used in clinics. Fundus imaging techniques are widely used to detect eye diseases including diabetic retinopathy, glaucoma, and age-related macular degeneration, while OCT imaging techniques are famous for diagnosing and managing patients with diabetic retinopathy, macular degeneration, and inflammatory retinal diseases [Abràmoff et al., 2010].

2.2.1 Fundus Imaging

The Dutch ophthalmologist Van Trigt drew the first fundus image in 1853 [Van Trigt, 1853] as shown in Figure 2.4. Fundus photography was invented in the 1920's and has been widely used since the 1960's [Gramatikov, 2014]. Fundus photographs are used to detect medical signs, such as hemorrhages exudates, cotton wool spots, blood vessel abnormalities, and pigmentation. Fundus imaging is one of the most widely used imaging tools in clinics.

Fundus photography uses a fundus camera to capture retinal images of the interior surface of the eye. A fundus camera is installed with a low power microscope which provides a magnified view of the retina. A fundus image obtained from the camera provides 2-D representative image of 3-D retina by using reflected light. The typical width of the camera view is from 30 to 50 degrees. The whole imaging process takes around 5 to 10 minutes. Figure 2.5 shows fundus images with three different widths of view: 20, 40, 60 degrees, respectively [Saine and Tyler, 2002].

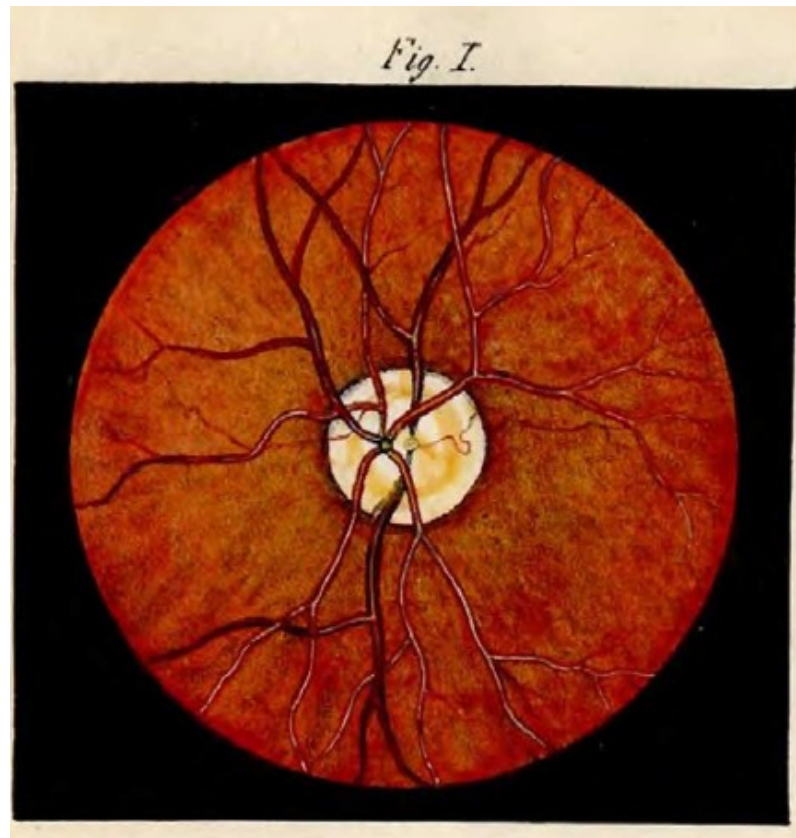


Figure 2.4: First human fundus image drawn by Van Trigt in 1853 [Van Trigt, 1853].

The broad category of fundus imaging contains the following modalities [Abràmoff et al., 2010]:

1. Fundus photography (including red-free photography): A filter is used to select specific colours from the imaging lights to enhance the appearance of specific areas of the retina. Red-free photography is used to highlight the blood vessels by removing the red colour. An example image is shown in Figure 2.6(D).
2. Colour fundus photography: Provides a full colour fundus image, Figure 2.6(C) shows an example of a colour fundus image.
3. Stereo fundus photography: Two images of the same retina are taken from two different viewpoints and fused to obtain a virtual, depth-enhanced stereo image,

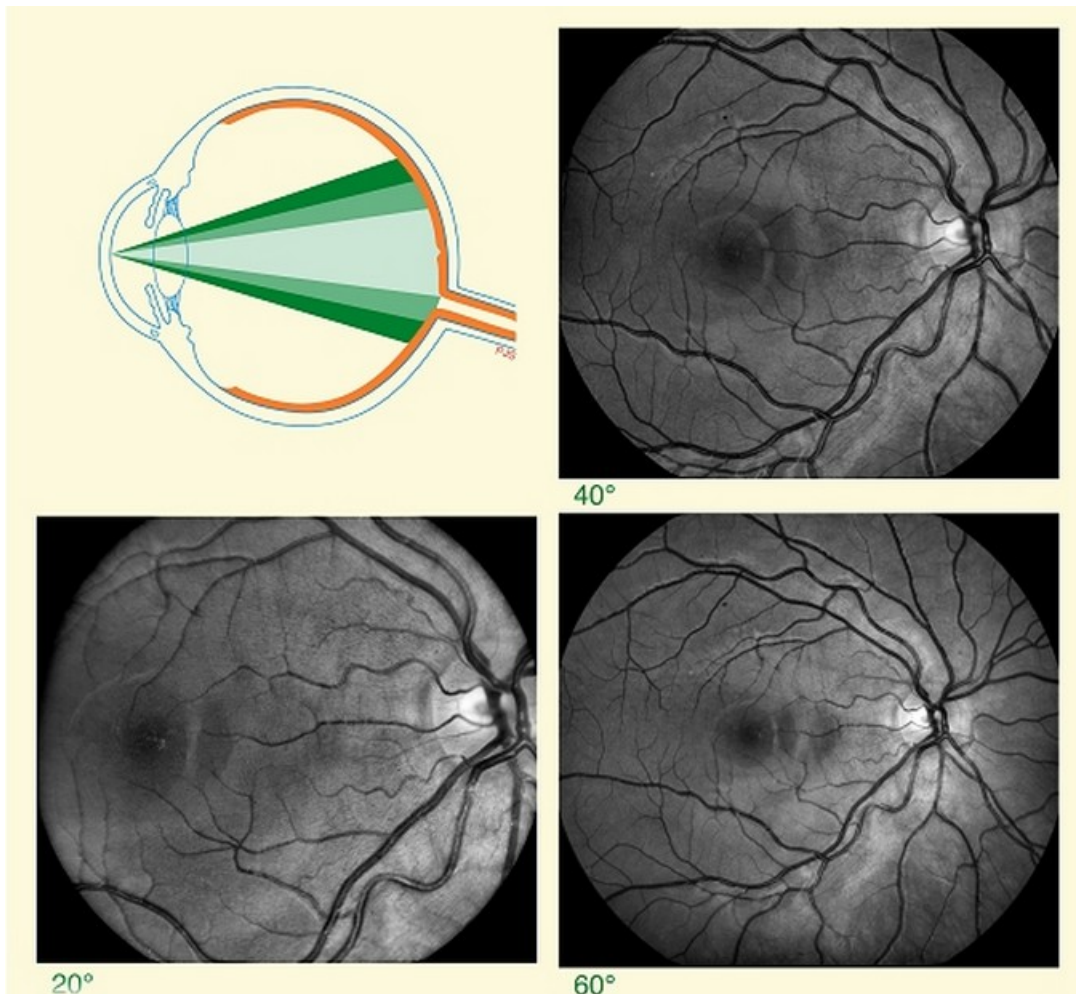


Figure 2.5: Three different angle views of fundus images [Saine and Tyler, 2002].

which helps the physician study the patient's retina more easily and comprehensively. Two retinal images taken from different angles are shown in Figure 2.6(E).

4. Hyper-spectral imaging (HSI): Used to obtain an electromagnetic spectrum for each pixel in the image, which can be used to record subtle variations of spectral properties, for finding objects, identifying materials, or detecting processes. It is widely used for analysing the spectra of inhomogeneous materials that contain a wide range of spectral and spatial information [Park et al., 2006]. The hyper-

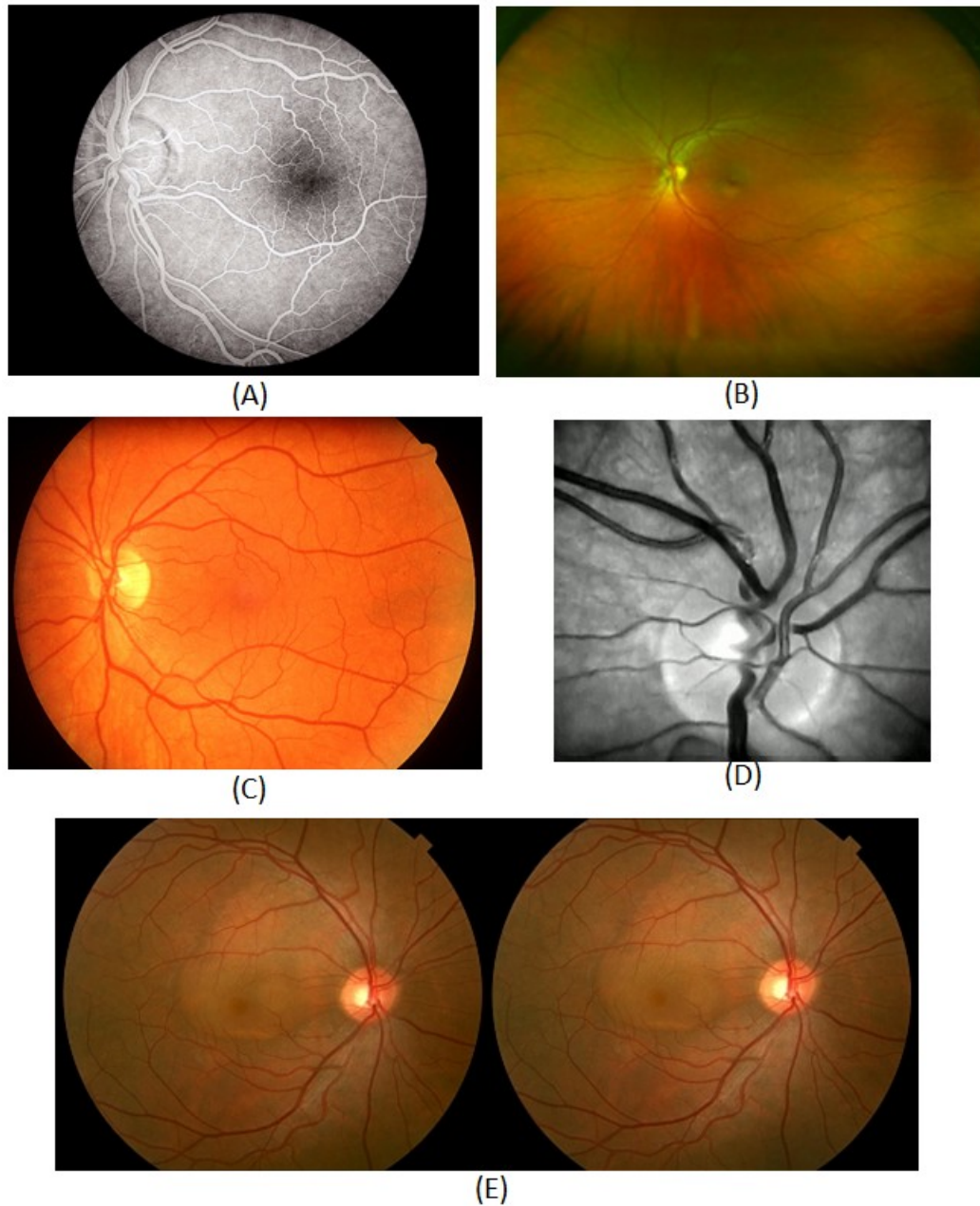


Figure 2.6: Some example images obtained from different fundus imaging techniques. (A)Fluorescein Angiogram, (B) Scanning Laser Ophthalmoscopy, (C) Colour Fundus Photography, (D) Red-Free Photography, (E) Two retinal images taken from two different viewpoints for Stereo Fundus Photography.

spectral camera detects the consumption of the oxygen in the retina, which is used to diagnose diseases including hemorrhagic shock, peripheral artery disease,

diabetes and many other abnormalities [Gramatikov, 2014].

5. Scanning laser ophthalmoscopy (SLO): Provides a high quality television image of any specific area of the retina by utilising horizontal and vertical scanning mirrors. This technique is widely used for diagnosing eye disorders, such as glaucoma, macular degeneration and other retinal pathologies. Figure 2.6(B) shows an example SLO image.
6. Adaptive optics SLO: Used to measure living retinal cellular and sub-cellular structures in the human eye to help diagnose retinal disorders [Huang et al., 2012]. It provides a high resolution image of a specific region of interest on the retina with adaptive optics technology, which is used to reduce the effect of wavefront distortions.
7. Fluorescein angiography: Require the injection of a small amount of dye into a vein at the bend of the elbow. After that, a specialised camera is used for imaging the blood flow in the retina and choroid. Because fluorescein angiography obtains images with high contrast between the blood vessel and background, it can be used to accurately detect and quantify the geometric changes in blood vessels. However, this technique is not available for all patients because of allergic reactions. Fluorescein angiography is normally used for the diagnosis of the eye disorders, such as: macular degeneration, and diabetic retinopathy. An example image of fluorescein angiography is shown in Figure 2.6(A).

2.2.2 Optical Coherence Tomography (OCT) Imaging

OCT is a non-invasive technology used to obtain high resolution, cross-sectional images of the microstructure of the eye. OCT was designed by Fujimoto's group at MIT in 1991 and was first introduced commercially in 1996 [Huang et al., 1991]. OCT uses light to scan in a similar way to an ultrasound scan. An OCT scan generally shows much finer detail than an ultrasound scan. However, ultrasound can be used to scan

deeper into tissue and through structures that are opaque to light [Fujimoto et al., 2000]. OCT is used to see details of the cornea or the retina, while ultrasound is used to see structures hidden by the iris. A near infrared low intensity light is directed into the retina of the patient. The light that is reflected back is captured by the OCT modality's detectors and converted into a high resolution cross-sectional image of the internal microstructure of the retina, displaying the different intra-retinal layers. The different layers of the retina reflect the light back at different frequencies. This allows the different layers to be seen.

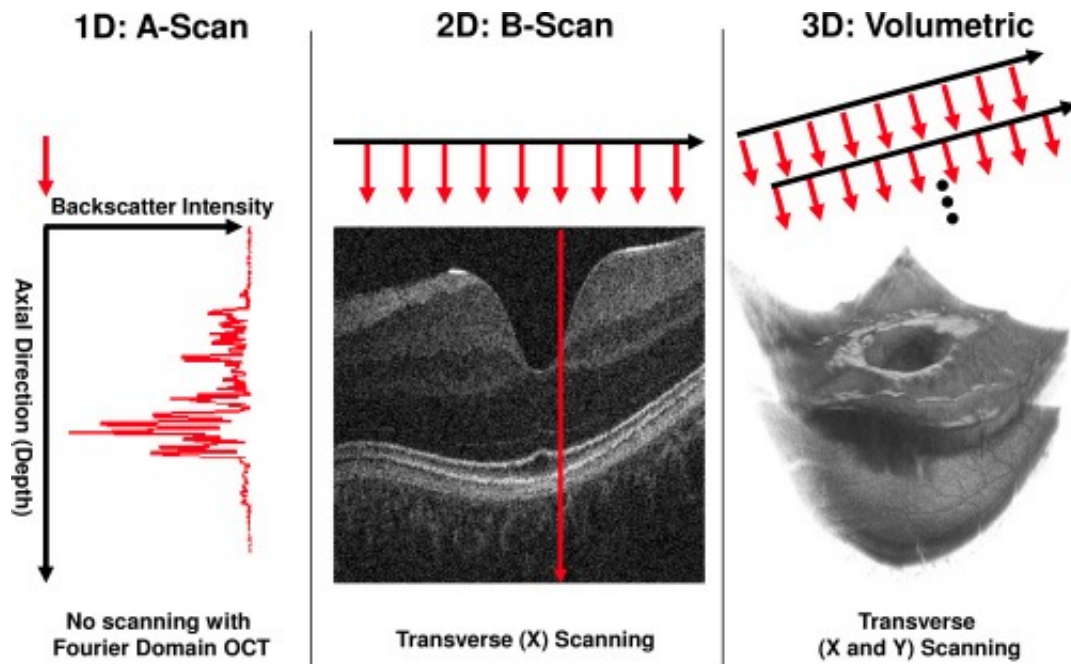


Figure 2.7: OCT scanner system schematic [Kraus et al., 2012]. Left: A-scan. Backscattered intensity along the axial direction is measured and formed a single depth profile. Middle: B-scan. The OCT beam is measured in transverse direction. Right: Volumetric image. Multiple B-scans are acquired and formed into a 3D volumetric image.

This imaging technique has been used to diagnose and manage many retinal disorders including glaucoma, choroidal neovascularization, macular edema, vitreomacular traction and diabetic retinopathy [Jaffe and Caprioli, 2004]. The main advantage of this technique in medical applications is that it is possible to image tissue structure on

site and in real time. There are three main OCT imaging techniques developed to capture cross-sectional or volumetric images of retina. An image scanned along the depth direction of the retina is called A-scan as Figure 2.7 (Left). Several A-scans across the area of the tissue can be collected together and used to create one cross sectional image which is called a B-scan as Figure 2.7 (Middle). A 3D image can be created using a collection of B-scans in parallel Figure 2.7 (Right).

Time-domain OCT (TD-OCT)

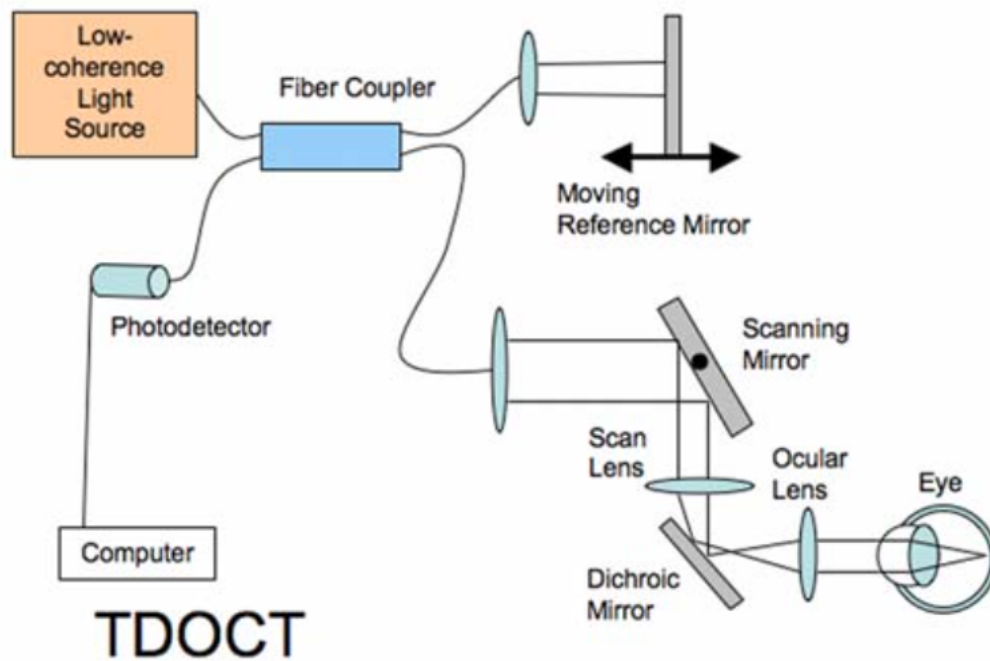


Figure 2.8: The setup of the time domain OCT (TD-OCT) imaging system [Schuman, 2008].

The TD-OCT technique is frequently compared to ultrasound due to the similarity in technique. TD-OCT technique uses the backscattered echo time delay and light intensity levels to create a cross-sectional image. TD-OCT has around $10\mu m$ axial resolution, which is much higher than ultrasound at around $150\mu m$. TD-OCT modality captures around 400 axial scans per second. The traditional OCT method (TD-OCT)

is used to represent the location of each reflection within the position of a moving reference mirror in the time information [Huang et al., 1991]. The StratusOCT (Carl Zeiss Meditec Inc., Dublin, CA, USA) is one of the most widely used TD-OCT devices in clinical applications. It acquires 400 A-scans per second with an axial resolution of $10\ \mu\text{m}$. The highest lateral resolution is up to around $20\ \mu\text{m}$.

Figure 2.8 shows the time-domain OCT (TD-OCT) imaging system setup [Schuman, 2008]. TD-OCT works by shining light from a light source, such as a superluminescent diode (superluminescent diodes operate on a bandwidth of around 20 to 50 nanometers) or a broad bandwidth laser into a beam splitter (fiber coupler). This splits the light into two beams, with one going to the mirror on the reference arm, and one going to the mirror on the sample arm which can be adjusted to localise the depth of scan into the tissue. Some light from the sample arm mirror is reflected back off the eye tissue but most of it scatters away in different angles. Light from the sample and reference mirrors then travels back to the beam splitter. If the sample and reference lights are coherent, meaning that the light depths of the sample and reference mirrors are the same, a combination of both reflections of light produces an interference pattern that is processed by the photodetector to produce an image or an A-scan [Huang et al., 1991]. If the sample and reference light are incoherent, they will not produce an interference pattern that can be converted to an image. It is difficult to precisely image retinal tissue in three dimensions because of eye movement.

Spectral-domain OCT (SD-OCT)

Although fundamentally similar to TD-OCT, SD-OCT has some significant variations. SD-OCT systems are able to scan and perform imaging at a higher speed and scan depth, and are able to take thousands of A-scans a second. Both TD-OCT and SD-OCT use a central wavelength range of approximately 800 to 1100 nm. Figure 2.13 shows a schematic of spectral domain OCT (SD-OCT) imaging system setup. One of the main differences is that the reference mirror is in a fixed position in SD-OCT. The

adjustments of the referencing mirror used in TD-OCT are not efficient and limit in the speed and sensitivity of the scans. It is faster and more efficient to detect reflections from the entire range of depths simultaneously. Therefore, in SD-OCT the reference mirror is kept stationary, and the interference between the sample and reference beams is detected as a spectrum. The interference pattern is split using a grating diffraction into its frequency components and all of these components are simultaneously detected by a charge-coupled device (CCD) camera. The CCD camera is sensitive to several different frequencies.

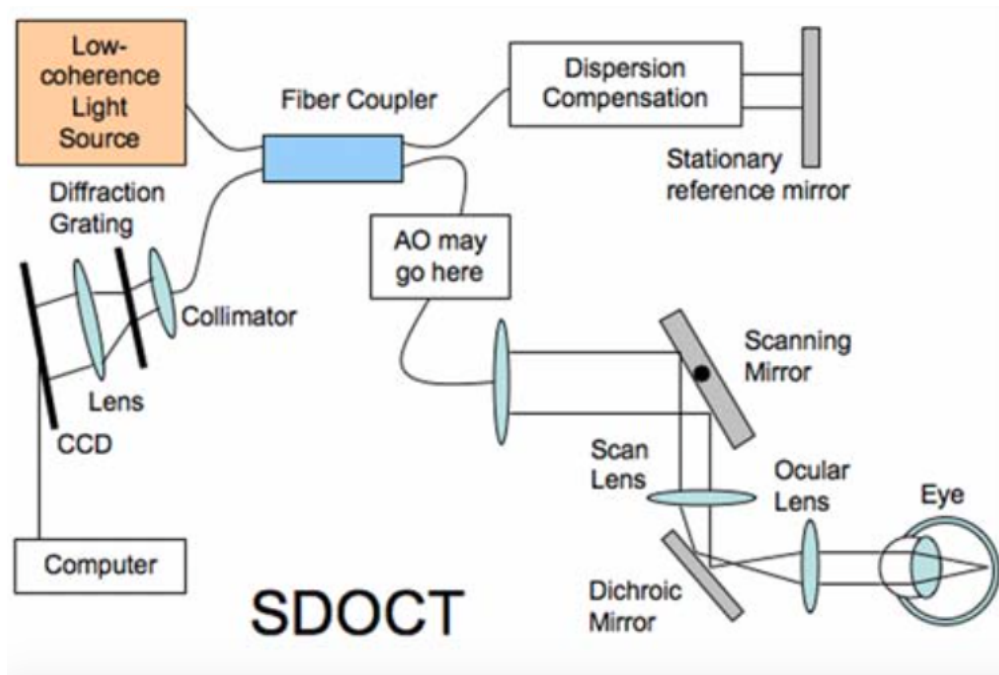


Figure 2.9: The setup of the spectral domain OCT (SD-OCT) imaging system [Schuman, 2008].

SD-OCT machines are up to 40 to 110 times faster than TD-OCT machines [Schuman, 2008]. This faster speed allows for a more rapid capturing of B-scans, and for a higher level of precision when modelling and visualising 3D datasets. However, TD-OCT is only able to reach a maximum of around 512 A-scans. Images from B-scans can be presented as grey scale or false colour images. Greyscale images are usually preferable for identifying fine detail, for example, the differences in the layers of the

retinal microstructure. In false colour images, bright colours such as red or white represent areas of high reflectivity, while darker colours such as blue or black represent areas where the reflections are minimal or nonexistent.

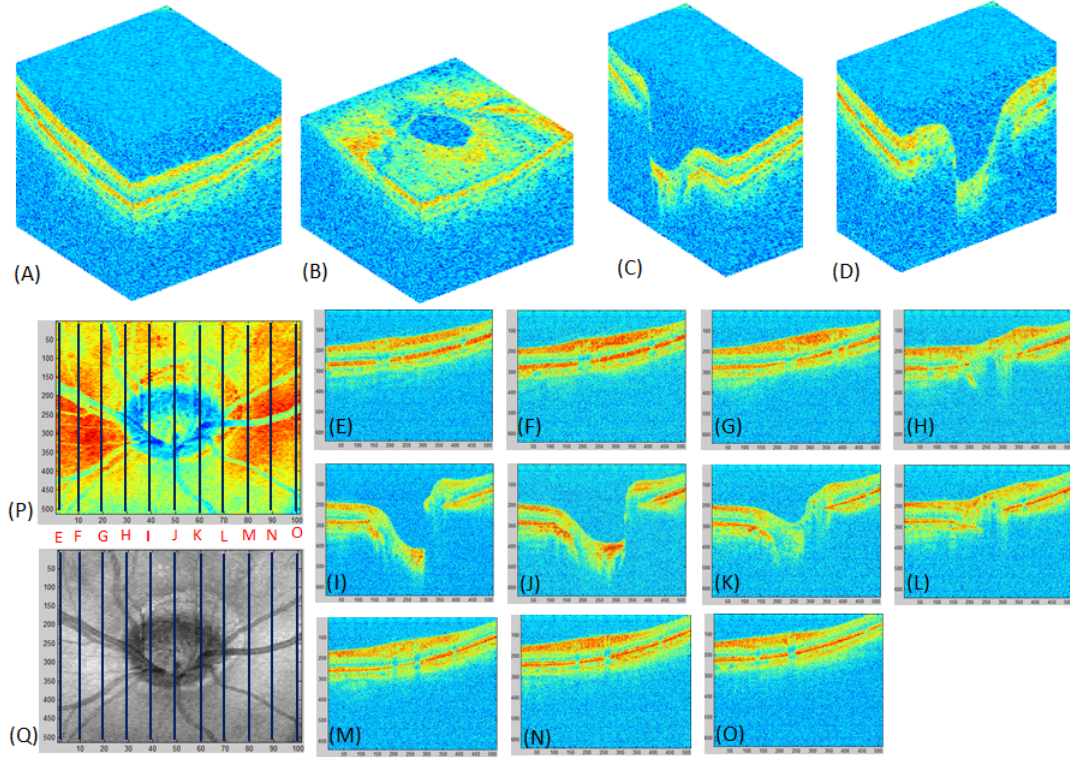


Figure 2.10: The SD-OCT example images captured by using the RTVue-100 system around the ONH area.

RTVue-100 (Optovue, Fremont, CA, USA) system is one example of a SD-OCT imaging system with high speed image capture (26,000 A-scans per second). It achieves up to $5\mu\text{m}$ axial resolution, which is two times higher resolution than the StratusOCT (Carl Zeiss Meditec Inc., Dublin, CA, USA) system. This system can obtain a 3D optic nerve head (ONH) image with 16 bits per pixel and 101 B-scans, 513 A-scans, 768 pixels in depth. An example 3D image acquired by using RTVue-100 system around the optic nerve head (ONH) area is shown in Figure 2.10. Figure 2.10 (A) shows the ONH SD-OCT volume, Figures 2.10 (B)-(D) show the reduced volumes of the original ONH volume in X, Y, Z direction. Figures 2.10 (E)-(O) are the 1st, 10th, 20th, 30th,

40th, 50th, 60th, 70th, 80th, 90th, 100th scans from the ONH volume, respectively. Figures 2.10 (P) and (Q) are the colour and the grey level en face images.

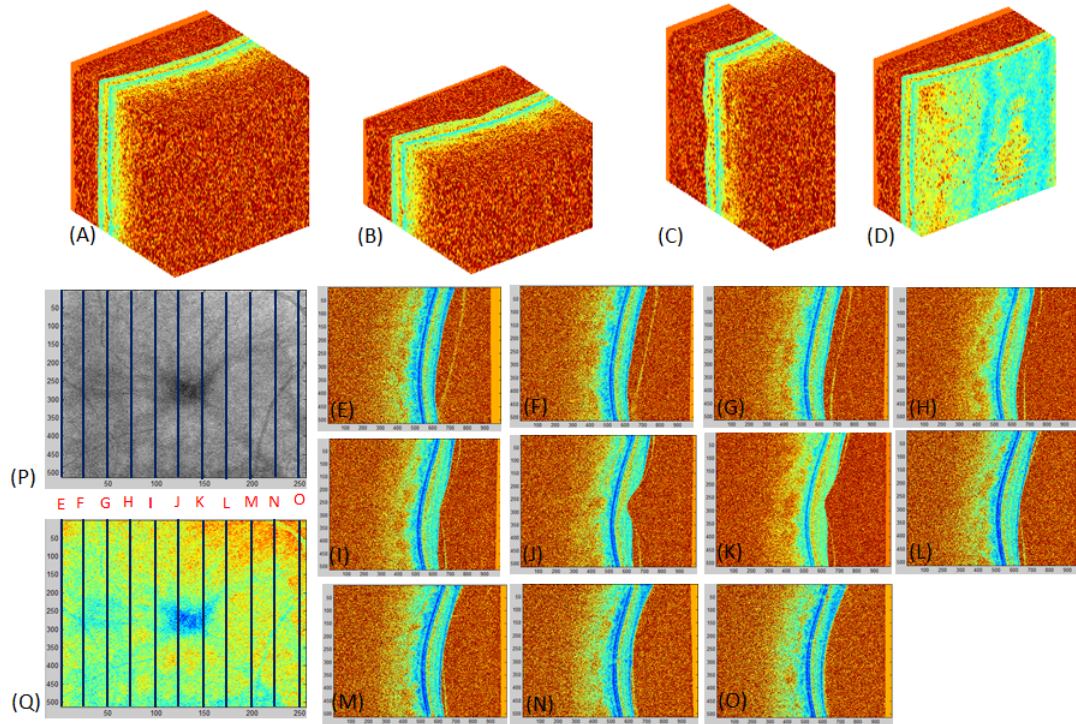


Figure 2.11: The SD-OCT example images taken by using the Spectralis HRA+OCT system around the macular area.

Spectralis HRA+OCT (Heidelberg Engineering, Germany) is another example of a SD-OCT system. It acquires up to 40,000 A-scans per second for a 3D image. It achieves up to $3.9\mu m$ axial resolution, $7\mu m$ depth resolution and $14\mu m$ lateral resolution. This imaging system has been widely used to diagnose retinal diseases, which provides 3D image with 256 B-scans, 512 A-scans, 992 pixels in depth and 16 bits per pixel. Figures 2.11 and 2.12 show example volume images of SD-OCT Spectralis HRA+OCT around the macula and ONH, respectively. Figure 2.11 (A) shows the example macular SD-OCT volume, Figures 2.11 (B)-(D) show the reduced macula SD-OCT volumes in X, Y, Z direction. Figures 2.11 (E)-(O) are the 1st, 25th, 50th, 75th, 100th, 125th, 150th, 175th, 200th, 225th, 250th scans from the ONH volume, respec-

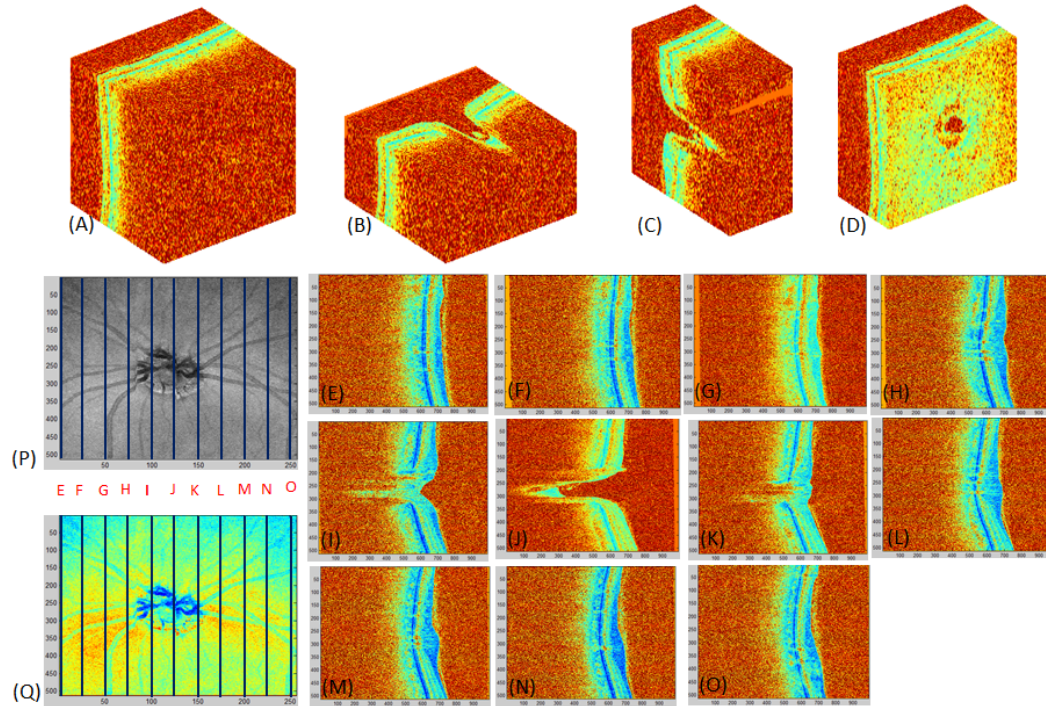


Figure 2.12: The SD-OCT example images taken by using the Spectralis HRA+OCT system around the ONH area.

tively. The grey level and colour en face images of the macular volume are shown in Figures 2.11 (P) and (Q) respectively. An example ONH volume captured by using the Spectralis HRA+OCT system is shown in 2.12 (A). The reduced volumes of the ONH volume in X, Y, Z direction are shown in Figures 2.12 (B)-(D), respectively. The 1st, 25th, 50th, 75th, 100th, 125th, 150th, 175th, 200th, 225th, 250th scans captured from the ONH volume are shown in Figures 2.12 (E)-(O), respectively. Figure 2.12 (P) and (Q) are the grey level and colour en face images.

Swept-source OCT (SS-OCT)

Swept-source OCT (SS-OCT) is the latest form of OCT. Because previous forms of OCT technologies do not have the ability to view deeply or clearly enough into the eye tissues, the primary function and development of SS-OCT is to enable a clearer and deeper view into the eye, gaining the ability to visualise the choroid. SS-OCT employs

a fast wavelength scanning light source such as laser rather than a low-coherence light source compared to TD-OCT and SD-OCT [Lim et al., 2014].

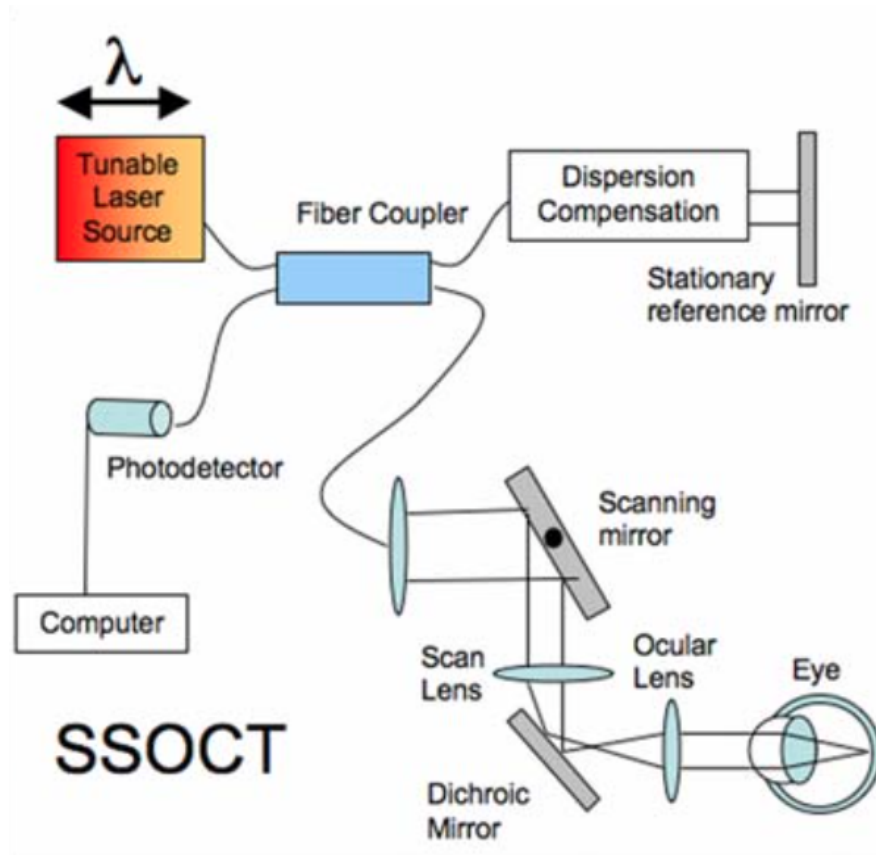


Figure 2.13: The setup of the swept source OCT (SS-OCT) imaging system [Schuman, 2008].

The setup of the swept-source OCT imaging system is shown in Figure 2.13 [Schuman, 2008]. Instead of using a spectrometer and a CCD camera to detect the interference signal in SD-OCT technology, a frequency swept laser source and a high speed photodetector are used to detect the interference signal. The reflections from the scanning mirror and reference mirror are detected by a single photodetector, which greatly increases the scanning speed and reduces the cost because the photodetector is much cheaper and simpler than a CCD camera [Schuman, 2008]. By using the swept source, the SS-OCT system is able to provide faster scanning speeds, uniform image quality and improved vitreous visualisation. Furthermore, the SS-OCT adopts longer wavelengths

(1050 nm) which increase tissue penetration, reduce intra-tissue light scattering, and make it possible to see the optic nerve and macula on the same scan.

DRI OCT-1 Atlantis (Topcon, Tokyo, Japan) is one example of a SS-OCT system. It provides 100,000 A-scans per second with 1,050 nm wavelength, which is the fastest scanning speed in the world [Schuman, 2008]. It enables the viewing of deep eye tissues such as choroid and sclera within a very short time. This system achieves a high resolution with 20 μm lateral resolution and 8 μm in-depth resolution.

2.3 Retinal Diseases

The retina is the light sensitive tissue which is responsible for vision. It is located on the inside back wall of the eye. The retina are vulnerable to diseases, including glaucoma, diabetes retinopathy, age-related macular degeneration, cardiovascular diseases and other inherited retinal degenerations. Some of the diseases can lead to visual loss or permanent blindness. Some of the most prevalent retinal diseases are briefly introduced in the following.

2.3.1 Glaucoma

Glaucoma affects the optic nerve of the eye. It increases the pressure in the eye because the extra eye fluid (Aqueous Humour) flows through an area of the sclera known as the Trabecular Meshwork and disrupts this area [Quigley and Broman, 2006]. Glaucoma is the second highest cause of permanent blindness [Thylefors et al., 1995]. The eye regulates the necessary drainage of fluid through the Trabecular Meshwork. This pressure is known as Intra Ocular Pressure (IOP). Although people with a high IOP may not necessarily go on to develop Glaucoma, sufferers do tend to have a higher level of IOP which may often be hereditary. Glaucoma is typically without symptoms until later in life. These affected are usually 40 and over. The symptoms of Glaucoma are: gradual loss of peripheral vision leading to tunnel vision.

There are two main types of Glaucoma: Open-angle Glaucoma and Angle-closure Glaucoma. Figure 2.14 compares the two types of Glaucomatous fundus images with the image of a healthy fundus. The cup-to-disc ratio (CDR) is measured to diagnose and track the progression of glaucoma. This ratio is calculated by comparing the diameter of the optic cup with the diameter of the optic disc. A healthy eye normally has almost a 0.3 cup-to-disc ratio. A large cup-to-disc ratio may indicate glaucoma.

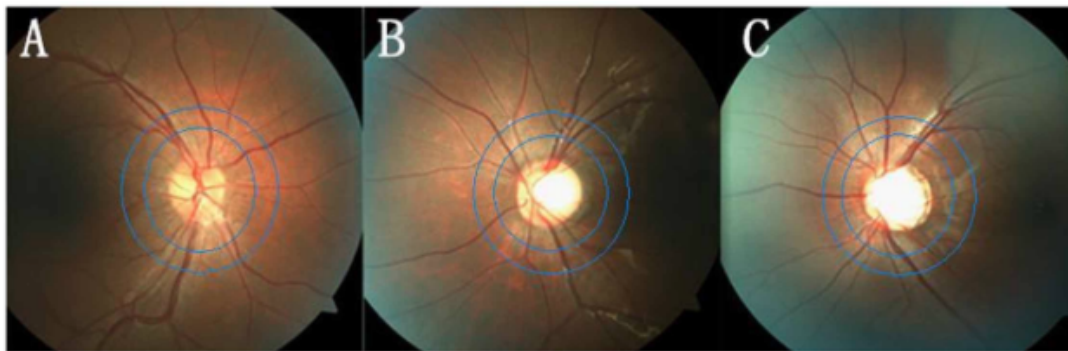


Figure 2.14: Glaucomatous damage shown on fundus images [Gao et al., 2015]. (A) Healthy fundus example, (B) Angle-closure Glaucoma fundus example, (C) Open-angle Glaucoma fundus example.

Open-angle Glaucoma

Open-angle Glaucoma is the most common type of Glaucoma [Quigley and Broman, 2006]. The pressure in the eye is raised in two ways: first, the eye fluid cannot effectively drain through the trabecular meshwork even though it may appear to be unobstructed; second, the eye produces more fluid than can be drained. This type of Glaucoma is usually caused by age-related degeneration. As the condition takes a long time to manifest, sufferers may not be aware of symptoms until later in life, typically from the ages of 40 onwards [Quigley and Broman, 2006]. Symptoms are often painless and gradually lead to a slow degeneration of vision.

Angle-closure Glaucoma

Angle-closure Glaucoma is the most serious form of Glaucoma [Quigley and Broman, 2006]. It occurs when the flow of eye fluid through the trabecular meshwork on to the drainage site is impeded because the iris is at an angle and pushed against the trabecular meshwork, causing an acute build-up of pressure. If Angle-closure Glaucoma is not detected early, significant damage can be caused to the retina and optic nerve. The symptoms of this form of Glaucoma manifest rapidly and include severe pain in the eye, nausea, blurred vision, halos seen when looking into a light, and redness to the eye. Angle-closure Glaucoma is treated as a medical emergency, as symptoms are not apparent until they become severe.

Treatments for Glaucoma

Although Glaucoma cannot be cured, the condition can be managed. The degeneration of the eye can be slowed by treatments which help drain the eye, such as prostaglandins in the form of eye drops, oral supplements, or the use of beta blockers to reduce pressure within the eye. Also, surgical treatments can be performed such as an argon laser trabeculoplasty (ALT) , which improves the flow of fluid through the trabecular meshwork, or removal of a portion of the trabecular meshwork to relieve pressure as well as improve the flow of fluid.

2.3.2 Diabetes

Diabetes is a long term metabolic disease in which blood sugar levels are high because the body produces an insufficient amount of insulin or the cells are unable to respond properly to it. Nowadays, diabetes affects 387 million people worldwide, increasing by 205 million by 2035 according the International Diabetes Federation [Guariguata, 2013]. There are two different types of diabetes. In Type 1 diabetes the body's immune system attacks the cells that produce insulin [Harjutsalo et al., 2013], [Alberti et al., 1998]. Type 1 diabetes usually develops in children and young adults. People with Type

Type 1 diabetes need injections of insulin every day in order to manage blood glucose levels, or they will die. In addition, regular blood tests are necessary to check blood-glucose levels and a special diet should be followed as well. Type 2 diabetes accounts for 90% of cases [Melmed et al., 2011]. The pancreas is not able to produce sufficient insulin to regulate blood glucose levels or the body's cells are unable to react to it properly. Type 2 diabetes can occur at any age but is often associated with obesity. Damage to the area of the retina that is used for fine vision (maculopathy) and cataracts are the largest problems for people with Type 2 diabetes. Type 2 diabetes can usually be managed with diet and exercise but most people eventually require oral drugs or insulin injections.

Diabetes retinopathy, i.e. damage to the retina, is a side effect of diabetes, eventually leading to blindness. In the first 20 years of the disease nearly all patients with Type 1 Diabetes and 60% of patients with Type 2 diabetes develop diabetic retinopathy. Excess blood-glucose caused by diabetes damages the blood vessels in the eye which can lead to fluid draining into the macula which causes it to swell leading to blurred central vision. In later stages of diabetes retinopathy, these damaged blood vessels can leak blood into the centre of the eye which can lead to loss of vision.

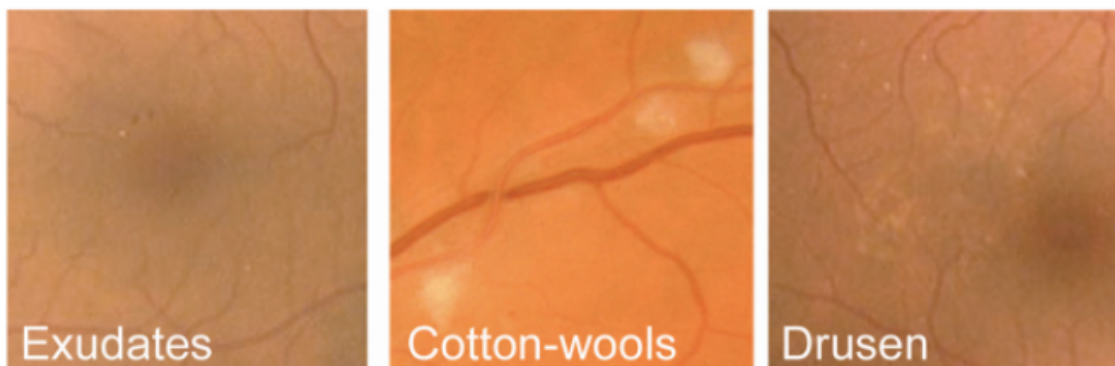


Figure 2.15: Some examples of fundus images which are affected by diabetes retinopathy, including exudates, cotton-wool and drusen [Niemeijer et al., 2007].

Figure 2.15 shows some example diabetes retinopathy fundus images [Niemeijer

et al., 2007]. There are four stages of diabetic retinopathy: Mild: The earliest stage of retinopathy. Small balloon-like swellings occur in the retina's tiny blood vessels causing microaneurysms which begin to damage the eye. Moderate: Blood vessels leading to the retina become blocked causing malnourishment and damage. Severe: The retina attempts to grow new blood vessels but the vessels created are abnormal and weaker than usual with thin walls which can rupture. These new weaker blood vessels rupture causing them to leak blood into the retina, destroying it, and resulting in severe vision loss or blindness.

The main symptoms of diabetes retinopathy are: intermittent blurred vision, double-vision, difficulty reading, spots in field of vision, shadows or veils across the field of vision, redness of the eye and pain or pressure [Melmed et al., 2011]. There is no direct cure for diabetic retinopathy but laser surgery can reduce further damage especially if carried out before the retina is severely damaged. A vitrectomy (surgical removal of the vitreous gel) and anti-VEGF (Vascular endothelial growth factor) inactions or anti-inflammatory medicine are effective in shrinking the new weakened blood vessels in the later proliferative stage.

2.3.3 Age-Related Macular Degeneration (AMD)

Age-related macular degeneration (AMD) is a medical condition affecting the macula, an area of the retina responsible for all central vision. AMD is a leading cause of visual impairment and blindness in adults aged 50 and over [Friedman et al., 2004]. Typically, individuals with AMD experience loss or corruption of vision in the centre of their visual field with peripheral vision generally unaffected. The symptoms of AMD are: blurring of central vision, straight lines appearing blurred or distorted, blind spots in the central field of vision, eyes taking longer than usual to adjust to normal light after bright light. Deterioration and an increased frequency of symptoms occur more quickly with those who have wet AMD. It is still unclear what causes AMD. However, age, smoking, diet and family history are known to be contributory factors. There are

two kinds of AMD, dry AMD and wet AMD. Figure 2.16 shows wet and dry AMD examples on B-scan macula and fundus images.

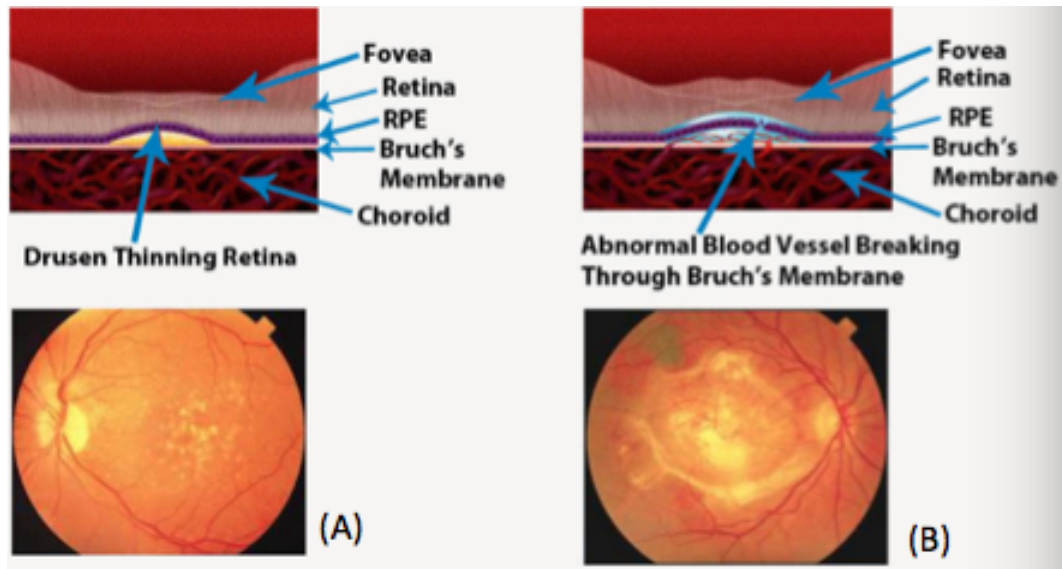


Figure 2.16: Some examples of AMD damage shown on B-scan macula and fundus images [mac, 2015]. (A) Dry AMD example for both B-scan macular and fundus images, (B) Wet AMD example both on B-scan macula and fundus images.

Dry AMD

The dry form of AMD is caused by a build-up of waste products known as drusen [Friedman et al., 2004]. Drusen are naturally occurring waste products that increase in quantity with age as the eye becomes less able to remove them. It is uncertain what causes the increase. Drusen cause macular degeneration, and there is often a link between increased Drusen and Multiple Sclerosis (MS). Dry AMD is the most common form of AMD and accounts for 90% of all AMD cases. Although dry AMD cannot be cured or reversed, and it generally involves only a slow degeneration with some individuals retaining clarity of vision for many years. In later stages dry AMD can evolve into wet AMD. Although there are no current treatments for dry AMD, the Age-Related Eye Disease Study (AREDS) has concluded that high dose of Antioxidants and Zinc may help to slow the advance of dry AMD [Group et al., 2001].

Wet AMD

The wet form of AMD is known as the choroidal neovascularization (CNV) [Friedman et al., 2004]. It includes 10% of all AMD cases and is responsible for 90% of legal blindness in all AMD patients [Holz and Spaide, 2010]. Wet AMD occurs due to abnormal blood vessels breaking and leaking under the macula, eventually scarring and causing cell damage. Symptoms of wet AMD can manifest quickly and without treatment the condition can deteriorate rapidly, usually within a period of weeks or even days. Several forms of treatment for wet AMD exist, most commonly in the form of injections known as anti-angiogenic therapy. Anti-angiogenics, such as Lucentis, help to stem the development of abnormal blood vessel growth around the macula. Other treatments involve laser therapy which acts to block damaged blood vessels and prevent further abnormal growth in areas around the macula helping to reverse some of the damage and slow further degeneration.

2.3.4 Cardiovascular Diseases (CVD)

Cardiovascular diseases primarily affect the function of the heart and blood vessels. In 2008, over 17.5 million people died worldwide from CVD, 31% of all causes of death [Alwan et al., 2011]. In the EU alone, the estimated annual cost of CVD to the economy is around €196 billion [Nichols et al., 2012]. Within this total, 54% is for healthcare, with 24% for productivity losses and 22% for informal care of CVD patients.

The primary examples of CVDs are:

1. Coronary heart disease (CHD): This disease is a blockage or narrowing of blood vessels that supply oxygen and blood to the heart, caused by a buildup of fat and cholesterol in the artery walls. It is the leading cause of death worldwide. According to the National Health Service (NHS), it causes around 1117,000 deaths per year in United Kingdom [of Health, 2000].
2. Cerebrovascular disease: A group of diseases affect the blood vessels to the brain,

causing limited or no blood flow to the affected areas [Flammer et al., 2013]. Cerebrovascular disease includes aneurysms, a chronic dilation of the bronchi which can enlarge and eventually rupture. This disease is often a common cause of strokes. A stroke occurs when part of the brain is damaged by a lack of blood supply or there is bleeding into the brain from a burst blood vessel. The lack of blood supply causes part of the brain to die, a process known as cerebral infarction. About 10% of strokes are caused by bleeding from arteries in the brain, which directly damages the brain's tissues and can also cause loss of blood supply.

3. Peripheral arterial disease (PAD): This is also called Peripheral Vascular Disease (PVD). Deposits of fat build-up in the arteries, restricting the blood supply to the leg muscles. This process is called atherosclerosis. PAD is more common with age increasing, affecting approximately 1 in 5 over 70s. On the average, men develop PAD earlier than women.
4. Rheumatic Heart Disease (RHD): This disease is caused by rheumatic fever, streptococcal bacteria, which damage the heart muscle and valves [Flammer et al., 2013]. Rheumatic fever may develop in very young children and young adults, but it is most common in 5 to 15 years old children.
5. Congenital heart disease (CHD): This disease is a malformation of the heart of birth. It is a defect with the heart's structure and blood vessels, which causes more deaths than other disease in the first year of life. According to the NHS, it affects up to 9 out of 1000 babies born in Unite kingdom [of Health, 2000].
6. Deep vein thrombosis (DVT) and pulmonary embolism: Blood clots mainly formed in the veins in the lower leg and thigh. The clots can move to the heart and the lungs when dislodged. According to the NHS, DVT affects 1 in every 1000 people in the United Kingdom each year [of Health, 2000].

The retina is a unique place in the body where microcirculation can be viewed directly. The retina tissue consumes one of the highest rates of oxygen in the body; therefore detecting changes in the microcirculation within the eye can often predict the development of cardiovascular diseases such as CHD [Liew and Wang, 2011]. Subsequent study and analysis of the retinal micro-vasculature has produced information about the structure as well as the functionality of the vessels. However, its clinical application has only recently gained some attention.

Most of eye diseases can be diagnosed using retinal imaging techniques, such as fundus imaging systems, OCT imaging systems and so on. Many algorithms have been designed to extract retinal structures from retinal images, which are analysed by ophthalmologists to diagnose eye diseases. Level set method is one of the most widely used algorithms for segmenting and extracting retinal structures.

2.4 Level Set Method

There are two major classes of the level set method: region-based model and edge-based model. The edge-based model uses local edge information to direct an active contour to the object boundaries, while the region-based models use a certain descriptor to identify each region of interest to guide the active contour to the desired boundary.

2.4.1 Region Based Model

The region based models usually include two parts: a regularity part to smooth the shapes of the contours, and an energy minimisation part to detect uniform features. The Mumford-Shah model [Mumford and Shah, 1989] was the earliest level set model developed to segment images. Let Ω be the image domain, let I be a grey level image, and let C be a contour desired to segment by using the energy function, which separates the image domain Ω into 2 disjoint regions: $\Omega_1, \dots, \Omega_N$. The energy function of the

model is defined as:

$$F^{MS}(u, C) = \int_{\Omega} (u - I(X))^2 dX + \mu \int_{\Omega \setminus C} |\nabla u|^2 dX + \nu |C| \quad (2.1)$$

where $|C|$ is the length of the contour, and u is an image that approximates the original image I . The first term of (2.1) is the data term, the second is the smoothing term, and the third is regularisation term. More specifically, the data term forces u to be close to the image I , the smoothing term is to smooth the image area from the contour C , and the regularisation term is to reduce the length of the contour C . However, the fact that the unknown contour C has lower dimension and the non-convexity of F^{MS} makes it difficult to minimise F^{MS} .

Chan-Vese (CV) [Chan and Vese, 2001] simplified the Mumford-Shah function and proposed a powerful and flexible method, which is able to segment many types of images. The energy function is defined as:

$$F^{CV}(\phi, c_1, c_2) = \lambda_1 \int_{outside(C)} (I(X) - c_1)^2 dX + \lambda_2 \int_{inside(C)} (I(X) - c_2)^2 dX + \mu \cdot Length(C) + \nu \cdot Area(inside(C)) \quad (2.2)$$

where $\lambda_1, \lambda_2 > 0$, $\mu \geq 0$, $\nu \geq 0$ are fixed parameters determined by the user, which are usually fixed as $\lambda_1 = \lambda_2 = 1$ and $\nu = 0$ in calculations. The energy function can be rewritten as:

$$F^{CV}(\phi, c_1, c_2) = \lambda_1 \int_{outside(C)} (I(X) - c_1)^2 dX + \lambda_2 \int_{inside(C)} (I(X) - c_2)^2 dX + \mu \cdot \int_{\Omega} |\nabla H(\phi(X))| dX + \nu \cdot \int_{\Omega} H(\phi(X)) dX \quad (2.3)$$

where ϕ is a level set function, the $outside(C)$ and $inside(C)$ indicate the region outside and inside the contour C , respectively, and c_1 and c_2 are the average image intensity of $outside(C)$ and $inside(C)$. The zero level set contour of ϕ is defined as $C = \{X : \phi(X) = 0\}$. This contour separates the image domain Ω into two disconnected regions

$\Omega_1 = \{X : \phi(X) > 0\}$ and $\Omega_2 = \{X : \phi(X) < 0\}$. The regularisation term Heaviside function H and the average intensities c_1 and c_2 are formulated as:

$$H_\epsilon(x) = \frac{1}{2} \left(1 + \frac{2}{\pi} \arctan\left(\frac{x}{\epsilon}\right) \right) \quad (2.4)$$

$$c_1 = \frac{\int_{\Omega} I(X) H(\phi(X)) dX}{\int_{\Omega} H(\phi(X)) dX} \quad (2.5)$$

$$c_2 = \frac{\int_{\Omega} I(X) (1 - H(\phi(X))) dX}{\int_{\Omega} (1 - H(\phi(X))) dX} \quad (2.6)$$

Variational region based level set methods are proposed to solve different segmentation problems based on the Chan-Vese model. The Local binary fitting model proposed by Li et al. [Li et al., 2007] modifies the region term by two fitting functions instead of the global average intensities of outside and inside of the contour with a kernel function. These two fitting functions approximate the local image intensity in outside(C) and inside(C). Sun et al. [Sun et al., 2012] present the local morphology fitting model by modifying the region term and adding a level set regularisation term. They use the maximum fuzzy opening and minimum fuzzy opening instead of the average intensity outside and inside of the contour in the region term for more complicated problems. Li et al. [Li et al., 2008] introduce the region-scalable fitting model to improve their previous work by using a Gaussian kernel function to scale the region term to solve the segmentation problem under uneven illumination. Zhao et al. [Zhao et al., 2015] develop a hybrid region term based level set model to extract region information from two inputs to locate objects with irregular or oscillatory shapes.

2.4.2 Edge Based Model

Normally, the edge based models include two parts: the first part (regularity part) constrains the shape of the contour, and the second part (edge constraint part) is to drive the contour towards the object boundary. Caselles et al. [Caselles et al., 1993]

presented the geometric active contour model for image processing in 1992, which was the earliest edge based level set method. This method is able to segment smooth shapes and can detect multi-regions simultaneously. A geodesic active contour model was presented by Caselles et al. [Caselles et al., 1997], [Kichenassamy et al., 1995] based on the theory of the geodesic curve. This method improves the geometric active contour model and makes it more stable in order to detect boundaries with large variations and gaps. According to Li et al's model [Li et al., 2010], the energy function of the geodesic model is rewritten as:

$$F_E(\phi) = \lambda L_g(\phi) + \alpha A_g(\phi), \quad (2.7)$$

where $\lambda > 0$ and $\alpha \in R$ are constant coefficients. The energy functionals $L_g(\phi)$ and $A_g(\phi)$ are formulated as:

$$L_g(\phi) \approx \int_{\Omega} g(x) \delta_{\epsilon}(\phi(X)) |\nabla \phi(X)| dX \quad (2.8)$$

$$A_g(\phi) \approx \int_{\Omega} g(x) H_{\epsilon}(-\phi(X)) dX \quad (2.9)$$

where $g(x)$, $H_{\epsilon}(x)$, $\delta_{\epsilon}(x)$ are the edge indicator function, the Heaviside function respectively and Dirac delta function, respectively. The edge indicator function and Dirac delta function are defined by:

$$g(x) \approx \frac{1}{1 + |\nabla G_{\delta} * I_m(X)|} \quad (2.10)$$

$$\delta_{\epsilon}(x) = H'_{\epsilon}(x) = \frac{1}{\pi} \frac{\epsilon}{\epsilon^2 + x^2} \quad (2.11)$$

where G_{δ} is the Gaussian kernel with a standard deviation δ . The indicator is used to smooth the image and reduce the noise through the convolution.

The first term $L_g(\phi)$ calculates the line integral of the edge indicator function g along the zero level set contour of ϕ with the Dirac delta function δ_{ϵ} . When the zero

level set of ϕ as a contour is parameterised as $C: [0, 1] \rightarrow \Omega$, the first term $L_g(\phi)$ can be rewritten as $\int_0^1 g(|\nabla I(C(s))|)|C(s)|ds$. This term $\int_0^1 g(|\nabla I(C(s))|)|C(s)|ds$ was first introduced by Caselles et al. [Caselles et al., 1997], where $g(|\nabla I(C(s))|)$ contains the boundary information of the object. The energy of this term $L_g(\phi)$ is minimised when the level set function ϕ is close to the target boundary of the object.

A weighted area of the region $\Omega_\phi^- \approx \phi(X) < 0$ is calculated by the second term $A_g(\phi)$. When $g(x) = 1$ as a special case, this term $A_g(\phi)$ computes the area within the contour Ω_ϕ^- . This term $A_g(\phi)$ is applied to speed up the motion of the level set function ϕ to the desired object boundary in the evolution process, especially when the initial contour is located far away from the target boundary of the object. The level set function ϕ is negative inside the zero level contour and positive outside the zero level contour. The coefficient α for the weighted area term should be positive when the initial contour is located outside the object, so that the zero level contour will shrink to the target boundary in the level set evolution. Otherwise, the coefficient α should be negative when the initial contour is located inside of the initial contour, so that the zero level contour will expand to the target boundary in the level set evolution. When the edge indicator function $g(x)$ is close to the object boundary, this weighted area term $A_g(\phi)$ will slow down the shrinking or expanding of the zero level contour.

In order to achieve different segmentation requirements, variational edge based level set models are developed based on the geometric active contour model. The distance regularised level set method [Li et al., 2010] adds a distance regularisation term to the geometric active contour model to maintain the desired shape of the level set function ϕ and avoid its induced numerical errors. Pratondo et al. [Pratondo et al., 2016] introduce an edge-stop functions based level set method to stop the contour evolution at the proper boundary. It is considered as a challenge to stop the contour evolution at proper boundary. Li et al. [Li et al., 2015] present a new geodesic model to integrate the local and global edge information in a signed pressure force function. This method can deal with images large variations in intensity.

2.5 Retinal Image Analysis

Retinal imaging has rapidly developed within ophthalmology over the past 20 years, becoming an essential part of detecting and diagnosing eye diseases, preventing serious deterioration such as sight loss or blindness. Development of affordable and efficient forms of imaging technology, such as fundus imaging cameras and OCT imaging modalities, has made it possible to examine the eye to detect and diagnose several different eye diseases efficiently and non-invasively. The retinal images from different imaging modalities are the main indicators of different retinal diseases as well as cardiovascular diseases. However, it is time-consuming or even impossible to hand-label all of the retinal structures in these images. Therefore, automated fundus and OCT image analysis tools are extremely important for ophthalmologists to detect and analyse even tiny structural changes, and to make more accurate diagnoses and give proper and efficient treatments in the early stages to prevent serious deterioration.

2.5.1 Fundus Image Analysis

Fundus imaging is one of the most widely used imaging systems in clinics and eye hospitals. Fundus cameras capture a 2D fundus image, which is obtained by using reflected light to form a 2D representation of 3D retinal semi-transparent tissues. The retinal structures of fundus images are important indicators for eye diseases, it is necessary to extract and analyse these information for disease diagnosis. Therefore, many researchers from different backgrounds including computer science and medical analysis are attracted to research of fundus images. More than 1000 papers have been published in this area. They cover the following topics [Abràmoff et al., 2010]:

1. Retinal structure detection and extraction:
 - retinal blood vessels: vessels diameter, vein classification, vessel occlusion;
 - fovea, optic disc, optic cup and rim, cupping.

2. Retinal abnormalities location and extraction:

- retinal abnormalities due to blood vessels: hemorrhages, microaneurysms, cottonwool spots;
- retinal abnormalities due to the pigment epithelium: drusen, hyper and hypopigmentation;
- retinal abnormalities due to the choroid: nevus and melanoma, choroidal lesions.

3. Image quality assessment:

- image quality verification, imaging artifact location, and iatrogenic lesion detection.

Our study mainly focuses on the segmentation of retinal blood vessels and optic discs from fundus images. More details of the methods will be given in chapters 3 and 4. The presence of exudates and lesions, low contrast between vessels and background, and the intensity inhomogeneity, make accurate vessel segmentation more difficult and complex. The current challenges of blood vessel segmentation are summarised as follows [Abràmoff et al., 2010]:

- Detect the smaller vessels of which the diameter is only a few pixels;
- Avoid misclassifying vessels on the boundary of the optic disc;
- Avoid misdetection of the intensity inhomogeneities due to lesions in blood vessels;
- Segment vessels accurately, given the low contrast between the vessels and the background;
- Detect blood vessels inside the optic disc.

It is difficult to accurately detect and segment the optic discs from fundus images, because of the irregular shape of optic disc, the intensity inhomogeneity in the optic disc, and the presence of retinal pathologies around or within the optic disc. The main challenges of optic disc segmentation are listed in the following [Abràmoff et al., 2010]:

- Detect the optic disc when it is affected by retinal pathologies;
- Segment optic discs with complex or irregular shapes;
- Avoid misdetecting the optic disc when there is optic disc swelling;
- Avoid misclassifying the optic disc boundary when it is obstructed by retinal vessels;
- locate the optic disc when there is poor contrast with background.

2.5.2 OCT Image Analysis

Compared to the fundus imaging technique, the OCT imaging technique is able to capture 3D images with a wealth of relevant information. The increasing improvements in OCT imaging technique has enabled a clearer view of retinal structures and detailed tissues. The information obtained by OCT imaging modalities is especially important for eye experts to diagnose the diseases and develop proper treatment strategy. However, it is time consuming or even impossible to hand label all the retinal structures and analyse this information. Therefore, automated and advanced OCT image analysis methods are required to segment and analyse the clinically relevant structures. Up till now, many papers have been covered the following research topics [Abràmoff et al., 2010]:

- detect and analyse the intra-retinal layers from 3D OCT images;
- locate and reconstruct the retinal vessels from 3D OCT images;
- segment and analyse the optic nerve head from 3D OCT optic nerve head images;

- classify and analyse retinal lesions from 3D OCT images.

We focus our study on the intra-retinal layer segmentation from both 3D macular and optic nerve head images. The details of the segmentation methods are discussed and explained in chapters 5, 6 and 7. By comparing with 2D layer segmentation methods on a sequence of 2D OCT slices, 3D layer segmentation methods take advantages of 3D contextual information on 3D OCT image. However, there are still several challenges in intra-retinal layers segmentation from 3D OCT images, which can be summarised as follows:

- Perturbation of 3D OCT images and image artefacts are produced by the eye movements during the imaging. It is difficult to remove all the noise and at the same time keep the relevant image structures;
- Intra-retinal layers segmentation can be difficult in images affected by disease;
- The leakages and irregular shapes of the optic nerve head can make it difficult to detect the intra-retinal layers accurately in ONH images;
- The layer boundaries within the retina is not distinct because of immature imaging modalities. The appearance of the layers may be inhomogeneous and inconsistent because of the presence of blood vessels and blood vessel shadows inside the layers.

In order to overcome these challenges mentioned above, level set based methods are proposed and applied to extract retinal structures, including retinal blood vessels and optic disc from 2D fundus images, intra-retinal layers and macular layer from 3D macular OCT images and intra-retinal layers from 3D optic nerve head images, in the following chapters. In chapters 3 and 4, we focus on the 2D retinal image analysis and the retinal structures are segmented from 2D retinal images. In chapters 5, 6 and 7, we

move the topic to the 3D retinal structure analysis and the retinal structures from 3D retinal images are segmented. The main baseline of the proposed methods are based on the level set method. These retinal structure information, extracted by methods presented in the following chapters, can be analysed and used by ophthalmologists to diagnose eye diseases in early stages.

Chapter 3

Bayesian Level Set Method Based Retinal Blood Vessels Segmentation

The blood vessels and the optic disc are two important retinal structures from a fundus image. The blood vessels are one of the most important indicators for diagnosing eye diseases. This chapter presents an automated and unsupervised method for segmenting retinal blood vessels from fundus images by using the level set method, which adopts Chan-Vese region-based term with a Gaussian mixture model and a distance regularisation term. Also included in the method are the morphological closing operation and matched filtering to preserve the vessels while removing the noise of the optic disc boundary, and to enhance the blood vessel information. The effectiveness of this method is demonstrated by testing and comparison with the state-of-the-art methods on two public datasets DRIVE and STARE. The experimental results show that our method offers several advantages over other methods, in particular in dealing with interference from the optic disc, displaying the vessels inside the optic disc and segmenting small vessel branches.

The work included in this chapter has been submitted for publication [Wang and Li, 2016]. The manuscript is lead-authored by the author of this thesis, who made substantial contributions to the conception, data collection, processing and writing-up, and sole contributions to the implementation and result analysis.

3.1 Introduction

Computer aided-diagnosis is an important tool in modern ophthalmology for detecting and tracking several retinal diseases such as diabetic retinopathy, hypertension, glaucoma, macular disintegration, neo-vascularisation and vein occlusion. The morphology of retinal blood vessels is an important structural indicator for assessing the presence of retinal diseases and can provide a measure of their progression over time. The quantification of the diameter and tortuosity of retinal blood vessels, manual planimetry has commonly been obtained by ophthalmologists using, which is in general time consuming and prone to human errors [Kwon et al., 2009], especially when the vessel structure is complicated or a large number of images are to be labelled. Therefore, a reliable automated method for retinal blood vessel segmentation, which preserves various vessel shapes, is attractive in computer aided-diagnosis.

Various methods have been developed for segmenting retinal blood vessels from 2-D fundus images. Chaudhuri et al. [Chaudhuri et al., 1989] used 12 different Gaussian templates to find the vessels in all possible directions before extracting them. Hoover et al. presented a vessel segmentation method in [Hoover et al., 2000]. Zana et al. [Zana and Klein, 2001] reported a curvature evaluation method to detect vessel-like patterns in retinal images after noise reduction using morphology operation. Staal et al. [Staal et al., 2004] implementing a k Nearest Neighbor (k-NN) classifier by using extracted image ridges as feature vectors to segment retinal vessels. Mendonca et al. [Mendonça and Campilho, 2006] segmented the retinal vessels using four directional differential operators. The operator responses are used to train a classifier to obtain

the centreline of the blood vessel. Then the vessel information is obtained by a region growing method. Soares et al. [Soares et al., 2006] performed vessel segmentation using Bayesian classification with Gaussian Mixture Models (GMMs) on 2D Gabor wavelet transform response images. Nguyen et al. [Nguyen et al., 2013] combined the generalised line detector with the basic line detectors at varying scales to segment the blood vessels. Kaba et al. [Kaba et al., 2013] developed an automated segmentation method of the retinal blood vessel by combining bias correction and a matched filter to enhance the appearance of the blood vessels. The vessels were extracted using the Expectation Maximisation algorithm. Azzopardi et al. [Azzopardi et al., 2015] segmented blood vessels by thresholding the sum of the responses of two rotation-invariant B-COSFIRE filters. Zhao et al. [Zhao et al., 2015] detected blood vessels by using a hybrid region information based active contour framework.

The aforementioned methods produced some good experimental results. However, due to the intensity inhomogeneity, the poor contrast of the vessels and the presence of lesions in the retinal images, those methods tend to classify the optic disc boundary and the lesions as vessel pixels, especially during the pre-processing steps. Methods such as [Hoover et al., 2000, Soares et al., 2006, Staal et al., 2004, Mendonça and Campilho, 2006] depend on the training sets to achieve good results, and additional training is required for performing segmentation on new datasets.

To address the above problems, we present an automated method for segmenting retinal structure using the level set method. We apply a pre-processing technique based on morphological closing to remove the boundary of the optic disc and retain the vessels inside the optic disc and obtain the closed image. The most likely blood vessel pixels are chosen as seeds. The appearance of the blood vessel is enhanced by using matched filtering. The level set method incorporates the Chan-Vese region based term, a Gaussian mixture term and a distance regularisation term to effectively segment blood vessels from retinal images. Finally, a length filter is used to remove noises and small contours.

The contributions to our method are as follows: (1) The absolute difference between the grey level image and the closed image obtained is calculated to remove the noise due to the high luminosity and retain the images of the blood vessels within the optic disc. (2) The hybrid region based terms including the Chan-Vese region term and Gaussian mixture region term are integrated into the level set method. The hybrid terms maximise the region information, which is extracted from the difference image and vessel enhanced image, to keep small vessels and compensate for variations in the intensity. (3) The Gaussian mixture term computes the negative log likelihood of the blood vessels and background probabilities according to the GMM model, which is updated through each level set iteration according to the characteristics of the image itself, to achieve better segmentation results.

The rest of the chapter is organised as follows. In Section 2, a detailed description of the proposed method is presented. The experimental results on two public datasets are demonstrated in the Section 3. Finally, conclusions are drawn in Section 4.

3.2 Methods

Retinal blood vessels are segmented by three major steps: pre-processing step, vessel segmentation step and post-processing step. Figure 3.1 shows the block diagram of the blood vessel segmentation method. During the pre-processing step, the morphological closing operation and matched filtering are applied to remove the optic disc inference and retain the images of the blood vessels inside the optic disc, and to enhance the blood vessel information and deal with the variations in contrast of the retinal images. In the second step, we apply the level set method with the Chan-Vese region based term, Gaussian mixture term and distance regularisation term to carry out the segmentation. This is followed by the minimisation of a level set energy function. Finally in the post-processing step, we use the length filter to remove background noise due to intensity inhomogeneity.

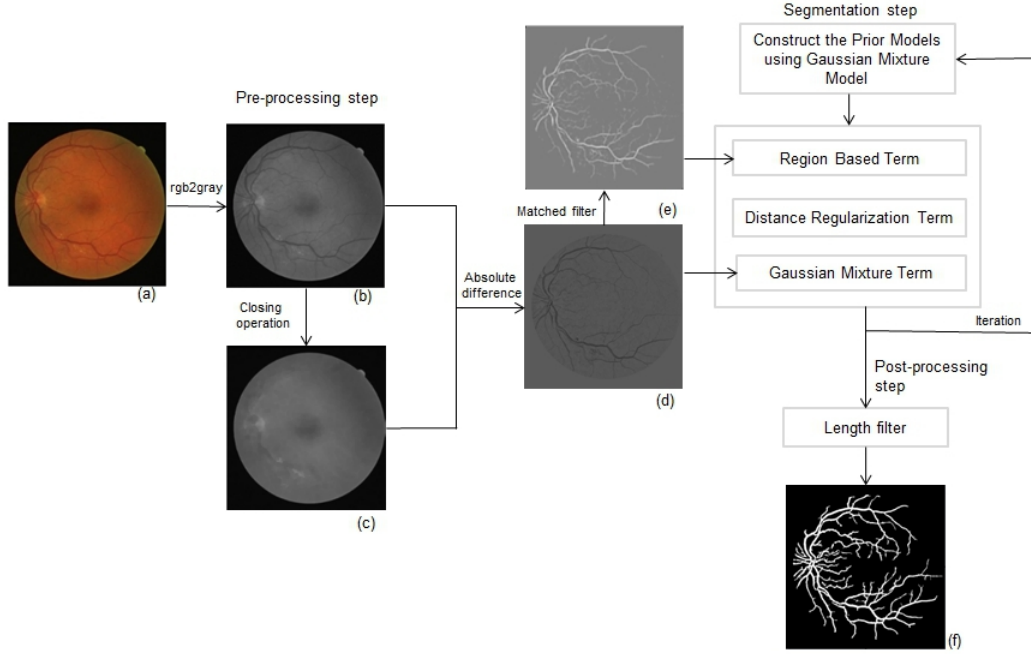


Figure 3.1: Block diagram of the proposed blood vessel segmentation method. (a) The original retinal image. (b) The grey level image (I_g) of the original image. (c) The closing operation of I_g (I_c). (d) The difference image I_d is obtained from the absolute difference between I_g and I_c . (e) The matched filtering response of I_d (I_m). (f) Final output of the proposed method.

3.2.1 Pre-processing

In order to improve the robustness and efficiency of the level set method, a pre-processing step is implemented. The grey level image (I_g) (see Figure 3.1 (b)) contains the intensity information from the colour image, which includes all the vessel information. Then, a morphological closing operation is applied to remove the blood vessels of (I_g). The closed image (I_c) is shown in Figure 3.1 (c). After that, we calculate the image I_d from the absolute difference between the I_g and I_c to remove the noises due to the large luminosity and optic disc interference and retain the images of vessels inside the optic disc. Figure 3.1 (d) shows the difference image.

This is followed by a two dimensional matched filtering [Chaudhuri et al., 1989] on I_d to enhance the appearance of blood vessels. The approach maximises the response over blood vessels and minimises the response for image background. There are three main

characteristics of the blood vessels in fundus images: first, the blood vessels usually have small curvatures; second, the blood vessels have lower reflectance compared to other retinal structures; finally, the width of the blood vessel decreases when it travels away from the optic disc. According to the characteristics of the blood vessel, the variations in vessel intensity can be approximated by a Gaussian curve function as:

$$f(x, y) = A\{1 - ke^{-\frac{d^2}{2\sigma^2}}\} \quad (3.1)$$

where d is the perpendicular distance from pixel (x, y) to the straight line through centre of the blood vessel in the same direction along its length, A is grey-level intensity of the local background of I_d , k represents the ratio of the reflectance between blood vessel and its neighbourhood, and σ defines the spread of the vessel intensity profile. The widths of the vessels are ranged within 2-10 pixels. For the initial calculation, the width of blood vessels are set to 2σ .

Two dimensional matched filter kernel is applied to convolve with the original image and defined as:

$$K(x, y) = -e^{-\frac{x^2}{2\sigma^2}} \text{ for } |y| \leq \frac{L}{2} \quad (3.2)$$

where L denotes the segmented vessel length for which the vessel is assumed in a fixed direction. The direction of the vessel is assumed with the alignment along the y-axis. A vessel is assumed to orient at any angle $\theta (0 \leq \theta \leq \phi)$. The matched filter has maximise response only at an angle $\theta \pm \frac{\phi}{2}$. Therefore, the filter will be rotated for all possible angles to obtain the maximum response for each pixel.

This filter suppresses the response due to the significant background noise. The procedure of the filter reduces the rate of false detection of blood vessels in a non-ideal environment. Here, we use a set of 12 matched filters because the kernel is rotated by $\pm 15^\circ$ to cover all possible directions. According to the experiment, the kernel size of the filter is set to $16 * 15$. The filtered image I_m is shown in Figure 3.1 (e). In addition, because the level set method needs an initialisation input, here we select the most likely blood vessel information as input seeds by thresholding the histogram of I_d . According

to the distribution of the histogram, the 20% highest intensity of I_d will be selected as the input seeds.

3.2.2 Hybrid region terms based segmentation

Our purpose is to segment the blood vessels. Let Ω be the image domain and let ϕ be a level set function. The level set function ϕ is used to separate the image domain Ω into two disjoint regions: Ω_1 and Ω_2 . The novelty of the proposed method is that we are integrating the hybrid region information, which has been extracted from the enhanced image (I_m) and difference image (I_d) by using the Chan-Vese region term [Chan and Vese, 2001] and Gaussian mixture term, into the level set method. The intensity distributions of the vessels and background are assumed to be relatively constant, the Chan-Vese region term is used to model the region information extracted from the vessel enhanced image (I_m) (See Page 35). Furthermore, the region information from the difference image (I_d) is modelled by using the GMM into the Gaussian mixture term. The Chan-Vese region term segments all big vessels and some small vessels, while the Gaussian mixture term locates most of the small vessels and suppresses noise due to intensity inhomogeneity by computing the negative log-likelihood of probabilities from I_d to separate the blood vessels and background. This hybrid region terms based segmentation method maximises the region information from different inputs to keep most of the small branch vessels and compensate the intensity inhomogeneity. Additionally, the distance regularisation term keeps the blood vessel region boundary smooth and avoids background noises due to intensity inhomogeneity.

Prior model construction

Let the blood vessels and background region be labelled 0 and 1 ($L = \{0, 1\}$), respectively. The GMM is used to model the blood vessels and background region, respectively. Let the pixel of I_d be $B = (b_1, \dots, b_i, \dots, b_N)$, where N is the total number of all pixels. $A = (a_1, \dots, a_i, \dots, a_N)$ ($a_i \in L$) is the corresponding initial label according

to the level set function ϕ . The initial GMM with C components parameter set Θ^0 is learned from A and B by using the EM algorithm. It is assumed that the pixel intensity y_i follows the GMM with C components parameters θ_i given the label a_i , $P(b_i|a_i) = G_{mix}(b_i; \theta_i)$.

The parameters set $\Theta = \{\theta_l | l \in L\}$ can be expressed as:

$$\theta_l = (\mu_{l,1}, \sigma_{l,1}, \omega_{l,1}), \dots, (\mu_{l,C}, \sigma_{l,C}, \omega_{l,C}) \quad (3.3)$$

The E-step: At the t^{th} iteration, we can obtain the parameters Θ^t , and the conditional expectation can be deduced as:

$$\begin{aligned} Q(\Theta|\Theta^t) &= E_A [\ln P(A, B|\Theta)|B, \Theta^t] \\ &= \sum_{A \in L} P(A|B, \Theta^t) \ln P(A, B|\Theta) \end{aligned} \quad (3.4)$$

where L is the set of all possible labels, and $P(A, B|\Theta)$ can be rewritten as:

$$P(A, B|\Theta) = P(A|B)P(B|\Theta) \quad (3.5)$$

M-step: Next parameter set Θ^{t+1} is estimated through maximising $Q(\Theta|\Theta^t)$:

$$\Theta^{t+1} = \arg \max_{\Theta} Q(\Theta|\Theta^t) \quad (3.6)$$

The parameters are updated by using $P(l|b_i)$

$$\begin{aligned} \mu_l^{(t+1)} &= \frac{\sum_i P^t(l|b_i)b_i}{\sum_i P^t(l|b_i)} \\ (\sigma_l^{(t+1)})^2 &= \frac{\sum_i P^t(l|b_i)(b_i - \mu_l^{(t+1)})^2}{\sum_i P^t(l|b_i)} \end{aligned} \quad (3.7)$$

Then, let $\Theta^{t+1} \rightarrow \Theta^t$ and repeat from E-step until it converges.

Compared to the supervised learning methods, our method updates the GMM parameters set through each level set iteration until it converges or reaches the maximum iteration number instead of obtaining the constant parameters set from a training process. The performance of these supervised methods normally depends on the variety of images covered in their training set. Our method can update the parameters according to the characteristics of the input data itself.

Gaussian Mixture term

Because of the intensity inhomogeneity of the difference image I_d due to the hemorrhages, exudates and neovascularisation, it is difficult to use one single Gaussian to model the blood vessels and one single Gaussian to model the background. Therefore, a Gaussian mixture model is used to accurately estimate blood vessels. The energy function of this term is formulated:

$$E_M(\phi) = -\nu \int_{\Omega} \log(P(B|A, \Theta)) dx dy \quad (3.8)$$

where $\nu \in \mathcal{R}$ is a constant coefficient. This term calculates the negative log-likelihood of the posterior segmentation probability. Based on the conditional independence assumption of each pixel b , the conditional segmentation probability $P(B|A, \Theta)$ can be expressed as:

$$\begin{aligned} P(B|A, \Theta) &= \prod_{i=0}^N P(b_i|a_i, \theta_{a_i}) = \prod_{i=0}^N G_{mix}(b; \theta_{a_i}) = \prod_{i=0}^N \sum_{c=1}^C \omega_{a_i,c} g(b; \mu_{a_i,c}, \sigma_{a_i,c}) \\ &= \prod_{i=0}^N \sum_{c=1}^C \omega_{a_i,c} \exp\left(\frac{-\log(2\pi\sigma_{a_i,c}^2)}{2} + \frac{-(b - \mu_{a_i,c})^2}{2\sigma_{a_i,c}^2}\right) \end{aligned} \quad (3.9)$$

According to the Jensen's inequality, if $\sum_{c=1}^C \omega_{a_i,c} = 1$, we have:

$$-\log\left(\sum_{c=1}^C \omega_{a_i,c} g(b; \theta_{a_i,c})\right) \leq -\sum_{c=1}^C \omega_{a_i,c} \log(g(b; \theta_{a_i,c})) \quad (3.10)$$

This indicates that minimising the right-hand term will lead to the minimisation of the left term. Therefore, the conditional log-likelihood energy function $U(B|A, \Theta)$ can be estimated:

$$\begin{aligned} U(B|A, \Theta) &= \sum_{l=0}^L \omega_l U(b|a, \Theta_l) \\ &= \sum_{l=0}^L \sum_{c=1}^C \omega_{l,c} \left[\frac{(b - \mu_{l,c})^2}{2\sigma_{l,c}^2} + \frac{1}{2} \log(2\pi\sigma_{l,c}^2) \right] \end{aligned} \quad (3.11)$$

Finally, the region-based term can be rewritten as:

$$\begin{aligned} E_M(\phi) &= \nu \int_{\Omega} U(B|A, \Theta) dx dy \\ &= \nu \left\{ \int_{\Omega} U(b|a, \Theta_0) (1 - H(\phi)) + U(b|a, \Theta_1) H(\phi) dx dy \right\} \end{aligned} \quad (3.12)$$

According to [Zhao et al., 1996], where the Heaviside function $H(\phi)$ is expressed as:

$$H(\phi) = \begin{cases} \frac{1}{2}[1 + \frac{\phi}{\epsilon} + \frac{1}{\pi} \sin(\frac{\pi\phi}{\epsilon})], & |\phi| \leq \epsilon \\ 1, & \phi > \epsilon \\ 0, & \phi < -\epsilon. \end{cases} \quad (3.13)$$

where ϵ is a parameter, usually set to 1.5 [Li et al., 2010].

Level Set formulation

The energy function $E(\phi)$ of our proposed model can be formulated as:

$$\begin{aligned} E(\phi) = & \nu \left\{ \int_{\Omega} U(y_0|x_0, \Theta_0)(1 - H(\phi)) dx dy + \int_{\Omega} U(y_1|x_1, \Theta_1)H(\phi) dx dy \right\} + \\ & \int_{\Omega} \frac{\lambda_R}{2} (|\nabla\phi| - 1)^2 dx dy + \int_{\Omega} \lambda_1 (I_m - c_1)^2 (1 - H(\phi)) dx dy + \\ & \int_{\Omega} \lambda_2 (I_m - c_2)^2 H(\phi) dx dy \end{aligned} \quad (3.14)$$

where λ_R , λ_1 and λ_2 are constant parameters. The first two terms of the proposed model are applied to calculate the negative log-likelihood probabilities according to the prior parameter set (Θ_0, Θ_1) to separate the blood vessels from the background. The third term is the distance regularisation term, which follows Li et al's approach [Li et al., 2010] by smoothing the level set function ϕ and maintaining the signed distance property $|\nabla\phi| = 1$ of the level set function ϕ in the entire domain. This term is used to derive the level set function ϕ close to the blood vessel boundary and avoid the background noise due to intensity inhomogeneity.

The final two terms of our model follow the classical Chan-Vese model [Chan and Vese, 2001] (See Page 35), it ensures that blood vessels and background have approximately constant intensity from I_m . The blood vessels and background of the vessel enhanced image I_m are relatively homogeneous. Additionally, the average image intensity of the blood vessels and background c_1 and c_2 defined on Page 37.

The energy function $E(\phi)$ is minimised by using gradient descent method with respect to ϕ , the formulation is:

$$\frac{\partial\phi}{\partial t} = -\frac{\partial E(\phi)}{\partial\phi}, \quad (3.15)$$

where $\frac{\partial E(\phi)}{\partial \phi}$ is the *Gâteaux* derivative. According to the Euler-Lagrange equations [Aubert and Kornprobst, 2006], and the corresponding gradient flow equation is defined as:

$$\begin{aligned} \frac{\partial \phi}{\partial t} = & \nu \{-U(y_0|x_0, \Theta_0) + U(y_1|x_1, \Theta_1)\} \delta(\phi) + \\ & \lambda_R (\nabla^2 \phi - \text{div}(\frac{\nabla \phi}{|\nabla \phi|})) + \{-\lambda_1 (I_m - c_1)^2 + \\ & \lambda_2 (I_m - c_2)^2\} \delta(\phi) \end{aligned} \quad (3.16)$$

where $\text{div}(\cdot)$ is the divergence operator, which is used to calculate the curvature of the evolving curve by using the spatial derivatives ϕ up to the second order. The Dirac delta function δ is approximated by:

$$\delta(\phi) = \frac{d}{d\phi} H(\phi) = \begin{cases} \frac{1}{2\epsilon} [1 + \cos(\frac{\pi\phi}{\epsilon})], & |\phi| \leq \epsilon \\ 0, & |\phi| > \epsilon. \end{cases} \quad (3.17)$$

3.2.3 Post-processing

Obviously, some background pixels are misclassified as blood vessel pixels. Through investigating the segmentation result of the level set method, we found that most of the small contours are intensity inhomogeneous noise. The length filter [Chanwimaluang and Fan, 2003] is used to eliminate all the background noise. This approach is designed to discard connected groups of pixels which are smaller than a given threshold. Groups of pixels larger than the threshold are retained, for which is defined as blood vessel information. Figure 3.1 (f) shows the final output of the length filter.

3.3 Results

The proposed method described in the previous section was evaluated on two public databases, the DRIVE [Staal et al., 2004] and the STARE [Hoover et al., 2000], with a total of 60 images. The DRIVE dataset includes 40 color images with 768×564 pixels and 8 bits per RGB channel, which were captured by a Canon CR5 non-mydiatic 3CCD camera at 45° of view (FOV) and initially saved in JPEG-format. This database

includes two sets: a test and training set with 20 images each. Both sets have hand-segmented images, and a second independent hand-label is available for the test set. We tested our method on all the 40 images, however, as the dataset site only has the performance of the test set, we will only report the performance of this set. The STARE dataset contains 20 images originally collected by Hoover et al. [Hoover et al., 2000] from the whole STARE database. The first 10 images are abnormal and the remaining 10 are normal. These images were captured by a TOPCon TRV-50 fundus camera at 35° FOV. The size of the image is 700×605 pixels, 8 bits per RGB channel. Both the normal and abnormal images were hand-labeled by two different experts. To evaluate our method, we compare our result with the first expert (AH) for the STARE dataset and with the first manually segmentation for the DRIVE dataset.

Three performance measurements are selected to evaluate different retinal extraction algorithms, (1) True Positive Rate (TPR), (2) False Positive Rate (FPR), and (3) Accuracy Rate (ACC). These metrics are defined as:

$$TPR = \frac{N_{TP}}{N_{TP} + N_{FN}}, \quad FPR = \frac{N_{FP}}{N_{FP} + N_{TN}}, \quad ACC = \frac{N_{TP} + N_{TN}}{N_P + N_N} \quad (3.18)$$

where N_{TP} , N_{FN} , N_{FP} , N_{TN} are the number of true positive, false negative, false positive and true negative, respectively; N_P and N_N represent the total positive (vessel) pixels and negative pixels. The following expressions, TP is the number of vessel pixels that are labelled correctly, FP is the number of non-vessel pixels that are wrongly labeled as vessel pixels, TN is the number of non-vessel pixels that are correctly labeled and finally FN is the number of vessel pixels that are wrongly labelled as non-vessel pixels.

Most of the extraction methods measure the performance using the whole image. However, Staal’s method [Staal et al., 2004] evaluates the performance without including the dark area outside the FOV and Mendonca’s method [Mendonça and Campilho, 2006] estimates the performance on both the whole image and the FOV. The number of the true negatives N_{TN} obtained by measuring within the FOV only is smaller than the number obtained from the whole image, as it is easy to segment the area outside

Method	TPR	FPR	ACC	TPR	FPR	ACC
	DRIVE			STARE		
2 nd Human observer [Mendonça and Campilho, 2006] [Martinez-Perez et al., 2007]	0.7761	0.0275	0.9473	0.8951	0.0438	0.9522
Supervised methods						
Niemeijer [Niemeijer et al., 2004]	0.6898	0.0304	0.9417	-	-	-
Staal [Staal et al., 2004]	0.7194	0.0227	0.9442	0.6970	0.0190	0.9516
Soares [Soares et al., 2006]	0.7332	0.0218	0.9466	0.7207	0.0253	0.9480
Ricci [Ricci and Perfetti, 2007]	0.7750	0.0280	0.9595	0.9030	0.0610	0.9646
Marin [Marín et al., 2011]	0.7067	0.0199	0.9452	0.6944	0.0181	0.9526
Unsupervised methods						
Chaudhuri [Chaudhuri et al., 1989]	-	-	-	0.6134	0.0245	0.9384
Hoover [Hoover et al., 2000]	-	-	-	0.6747	0.0435	0.9275
Mendonca [Mendonça and Campilho, 2006]	0.7344	0.0236	0.9463	0.6996	0.0270	0.9479
Martinez [Martinez-Perez et al., 2007]	0.7246	0.0345	0.9344	0.7506	0.0431	0.9410
Zhang [Zhang et al., 2010]	0.7120	0.0276	0.9382	0.7177	0.0247	0.9484
Azzopardi [Azzopardi et al., 2015]	0.7655	0.0296	0.9442	0.7716	0.0299	0.9497
Roychowdhury [Roychowdhury et al., 2015]	0.7390	0.0220	0.9490	0.7320	0.0160	0.9560
Zhao [Zhao et al., 2015]	0.7420	0.0180	0.9540	0.7800	0.0220	0.9560
Our method without Gaussian Mixture term	0.7318	0.0234	0.9468	0.7156	0.0240	0.9483
Our method	0.7719	0.0204	0.9548	0.7756	0.0204	0.9574

Table 3.1: Performance of the segmentation methods on the DRIVE and STARE datasets

Method	TPR	FPR	ACC
Normal images			
Chaudhuri [Chaudhuri et al., 1989]	0.7335	0.0218	0.9486
Hoover [Hoover et al., 2000]	0.6766	0.0338	0.9324
Mendonca [Mendonça and Campilho, 2006]	0.7258	0.0209	0.9492
Soares [Soares et al., 2006]	0.7554	0.0188	0.9542
Zhang [Zhang et al., 2010]	0.7526	0.0221	0.9510
Roychowdhury [Roychowdhury et al., 2015]	0.7571	0.0123	0.9586
Our method without Gaussian Mixture Term	0.7464	0.0224	0.9518
Our method	0.7921	0.0188	0.9607
Abnormal images			
Chaudhuri [Chaudhuri et al., 1989]	0.5881	0.0384	0.9276
Hoover [Hoover et al., 2000]	0.6736	0.0528	0.9211
Mendonca [Mendonça and Campilho, 2006]	0.6733	0.0331	0.9388
Soares [Soares et al., 2006]	0.6869	0.0318	0.9416
Zhang [Zhang et al., 2010]	0.6828	0.0273	0.9458
Roychowdhury [Roychowdhury et al., 2015]	0.7062	0.0192	0.9535
Our method without Gaussian Mixture Term	0.6848	0.0264	0.9456
Our method	0.7591	0.0220	0.9541

Table 3.2: Performance of vessel segmentation method on the STARE dataset (normal versus abnormal images)

of FOV and which occupies around 25% of the whole image pixels in both the public datasets. It only affects the measurements FPR and ACC.

3.3.1 Performance of blood vessel segmentation

In order to prove that the hybrid region based terms of our method are necessary, we compared the performance of the proposed method with the performance of this method without the Gaussian mixture model on both STARE and DRIVE datasets. As shown in Table 3.1 and 3.2, it proves that our proposed method performs much better than the proposed method without the Gaussian mixture term.

Table 3.1 compares our segmentation method with the alternative methods, using TPR, FPR and ACC on DRIVE and STARE datasets for the comparison. On the

Drive dataset, the average accuracy of our method is higher than the other unsupervised learning methods and most of other supervised learning methods except Ricci et al. [Ricci and Perfetti, 2007]. For the supervised learning methods, a learning process on the training sets is needed before doing the experiments on a new dataset. The performance of these methods generally depends on the training set. In other words, if the training images are similar to the test images, the performance will be better. In terms of the FPR, our method is only inferior to the methods of Zhao et al. [Zhao et al., 2015] and Marin et al. [Marín et al., 2011] with 0.24% and 0.05% differences, respectively. Finally, the TPR is only slightly inferior to the 2nd Human observer with 0.42% difference. Although our method does not have the best performance, the overall performance from the three measurement is still comparable with the labelling by 2nd Human observer with ACC= 0.9473, FPR=0.0275 and TPR=0.7761 on comparison with the ground truth.

The results obtained on the STARE dataset are shown in Table 3.1. All the segmentation methods were tested on all the 20 images except that Staal et al. [Staal et al., 2004] only tested on 19 (10 healthy and 9 unhealthy) images. We consider the 2nd Human observer labelled as the target performance level (ACC=0.9522, FPR=0.0438 and TPR=0.8951) with the first observer labelled as the ground truth in Table 2. Our method achieves the best performance as measured by average accuracy, when compared with all other unsupervised methods. However, our method is marginally inferior to the supervised technique presented by Ricci et al. [Ricci and Perfetti, 2007] with 0.72% difference. Regarding the FPR, our method is better than all the other methods except the Staal’s method [Staal et al., 2004], Marin’s method [Marín et al., 2011], and Roychowdhury’s method [Roychowdhury et al., 2015]. Finally, in terms of TPR, our method is only slightly inferior to the unsupervised method Zhao et al. [Zhao et al., 2015] and supervised method Ricci et al. [Ricci and Perfetti, 2007].

The performance of the normal and abnormal sets from the STARE dataset are compared in Table 3.2. The average accuracy rate of our method on the normal and

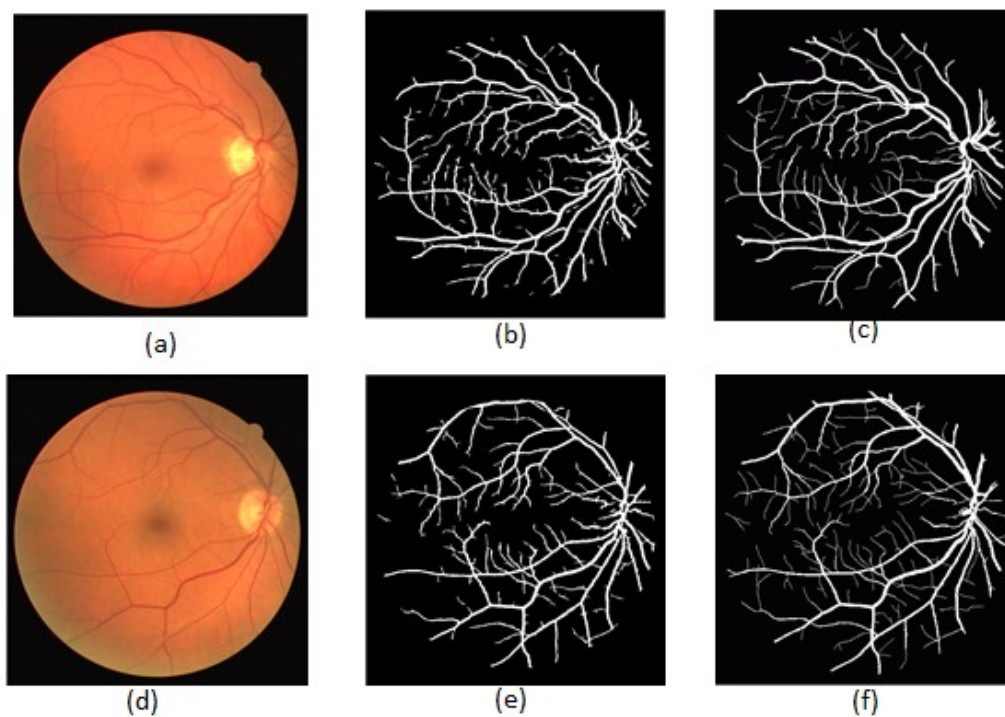


Figure 3.2: The DRIVE dataset: (a, d) Retinal images. (b, e) Our segmentation results. and (c, f) Ground truth image.

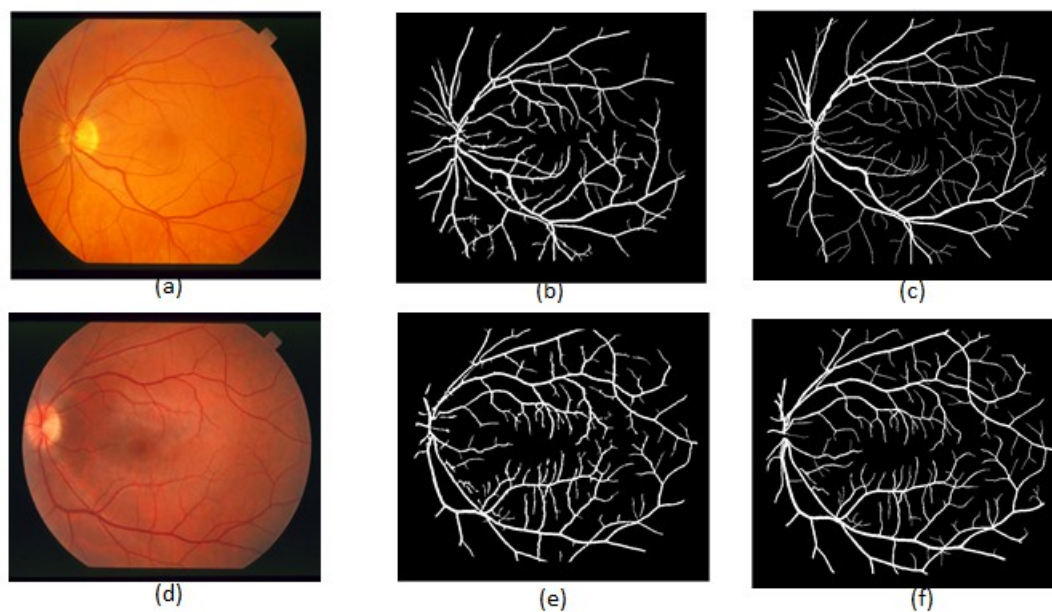


Figure 3.3: The STARE dataset (Normal): (a, d) Retinal images. (b, e) Our segmentation results. and (c, f) Ground truth images.

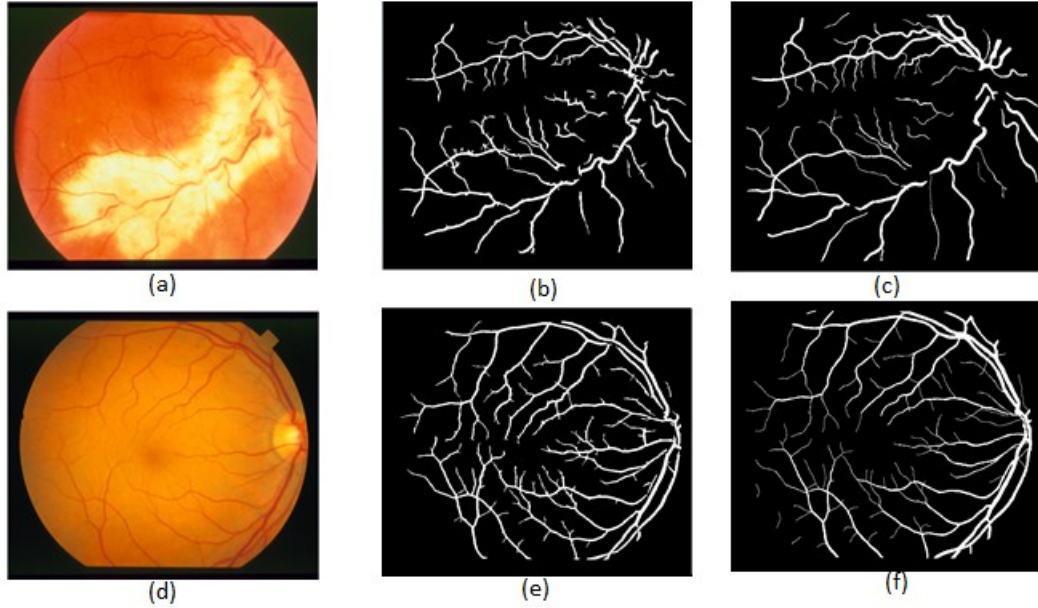


Figure 3.4: The STARE dataset (Abnormal): (a, d) Retinal images. (b, e) Our segmentation results. and (c, f) Ground truth images.

abnormal sets is better than that of all the other methods. In terms of the TPR, our method achieves the best result over all the other methods on both normal and abnormal sets. In terms of the FPR, our method is only slightly inferior to Roychowdhury’s method [Roychowdhury et al., 2015] with 18% difference on the abnormal set, while on the normal set, our method is slightly inferior to Roychowdhury et al. [Roychowdhury et al., 2015] and achieves the same result as Soares et al. [Soares et al., 2006]. An overview of the results on the STARE dataset, our proposed method can work on both normal and abnormal sets and get relatively good results.

Figure 3.2-3.4 illustrate the segmentation results of our proposed method and ground truth images from DRIVE and STARE datasets. Fig 3.2 illustrates the output images of our proposed method and ground truth images for the DRIVE dataset. Figure 3.3 and Figure 3.4 display the output images with ground truth images on normal set and abnormal set of the STARE dataset, respectively.

Finally, our approach is implemented on MATLAB. The computation time of our algorithm is less than 75 seconds for an image from the DRIVE dataset, and less than

80 seconds for a STARE image, on a MAC OX X. The computational complexity is $O(n \log(n))$, n is the image.

3.4 Conclusions

In this chapter, we have presented a level set based blood vessel segmentation method, which incorporates the Gaussian mixture information, region information and distance regularisation information. The method was implemented in a typical three-staged process together with the pre-processing and post-processing to enhance the blood vessel information and the contrast between vessel and background, and remove background noises.

We have evaluated our method against alternative methods on two publicly available datasets: the STARE dataset and the DRIVE dataset. The comparison results demonstrate that the proposed approach has the following advantages: (1) It performs equally well on different datasets and on both healthy and unhealthy images, while many previous methods perform poorly on unhealthy images. (2) It is capable of extracting the blood vessels inside the optic disc and removing the noise of the optic disc boundary, other methods have difficulty in retaining this boundary. (3) It can detect more small branch vessels compared to other methods.

The key attributes of this chapter are: (1) In order to retain the images of the blood vessels inside the optic disc and remove the optic disc interference, the difference image is calculated to compensate. (2) The hybrid region information from the difference image and enhanced image are integrated into the level set method to keep the small branch vessels and compensate the intensity inhomogeneity. (3) The negative log likelihood of the blood vessels and background probabilities are computed according to the prior GMM parameters as a Gaussian mixture region term, and the GMM parameters set is reconstructed on level set iteration.

In this chapter, the Bayesian level set method is proposed and applied to detect the

blood vessels, which are one of the most important retinal structures from a fundus image. The optic disc is another important retinal structure of a fundus image. It is important and necessary to segment the optic disc from a fundus image; this is the topic of the next chapter.

Chapter 4

Level Set Segmentation of Optic Discs from Retinal Images

The analysis of retinal images can provide important information for detecting and tracing retinal and vascular diseases. We have already proposed a method for segmenting blood vessels from fundus images in last chapter. Therefore, the purpose of this work in this chapter is to design a method that can automatically segment the optic disc, which is another important retinal structure of a fundus image. The template matching method is used to approximately locate the optic disc centre, and the blood vessels are extracted to reset the centre of the optic disc. This is followed by applying the level set method, which incorporates the edge term, distance regularisation term and shape-prior term, to segment the shape of the optic disc from retinal images. Seven measurements are used to evaluate the performance of the methods including our method. The effectiveness of the proposed method is evaluated against alternative methods on three public data sets DRIVE, DIARETDB1 and DIARETDB0. The results show that our method outperforms state-of-the-art methods on these datasets.

The work included in this chapter was previously published in [Wang et al., 2015a], lead-authored by the author of this thesis, who made substantial contributions to the conception, data collection and processing and writing-up, and sole contributions to

the implementation and result analysis.

4.1 Introduction

Glaucoma, predicted to affect about 70 million people around the world by 2020 [JMJ, 2002], is one of the major causes of blindness in the world. This disease manifests by gradual degeneration of the retinal ganglion cell axons and cupping of the optic disc. Thus the optic disc nerve is an important structure in glaucoma analysis. Over the past years, glaucoma experts have analysed the amount of cupping using manual planimetry on stereo colour photographs of the optic disc nerve. However, the manual planimetry of the optic disc nerve is time consuming and can be affected by human error. Thus, a reliable automated method for the optic disc segmentation, which preserves various optic disc shapes, is attractive for computer aided-diagnosis and for large-scale retinal disease screening.

In the literature, numerous studies have been published on automated segmentation of the optic disc. Shape based template matching is one of the earliest methods. This method models the optic disc as a circular or elliptical object [Abdel-Ghafar and Morris, 2007, Lalonde et al., 2001, Chrástek et al., 2002, Sekhar et al., 2008, Zhu and Rangayyan, 2008, Pallawala et al., 2004]. The performance of this method is affected by the presence of the blood vessels inside the optic disc region. To overcome these limitations, the images of the blood vessels are removed by using a morphological operation in [Abdel-Ghafar and Morris, 2007]. Nevertheless, the shape based modelling approach of the optic disc extraction is not effective due to the intensity inhomogeneity and the changes of the disc shape caused by the exudates present in abnormal images.

To address the problem of shape irregularity and intensity inhomogeneity, several gradient based active contour methods have been developed [Lowell et al., 2004, Osareh et al., 2002, Novo et al., 2009]. Those methods initialise the contour automatically or manually and performed the deformation of the contour with an energy functional

derived from the image gradient. Then a gradient vector flow based contour model is used to detect the optic disc boundary, and the energy functional is minimised. This process is achieved using pre-processing step or incorporating a circular or elliptical shape constraint term into the segmentation algorithm to model the optic disc. To further improve the active contour method by handling the local gradient minima, a variational level set based deformable model was developed to smooth the segmentation with an ellipse fitting operation [Wong et al., 2008]. This process either incorporates the shape model into the energy formulation or uses a post-processing step. However, a limitation of this method is that it may not perform well on these images with irregular shapes of optic discs.

Model free snake methods are developed to effectively segment any irregular disc shape using a supervised classification [Xu et al., 2007, Li and Chutatape, 2003, Li and Chutatape, 2004]. These methods classify the contour points by using a supervised manner into an edge point cluster or an uncertain point cluster in each evolution [Joshi et al., 2011]. The uncertain point cluster groups the points belonging to the blood vessel region. To address the local gradient variation, the deformation of each point used global and local information. Though this method produces good segmentation results on normal and irregular optic disc shapes, the segmentation accuracy is sensitive to the contour initialisation.

The model proposed by Shah et al. [Mumford and Shah, 1989] has been widely used in region based active contour to overcome the local gradient variation, the sensitivity to contour initialisation and the noise. This region based active contour approach [Chan and Vese, 2001] applies statistical models to define both the foreground and the background before minimising the energy functional. For example, the method proposed in [Joshi et al., 2010] achieved a good segmentation performance but it was unable to accurately segment the boundary of images with smooth region transition between the optic disc area and the background. To address this problem, the Chan-Vese method [Chan and Vese, 2001] was incorporated with a circular shape into the

segmentation formulation. Tang et al. [Tang et al., 2006] developed an automatic method to segment the papilla using the combination the Chan-Vese model and an elliptic shape restraint to ensure that the evolving curve stays an ellipse. Though this method shows a good performance in detecting the papilla shapes, restricting the segmentation to an elliptic shape may adversely affect the segmentation of irregular optic disc shapes.

In order to improve the segmentation of the optic disc boundary, we present in this chapter a novel method by combining the template matching model and the level set method. The segmentation formulation incorporates edge, distance regularisation and shape-prior terms respectively, making it possible to segment the optic disc with large gradient near the boundary and preserve various optic disc shapes.

4.2 Optic disc centre detection

Inspired by the method reported by Lowell et al. [Lowell et al., 2004], the template matching method is used to locate the approximate optic disc centre. Figure 4.1 shows the process to locate the optic disc centre. There are two main stages for the optic disc centre detection: (1) template matching, and (2) relocating the optic disc centre.

The size of the optic disc varies from dataset to dataset. In order to ensure a fixed scale for the optic disc, we rescale the original retinal images into $570 \times 760 \times 3$ (Figure 4.1 (a)). The I channel, which contains the intensity information in the HSI colorspace, is extracted. Then, the morphological closing operation is applied to remove the blood vessels, and the closed image is shown in Figure 4.1 (c). A 201×201 size binary image is used as a template (Figure 4.1 (d)). This is followed by correlating the template with the closed image. In this work, the full Pearson-R correlation [Lowell et al., 2004] is used to explain the variations of the mean intensity and contrast, the formulation is

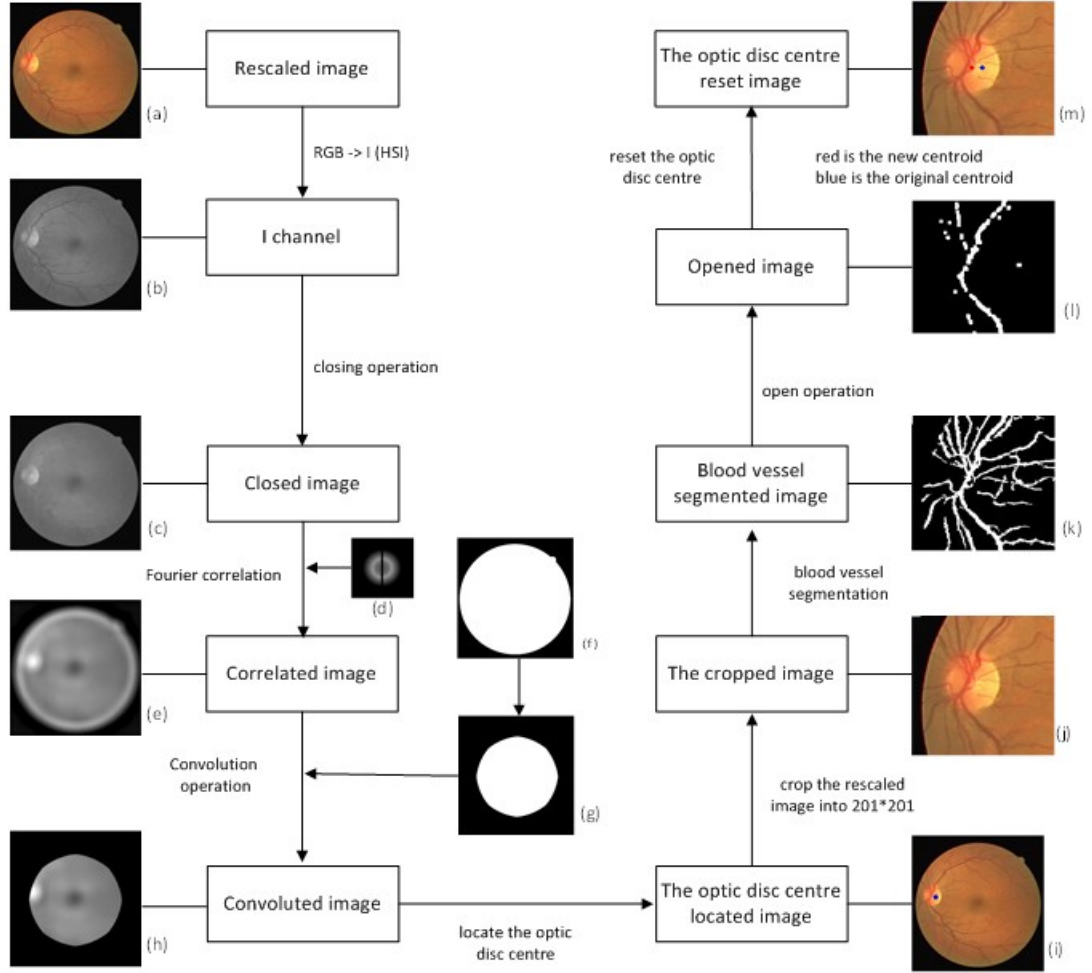


Figure 4.1: The process to locate the optic disc centre. (a) Rescaled image. (b) The I channel image. (c) Closing operation of I channel. (d) The template with the size of 201×201 . (e) The Fourier correlated image. (f) The mask of rescaled image. (g) The border eroded image. (h) The convoluted image. (i) The optic disc centre located image. (j) The cropped image from F_r with the size of 201×201 . (k) The blood vessel segmented image. (l) Open operation of vessel segmented image. (m) The optic disc centre reseted image.

defined as:

$$C_{i,j} = \frac{\sum_{x,y} (F_c(x,y) - \bar{F}_c(x,y)) (F_t(x-i, y-j) - \bar{F}_t)}{\sum_{x,y} (F_c(x,y) - \bar{F}_c(x,y))^2 \sum_{x,y} ((F_t(x-i, y-j) - \bar{F}_t)^2)} \quad (4.1)$$

where F_c is the closed image, \bar{F}_t and \bar{F}_c are the mean value of the template F_t and the

area covered by F_t , respectively. The correlated image is shown in Figure 4.1 (e). The peak of the image is the approximate centre of the optic disc. However, it is obvious that the near-circular rim is with high intensity. In order to eliminate the effect of the rim, an eroded image (see Figure 4.1 (g)) is used to convolute with the correlated image to remove the near circular rim area (Figure 4.1 (e)). The eroded image is obtained from the mask (Figure 4.1 (f)) by using morphological erode operation. The Figure 4.1 (h) shows the convoluted image.

After the template matching method, the approximate centre of the optic disc is located by detecting the peak of the convoluted image. The optic disc centre located image is shown in Figure 4.1 (i). This is followed by cropping the rescaled image into $201 \times 201 \times 3$ by using the peak as the centroid. Figure 4.1 (j) shows the cropped image. As the centre of the optic disc is usually located around the blood vessel and the level set method is sensitive to the initialisation, the blood vessel information is extracted to reset the centroid by using the method defined in last section. The blood vessel segmented image is shown in Figure 4.1 (k). After that, the morphological open operation is applied to prune small branches of vessels and keep the main arcade of blood vessels, Figure 4.1 (l) shows the opened image. We let (c_x, c_y) as the approximate centre of the optic disc. According to the experiments, we assume that c_y is already located at the centroid of the optic disc. Therefore, we keep the y value of the approximate centre unchanged ($c_{y'}$) and find a new c_x value according to $F_o(c_{x'})$. The optic disc reset image is shown in Figure 4.1 (m), and the red point of the image is the new centroid and the blue one is the original centre.

4.3 Optic Disc Extraction

We perform the segmentation using the grey level image, which contains all the information necessary. However, the high contrast of the blood vessel inside the optic disc misguides the segmentation energy functional and breaks the continuity of the optic

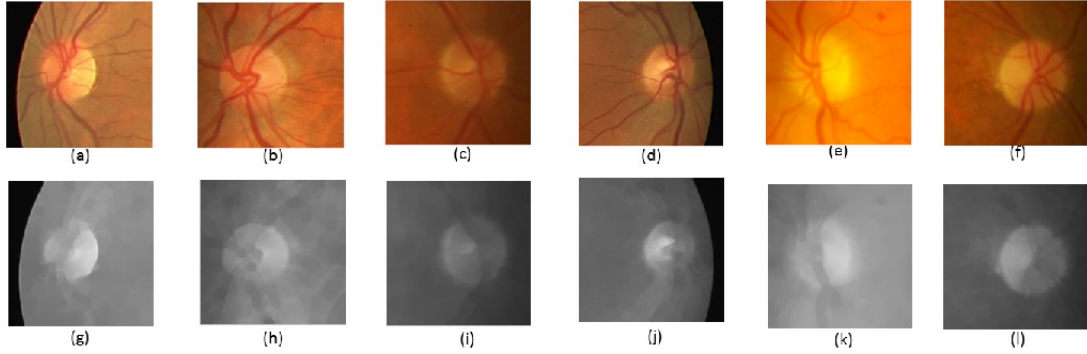


Figure 4.2: Morphological close operation on the cropped retinal images. The first row contains the input images, the second row contains the closed images.

disc boundary. Therefore, we apply the morphological closing operation to remove the blood vessels. Figure 4.2 shows sample images before and after the closing operation. The prominence of the blood vessels is reduced but they can still be seen.

Our aim is to segment the optic disc from the vessel removed image. Let Ω be the image domain and ϕ be a level set function. To obtain a better segmentation, we develop an energy functional as:

$$E(\phi) = E_S(\phi) + E_E(\phi) + E_R(\phi), \quad (4.2)$$

Each term of the energy functional models a different aspect of the problem. The first term E_S is a shape prior term, which is used to compensate these intensity inhomogeneities inside the optic disc due to the intensity inhomogeneity after the blood vessel removal. In order to locate the boundary of the optic disc accurately, we incorporate edge-based information into the energy formulation. The edge based term E_E adapts the Li et al's model [Li et al., 2010] (See Page 37), because the optic disc has significant edge information. The last term E_R is a distance regularisation term, which keeps the optic disc boundary smooth.

4.3.1 Shape prior Term

The shape-prior term was first introduced by Azadeh et al. [Yazdanpanah et al., 2009]. Because the intensity inside the optic disc is inhomogeneous even after vessel removal, the shape-prior term is incorporated to compensate these intensity inhomogeneities inside the optic disc. Usually, the shape of the optic disc is circular. Therefore, a circular prior term is applied to assist the algorithm when the edge information is insufficient for detecting the optic disc boundary. The square distance from a point (x, y) to the shape constraining boundary is defined as:

$$D(x, y) = [(x - c_{x'})^2 + (y - c_{y'})^2 - r^2] \quad (4.3)$$

where $(c_{x'}, c_{y'})$ is the optic disc centre, and r is the approximate radius of the optic disc according to the level set function ϕ .

The circular prior term is used to encourage the boundary of the level set function ϕ to lie on a circle. Therefore, the shape term can be formulated as:

$$E_S(\phi) = \lambda_S \int_{\Omega} D(x, y) \delta_{\epsilon}(\phi(x, y)) |\nabla \phi(x, y)| dx dy \quad (4.4)$$

where $\lambda_S \in \mathcal{R}$ is a constant coefficient, and δ_{ϵ} is the Dirac delta function. This term calculates the line integral of D along the zero level boundary of ϕ . It keeps the boundary of ϕ circular. The Dirac delta function δ_{ϵ} is defined as Page 55.

4.3.2 Distance Regularisation Term

The accuracy of the located boundary of the optic disc is improved by smoothing. Thus the following distance regularisation term is added to the energy functional:

$$E_R(\phi) = \lambda'_R E'_R(\phi) + \lambda''_R E''_R(\phi), \quad (4.5)$$

where λ'_R and λ''_R are positive valued parameters. The first term $E'_R(\phi)$ computes the contour length of the zero level set ϕ to smooth the boundary of the optic disc. However, the penalty term from Li et al [Li et al., 2005] is added to keep the zero level set function ϕ close to the optic disc boundary. The terms of $E'_R(\phi)$ and $E''_R(\phi)$ are defined by:

$$E'_R(\phi) = \int_{\Omega} \delta_{\epsilon}(\phi(x, y)) |\nabla \phi(x, y)| dx dy, \quad (4.6)$$

and

$$E''_R(\phi) = \int_{\Omega} \frac{1}{2} (|\nabla \phi(x, y)| - 1)^2 dx dy. \quad (4.7)$$

The second term $E''_R(\phi)$ is used to maintain the signed distance property $|\nabla \phi| = 1$. This term will be minimised when $|\nabla \phi| = 1$.

4.3.3 Energy minimisation

The energy terms defined by a shape term, an edge term and a regularisation term, are substituted into 4.2, and our energy model of $E(\phi)$ can be rewritten as:

$$\begin{aligned} E_{\phi} = & \lambda_S \int_{\Omega} D(x, y) \delta_{\epsilon}(\phi(x, y)) |\nabla \phi(x, y)| dx dy + \lambda \int_{\Omega} g \delta_{\epsilon}(\phi(x, y)) |\nabla \phi(x, y)| dx dy + \\ & \alpha \int_{\Omega} g H_{\epsilon}(-\phi(x, y)) dx dy + \lambda'_R \int_{\Omega} \delta_{\epsilon}(\phi(x, y)) |\nabla \phi(x, y)| dx dy + \\ & \lambda''_R \int_{\Omega} \frac{1}{2} (|\nabla \phi(x, y)| - 1)^2 dx dy \end{aligned} \quad (4.8)$$

where the Heaviside function H_{ϵ} is expressed as Page 54.

In calculus of variations [Aubert and Kornprobst, 2006], minimising the energy functional of $E(\phi)$ with respect to ϕ by using gradient descent method as follows:

$$\frac{\partial \phi}{\partial t} = - \frac{\partial E(\phi)}{\partial \phi} \quad (4.9)$$

where $\frac{\partial E(\phi)}{\partial \phi}$ is the *Gâteaux* derivative [Aubert and Kornprobst, 2006] of the energy

function $E(\phi)$. According to Euler-Lagrange equations [Aubert and Kornprobst, 2006], the gradient flow is expressed by :

$$\begin{aligned} \frac{\partial \phi}{\partial t} = & \lambda_S (\nabla D |\nabla \phi| + D \operatorname{div}(\frac{\nabla \phi}{|\nabla \phi|})) \delta_\epsilon(\phi) + \\ & \{ \lambda (\nabla g |\nabla \phi| + g \operatorname{div}(\frac{\nabla \phi}{|\nabla \phi|}) + \alpha g) \} \delta_\epsilon(\phi) + \\ & \lambda'_R \operatorname{div}(\frac{\nabla \phi}{|\nabla \phi|}) \delta_\epsilon(\phi) + \lambda''_R (\nabla^2 \phi - \operatorname{div}(\frac{\nabla \phi}{|\nabla \phi|})) \end{aligned} \quad (4.10)$$

where ∇ is the gradient operator, $\operatorname{div}(\cdot)$ is the divergence operator, which is used to calculate the curvature of the evolving curve by using the spatial derivatives ϕ up to the second order. The curvature $\operatorname{div}(\frac{\nabla \phi}{|\nabla \phi|})$ as follows:

$$\operatorname{div}(\frac{\nabla \phi}{|\nabla \phi|}) = \frac{\phi_x^2}{\phi_x^2 + \phi_y^2 + \varpi} + \frac{\phi_y^2}{\phi_x^2 + \phi_y^2 + \varpi} \quad (4.11)$$

ϕ_x and ϕ_y are the directional derivative of ϕ in x direction and y direction. In order to prevent the denominator to be zero, ϖ is a small positive number.

4.4 Experimental Results

4.4.1 Dataset

The proposed method was evaluated on three public datasets, the DRIVE [Staal et al., 2004], the DIARETDB0 [Kauppi et al., 2006] and the DIARETDB1 [Kauppi et al., 2007], with a total of 259 images.

The DRIVE dataset includes 40 fundus images with 768×564 pixels and 8 bits per RGB channel, which were captured by a Cannon CR5 non-mydratic 3CCD camera at 45° of view (FOV) and initially saved in JPEG-format. This database includes two sets: a test and training set with 20 images each. Both sets have blood vessel hand-segmented images, and a second expert's hand-labelling is available for the test set.

The DIARETDB0 dataset consists of 130 color images where 20 of them are normal and 110 of them contain signs of the diabetic retinopathy. These images were captured by 50° FOV digital fundus cameras with unknown camera settings (flash intensity, shutter speed, aperture, gain), and have a size of 1500×1152 pixels.

The DIARETDB1 dataset contains 89 retinal images, of which 84 have at least one indication of diabetic retinopathy. The images were captured with a digital fundus camera at 50° FOV with varying imaging settings (flashing intensity, shutter speed, aperture, gain). The size of the image is 1500×1152 pixels, 8 bits per RGB channel. In addition, the dataset provides ground truth on hard exudates, hemorrhages, red small dots and soft exudates obtained from four experts, one for each area.

None of the three datasets provide the ground truth for the optic disc. In order to evaluate the performance of the proposed segmentation method, we created hand labeled sets for the three datasets according to an expert’s guidance. The optic disc ground truth for all of the three datasets available at ¹.

4.4.2 Performance measures

Seven performance measurements are selected to evaluate different retinal extraction algorithms. Four of them are sensitivity (R_{sen}), specificity (R_{spe}), predictive value (P_v) and overlapping ratio (O_r), respectively. These metrics are defined as:

$$R_{sen} = \frac{N_{TP}}{N_{TP} + N_{FN}} \quad (4.12)$$

$$R_{spe} = \frac{N_{TN}}{N_{TN} + N_{FP}} \quad (4.13)$$

$$P_v = \frac{N_{TP}}{N_{TP} + N_{FP}} \quad (4.14)$$

$$O_r = \frac{area(A \cap B)}{area(A \cup B)} \quad (4.15)$$

where N_{TP} , N_{FN} , N_{FP} , N_{TN} are the number of true positive, false negative, false positive and true negative, respectively; A and B represent the optic disc region seg-

¹<http://www.brunel.ac.uk/cspgccw>

mented by the human expert and our proposed method, respectively. The term, TP is defined as all the vessel pixels that are labelled correctly, FP is all the non-vessel pixels that are wrongly labeled as vessel pixels, TN is the number of non-vessel pixels that are correctly labeled and finally FN is the number of vessel pixels that are wrongly labelled as non-vessel pixels. The sensitivity (R_{sen}) and specificity (R_{spe}) measures are calculated to show the percentage of true positive and true negative, respectively. The predictive value (P_v) [Walter et al., 2002] predicts the probability that a pixel is correctly classified as exudate. Finally, overlapping ratio (O_r) of the optic disc region between the ground truth and the output of the proposed method is computed.

This is followed by computing the Euclidean distance between the optic disc centroid obtained by the proposed method and the centre of the ground truth region. The Euclidean distance (ED) is:

$$ED(A, B) = \sqrt{(x_1 - x_2)^2 + (y_1 - y_2)^2} \quad (4.16)$$

where (x_1, y_1) and (x_2, y_2) are the centroids of the A and B , respectively.

In addition, the mean absolute distance (MAD) between the optic disc boundary extracted by the proposed method and the ground truth is calculated as a measurement of detection accuracy [Chalana et al., 1996]. The formulation of the MAD is defined as:

$$MAD(A_c, B_c) = \frac{1}{2} \left\{ \frac{1}{n} \sum_{i=1}^n d(a_i, B_c) + \frac{1}{m} \sum_{i=1}^m d(b_i, A_c) \right\} \quad (4.17)$$

Where A_c and B_c are sets of points from the optic disc contour of our segmentation method and ground truth, i.e. $A_c = \{a_1, a_2, \dots, a_n\}$ and $B_c = \{b_1, b_2, \dots, b_m\}$. Furthermore, $d(a_i, B_c)$ is the minimum distance from a_i to the set of points B_c . Finally, the last measurement is the computation time, which indicates the efficiency of the method.

Methods	Detection performance (DRIVE dataset) (%)	Detection performance (DIARETDB1 dataset) (%)	Detection performance (DIARETDB0 dataset) (%)
Sopharak[Sopharak et al., 2008]	95	59.55	-
Walter[Walter et al., 2002]	77.5	92.13	-
Seo[Seo et al., 2004]	95	80.89	-
Kande[Kande et al., 2008]	95	86.51	-
Stapor[Stapor et al., 2004]	87.5	78.65	-
Lupascu[Lupascu et al., 2008]	95	88.76	-
Welfer[Welfer et al., 2013]	100	97.7	-
Our method	100	97.75	97.7

Table 4.1: The optic disc detection performance on the DRIVE, DIARETDB0 and DIARETDB1 datasets.

4.4.3 Results

Table 4.1 shows the performance of the optic disc location on the DRIVE, DIARETDB0 and DIARETDB1 datasets. The performance of our method is compared with the alternative methods: Sopharak et al. [Sopharak et al., 2008], Walter et al. [Walter et al., 2002], Seo et al. [Seo et al., 2004], Kande et al. [Kande et al., 2008], Stapor et al. [Stapor et al., 2004], Lupascu et al. [Lupascu et al., 2008] and Welfer et al. [Welfer et al., 2013] taken from [Welfer et al., 2013]. The comparison indicates that the proposed method achieves the best performance in detecting the optic disc. This method can 100% detect the location of the optic disc on DRIVE dataset, 97.75% on DIARETDB1 dataset (2 out of 89 images), and 97.7% on DIARETDB0 dataset (3 out of 130 images). Welfer et al. [Welfer et al., 2013] obtain almost the same result as the template matching method on the DRIVE and DIARETDB1 datasets. The performances of the other methods are all inferior to this method.

Table 4.2 compares the performance of the optic disc segmentation with the state of the art methods: Sopharak et al. [Sopharak et al., 2008], Walter et al. [Walter et al., 2002], Seo et al. [Seo et al., 2004], Kande [Kande et al., 2008], Stapor et al. [Stapor et al., 2004], Lupascu et al. [Lupascu et al., 2008] and Welfer et al. [Welfer et al., 2013]

taken from [Welfer et al., 2013]. All of the other methods are tested on two datasets: DRIVE and DIARETDB1 datasets only. We use DIARETDB0 dataset to evaluate the performance of our method. Our method achieves 89.06% mean overlapping ratio, 94.65% mean sensitivity, 98.89% mean specificity, 93.95% average predictive value, 2.76 mean Euclidean distance and 2.48 mean absolute distance on the dataset.

On the DRIVE dataset, our method for optic disc segmentation has an average sensitivity 92.58%, predictive value 94.23%, overlapping ratio 88.16%, Euclidean distance 3.11 and mean absolute distance 2.52. It outperforms all the alternative methods. However, the value of the average specificity achieved by our method is marginally inferior to the other methods except Kande et al. [Kande et al., 2008] and Stapor et al. [Stapor et al., 2004].

Similarly to the DRIVE dataset, our method achieves the best over all performance on DIARETDB1 dataset. As we can see from the Table 4.2, the proposed method outperforms all the other methods on average sensitivity, predictive value, overlapping ratio, Euclidean distance and mean absolute distance. Nevertheless our method achieves lower average specificity compared to the alternative methods.

Figures 4.3-4.5 illustrate the output images of our proposed method and ground truth images for the DRIVE, DIARETDB1 and DIARETDB0 datasets, respectively.

The proposed approach is implemented on MATLAB R2011b. The average computation time of the algorithm is 17.55 seconds for an image in the DRIVE dataset, 18.25 seconds for an image of DIARETDB1, and 18.3 seconds for an image of DIARETDB0 on Intel Core i5-2500 CPU, clock of 3.3GHz. The computational complexity is $O(n \log(n))$, n is the image.

4.5 Conclusions

We have presented a novel method to detect and remove the optic disc from retinal images. First, the template matching method is used to approximately locate the

Methods	Sens (%)	Spec (%)	Pred (%)	O_r (%)	ED	MAD	Time(s)
DRIVE dataset							
Sopharak							
[Sopharak et al., 2008]	21.04	99.93	93.34	16.88	20.85	23.15	14.92
Walter							
[Walter et al., 2002]	49.88	99.81	86.53	29.32	16.51	14.96	219.60
Seo							
[Seo et al., 2004]	50.29	99.83	84.3	31.09	19.68	14.00	7.23
Kande							
[Kande et al., 2008]	69.99	98.88	52.18	29.66	29.66	12.49	111.74
Stapor							
[Stapor et al., 2004]	73.68	99.20	61.98	33.42	11.12	7.5	43.00
Lupascu							
[Lupascu et al., 2008]	77.68	99.68	88.14	40.01	9.51	9.71	-
Welfer							
[Welfer et al., 2013]	83.54	99.81	89.38	42.54	7.48	5.65	22.66
Our method	92.58	99.26	95.19	88.17	2.46	2.51	17.55
DIARETDB1 dataset							
Sopharak							
[Sopharak et al., 2008]	46.03	99.94	95.93	29.41	6.99	16.86	74.55
Walter							
[Walter et al., 2002]	65.69	99.93	93.95	36.97	13.10	16.03	308.56
Seo							
[Seo et al., 2004]	61.03	99.87	88.78	35.32	13.62	9.84	15.63
Kande							
[Kande et al., 2008]	88.08	98.78	54.48	33.41	21.77	8.50	120.55
Stapor							
[Stapor et al., 2004]	84.98	99.64	80.34	34.08	6.74	6.03	59.72
Lupascu							
[Lupascu et al., 2008]	68.48	99.69	81.17	30.95	16.04	13.81	-
Welfer							
[Welfer et al., 2013]	92.51	99.76	87.60	44.58	4.95	3.91	24.10
Our method	93.24	98.94	94.23	88.16	3.11	2.74	18.25
DIARETDB0 dataset							
Our method	94.65	98.89	93.95	89.06	2.76	2.48	18.3

Table 4.2: The optic disc segmentation performance on DRIVE, DIARETDB0 and DIARETDB1 datasets.

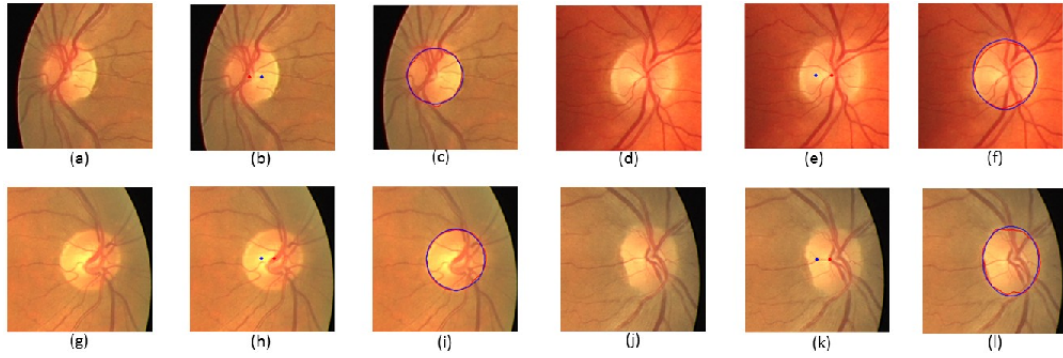


Figure 4.3: The DRIVE dataset: (a, d, g, j) The cropped retinal images. (b, e, h, k) The optic disc centre reseted images. (c, f, i, l) Our segmentation results (Red is our segmentation result, blue is the ground truth).

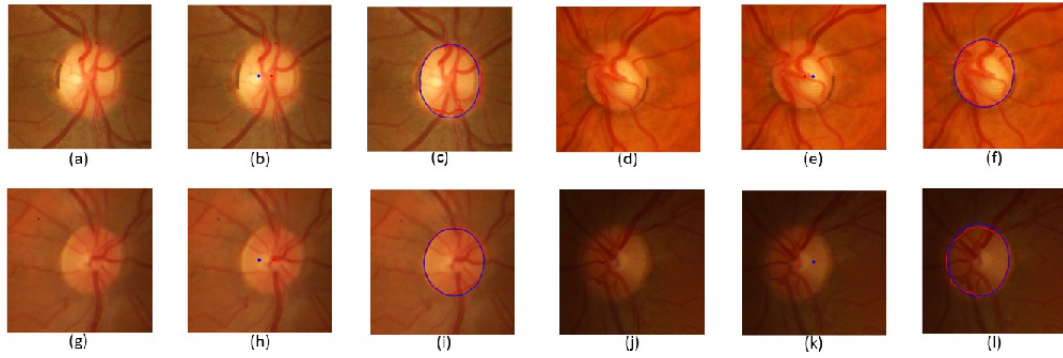


Figure 4.4: The DIARETDB1 dataset: (a, d, g, j) The cropped retinal images. (b, e, h, k) The optic disc centre reseted images. (c, f, i, l) Our segmentation results (Red is our segmentation result, blue is the ground truth).

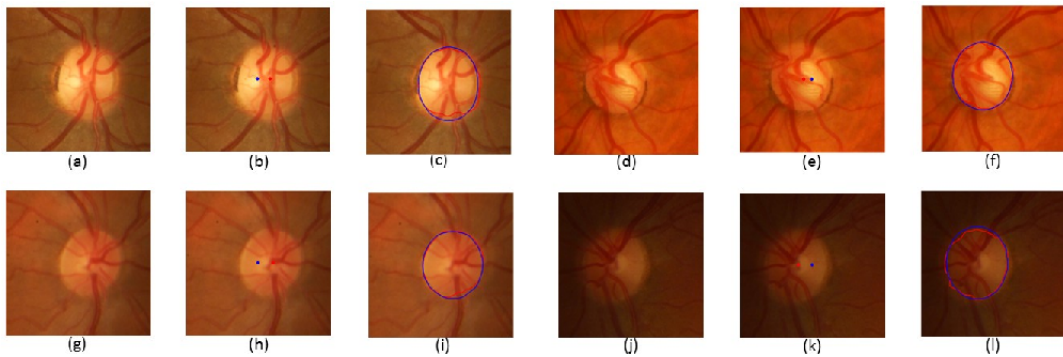


Figure 4.5: The DIARETDB0 dataset: (a, d, g, j) The cropped retinal images. (b, e, h, k) The optic disc centre reseted images. (c, f, i, l) Our segmentation results (Red is our segmentation result, blue is the ground truth).

position of the optic disc. Then, the morphological based method is applied to remove the blood vessels, after which the centroid of the optic disc is reset. Then, the level set method incorporated with shape-prior term, distance regularisation term and edge-based term is used to segment the optic disc.

The effectiveness of our method is evaluated against the-state-of-the-art methods on two public datasets: the DRIVE and DIARETDB1 datasets. The DIARETDB0 dataset is used to evaluate the proposed method. The overall experimental results show that the proposed method outperformed all the alternative methods chosen for comparison. Our method has advantages over the shape-based template matching method as it addresses the intensity inhomogeneity and the obstruction because of the vessels inside the optic disc area. which generally affects the segmentation of the optic disc. Unlike the gradient based active contour methods, the model free snake methods and general region based active contour methods, our method can perform the segmentation of normal and irregular optic disc shapes without constraining the optic disc shape.

In this chapter, the shape constraint level set method is proposed and applied to detect the optic disc, which is a major structure of fundus image. However, the 2D fundus images do not provide enough information for diagnosing eye diseases. The OCT imaging techniques are introduced to provide a clearer information of retina in 3D. Therefore, the tools for 3D retinal structures extraction from 3D OCT images is necessary and important to assist ophthalmologists to diagnose eye diseases in the early stages. The intra-retinal layer segmentation from 3D macular images is the topic of the next chapter.

Chapter 5

Automated Layer Segmentation of 3D Macular Images

Two major retinal structures of fundus images are segmented by using the method we proposed in chapters 3 and 4. However, 2D fundus camera may not capture all the disorders in the retina in the early stages. Spectral-Domain Optical Coherence Tomography (SD-OCT) is a non-invasive imaging modality, which provides retinal structures with unprecedented detail in 3D. In this chapter, we propose an automated segmentation method to detect intra-retinal layers in OCT images acquired from a high resolution SD-OCT Spectralis HRA+OCT (Heidelberg Engineering, Germany). The algorithm starts by removing all the OCT imaging artifacts include the speckle noise and enhancing the contrast between layers using both 3D nonlinear anisotropic and ellipsoid averaging filters. Eight boundaries of the retina are detected by using a hybrid method which combines hysteresis thresholding method, level set method, multi-region continuous max-flow approaches. The segmentation results show that our method can effectively and accurately locate eight retinal layer surfaces for varying quality 3D macular images.

The work included in this chapter was previously published in [Wang et al., 2015b], lead-authored by the author of this thesis, who made substantial contributions to the

conception, data collection and processing and writing-up, and sole contributions to the implementation and result analysis.

5.1 Introduction

Optical Coherence Tomography (OCT) is a powerful biomedical tissue-imaging modality, which can provide a wealth of information, such as structure, blood flow, elastic parameters, change of polarisation state and molecular content [Huang et al., 1991]. Therefore, it has been increasingly useful in diagnosing eye diseases, such as glaucoma, diabetic retinopathy and age-related macular degeneration, which are the most common causes of blindness in the developed countries according to the World Health Organisation (WHO) survey [Organization, 1988]. In order to help ophthalmologists diagnose eye diseases more accurately and efficiently, some medical image processing techniques are applied to extract useful information from OCT data, such as retinal layers, retinal vessels, retinal lesions, optic nerve head, optic cup and neuro-retinal rim. In this work, we focus on the intra-retinal layer segmentation of 3D macular images.

There are two main reasons for intra-retinal layer segmentation [Garvin et al., 2009]. First, the morphology and thickness of each intra-retinal layer are important indicators for assessing the presence of ocular disease. For example, the thickness map of the nerve fiber layer is an important indicator of glaucoma. Second, intra-retinal layer segmentation improves the understanding of the pathophysiology of systemic diseases. For instance, the damage of the nerve fiber layer can provide an indication of brain damage.

However, it is time consuming or even impossible for an ophthalmologist to manually label each layer, specifically for those macular images with complicated 3D layer structures. Therefore, a reliable automated method for layer segmentation is attractive in computer aided-diagnosis. 3D OCT layer segmentation is a challenging problem, and there has been significant effort in this area over the last decade. A number of

different approaches have been developed to do the segmentation, however, no typical segmentation method works equally well on different macular images collected from different imaging modalities.

For most of the existing 3D macular segmentation approaches, a typical two-step process is adopted. The first step is de-noising, which is used to remove the speckle noises and enhance the contrast between layers (usually with a 3D anisotropic diffusion method, 3D median filter, 3D Gaussian filter or 3D wavelet transform). The second step is to segment the layers according to the characteristics of the images, such as shapes, textures or intensities. The existing 3D OCT layer segmentation approaches can be classify into three distinct groups: snake based, pattern recognition based and graph based.

Snake based methods [Kass et al., 1988] attempt to minimise the energy of a sum of internal and external energy of the current contour. These methods work well on those images with high contrast, high gradient and smooth boundaries between the layers, however, the performance is adversely affected by blood vessel shadows, other morphological features of the retina, or irregular layer shapes. Zhu et al. [Zhu et al., 2010] proposed a floating canvas method to segment 3D intra-retinal layers. This method can produce relatively smooth layers, however, it is sensitive to any low gradients between layers. Yazdanpanah et al. [Yazdanpanah et al., 2011] proposed an active contour method, incorporating with circular shape prior information, to segment intra-retinal layer from 3D OCT image. This method can effectively overcome the effects of the blood vessel shadows and other morphological features of the retina, however it cannot work well on those images with irregular layers.

Pattern recognition based techniques perform layer segmentation by using boundary classifier, which is used to classify each voxel either as a layer boundary or a non boundary. The classifier is trained through a learning process by using reference layer boundaries. Fuller et al. [Fuller et al., 2007] designed multi-resolution hierarchical support vector machines (SVMs) to segment OCT retinal layer. However, the performance

of this algorithm is not good enough. It has 6 pixels of line difference and 8% of the thickness difference. Lang et al. [Lang et al., 2013] trained a random forest classifier to segment retinal layers from macular images. However, the performance of the pattern recognition based techniques are highly dependent on training sets.

Graph based methods find the global minimum cut of the segmentation graph, which is constructed with a regional term and a boundary term. Garvin [Garvin et al., 2008] proposed a 3D graph search method by constructing geometric graph with edge and regional information. Five intra-retinal layers were successfully segmented. This method was extended in [Chiu et al., 2010], which combined graph theory and dynamic programming to segment the intra-retinal layers. Eight retinal layer boundaries were located. Although these methods provide good segmentation accuracy, they can not segment all layer boundaries simultaneously and the processing speed is relatively slow. Lee et al. [Lee et al., 2012] proposed a parallel graph search method to overcome these limitations. Kafieh et al. [Kafieh et al., 2013] proposed coarse grained diffusion maps relying on regional image texture without requiring edge based image information. Ten layers were segmented accurately. However, this method has high computational complexity and cannot work well for abnormal images.

In this chapter we propose an automatic approach for segmenting macular layers by using the graph cut and level set method. A de-noising step including the nonlinear anisotropic diffusion approach and ellipsoidal averaging filter is applied to remove speckle noise and enhance the contrast between layers. The segmentation of the layer boundaries is performed by using the combination of classical region based level set method, and multi-region continuous max-flow approaches. All the segmentation techniques use the layers characteristics, such as voxel intensities and positions of layers.

This chapter is organised as follows. A detailed description of the proposed method is presented in Section 2. This is followed by the experimental results in Section 3. Finally, conclusions are drawn in Section 4.

5.2 Methods

Intra-retinal layers are segmented by two major steps: a preprocessing step and a layer segmentation step. Figure 5.1 shows the process of layer segmentation. During the preprocessing step, the nonlinear anisotropic diffusion approach [Gerig et al., 1992] and ellipsoidal averaging filter are applied to 3D macular images to remove speckle noise, enhance the contrast between object and background and remove staircase noise. At the second step, eight intra-retinal boundaries are segmented by using different methods, which include the level set method, hysteresis method, and multi-region continuous max-flow algorithm, according to the characteristics of each layer.

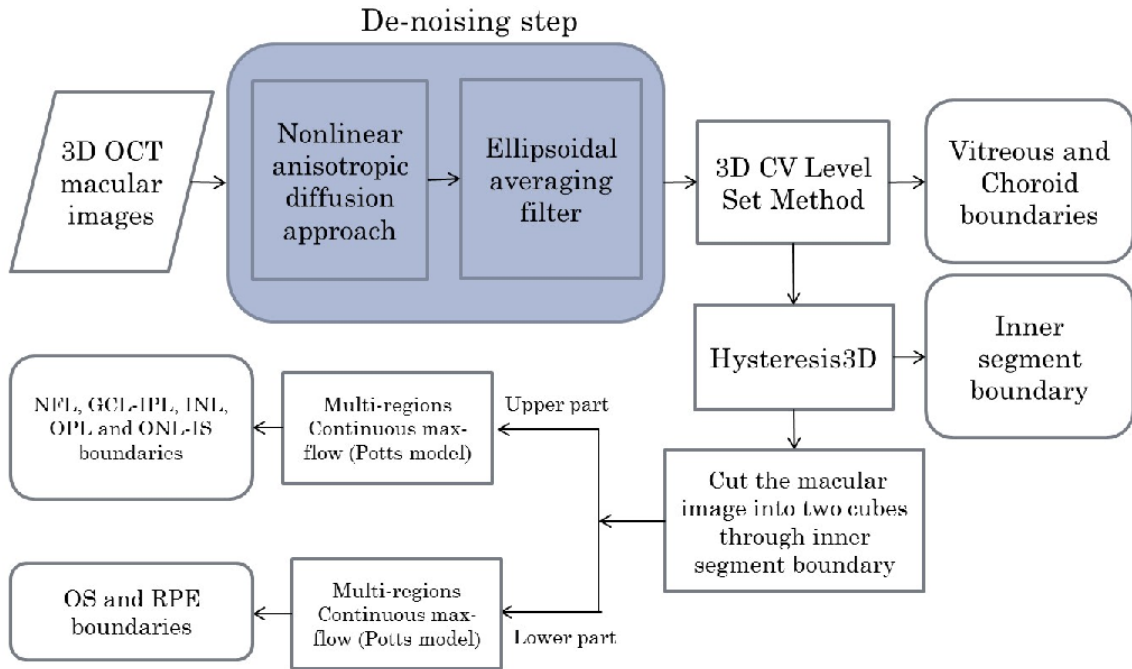


Figure 5.1: Block diagram of retinal layers segmentation process. (NFL: Nerve Fiber Layer, GCL: Ganglion Cell Layer, IPL: Inner Plexiform Layer, INL: Inner Nuclear Layer, OPL: Outer Plexiform Layer, ONL: Outer Nuclear Layer, IS: Inner Segment, OS: Outer Segment, RPE: Retinal Pigment Epithelium)

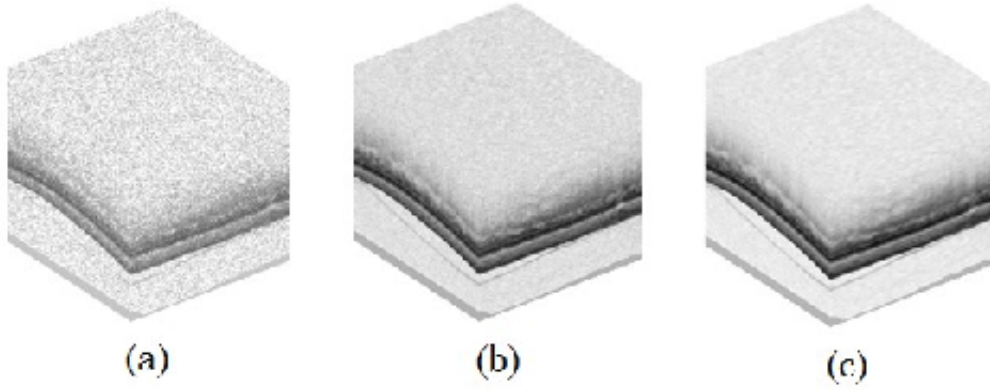


Figure 5.2: a) Original 3D macular image. b) The filtered image by nonlinear anisotropic diffusion. c) The filtered image by ellipsoidal averaging.

5.2.1 Preprocessing

During the OCT imaging of the retina, the speckle noise is introduced simultaneously. Figure 5.2 (a) shows the original 3D macular image, which contains a significant level of speckle noise. The conventional anisotropic diffusion approach (Perona-Malik) [Gerig et al., 1992] is used to remove the speckle noise and sharpen the object boundary. The nonlinear anisotropic diffusion filter is defined as:

$$\frac{\partial}{\partial t} I(\bar{x}, t) = \text{div}[c(\bar{x}, t)\nabla I(\bar{x}, t)] \quad (5.1)$$

where the vector \bar{x} represents (x, y, z) and t is the process ordering parameter. $I(\bar{x}, t)$ is macular voxel intensity. $c(\bar{x}, t)$ is the diffusion strength control function, which is depended on the magnitude of the gradient of the voxel intensity. The function $c(\bar{x}, t)$ is:

$$c(\bar{x}, t) = \exp\left(-\frac{|\nabla I(\bar{x}, t)|^2}{\kappa}\right) \quad (5.2)$$

where κ is a constant chosen according to the noise level and edge strength. Finally, the voxel intensities are updated by the following formula:

$$I(t + \Delta t) = I(t) + \Delta t \frac{\partial}{\partial t} I(t) \quad (5.3)$$

The filtered image is shown in Figure 5.2 (b). Due to the stair-casing (a byproduct of the anisotropic method), the ellipsoidal averaging filter is applied to remove the noise and smooth the images. The filter reduces the amount of intensity variation between one pixel and the next. The filter function is defined as

$$h(x, y, z) = \begin{cases} 1, & \left(\frac{x^2}{(X/2)^2} + \frac{y^2}{(Y/2)^2} + \frac{z^2}{(Z/2)^2} \right) > 1 \\ 0, & \text{otherwise} \end{cases} \quad (5.4)$$

where X, Y, Z are the mask size of x, y, z axis direction of the filter, respectively, x, y and z are the rectangular grid in 3D space and are obtained by using the function as $ndgrid(-X/2 : X/2, -Y/2 : Y/2, -Z/2 : Z/2)$. In our experiments, the size of the filter is set to $[9, 9, 9]$. This is followed by convolution with $2 \times 2 \times 2$ ones array, and we can get the result f . Finally, the filter mask is: $f = f/sum(f)$. The result of this filtering is shown in Figure 5.2 (c).

5.2.2 Vitreous and choroid boundaries segmentation

Due to different characteristics of each layer, different methods are applied to segment different layers. Through the de-noising process, most of the speckle noise is removed and the contrast between background and object is enhanced. The level set method is used to segment the vitreous and the choroid boundaries because it works well when there is large gradient between the retina and background. In this study, the classical region based Chan-Vese model [Chan and Vese, 2001] is used to locate the boundaries of victorious and choroid layer from 3D macular images. The formulation of the energy function of the Chan-Vese method is defined on Page 35.

In calculus of variations [Aubert and Kornprobst, 2006], minimising the energy functional of $E(\phi)$ with respect to ϕ by using gradient descent method:

$$\frac{\partial \phi}{\partial t} = - \frac{\partial E(\phi)}{\partial \phi} \quad (5.5)$$

where $\frac{\partial E(\phi)}{\partial \phi}$ is the *Gâteaux* derivative [Aubert and Kornprobst, 2006] of the energy function $E(\phi)$. The equation of (4) is derived by using Euler-Lagrange equation [Smith et al., 2008], which gives us the gradient flow as follow:

$$\frac{\partial \phi}{\partial t} = - \{ \lambda_1 (I(X) - c_1)^2 - \lambda_2 (I(X) - c_2)^2 \} H(\phi(X)) \quad (5.6)$$

5.2.3 NFL, GCL-IPL, INL, OPL, ONL-IS, OS, RPE (See Page xx) boundaries segmentation

After locating the boundaries of the vitreous and choroid layers, we define a region that includes all the layers see Figure 5.3 (b). Because of the low intensities of the OS-RPE layers, the 3D hysteresis method is used to locate the boundary of IS layer, where two threshold values and a loop are used to produce a connect segmentation results with fewer isolated pixels. A dual thresholding operation using two threshold values (lower and upper) is applied on the reduced images to detect the boundary of IS layer. Furthermore, this method takes advantage of the 3D connectivities by filling image regions and holes to produce a smooth boundary.

In order to reduce the computation load and increase the speed of the segmentation, we further split the region into two parts (upper part (Figure 5.3 (d)) and lower part (Figure 5.3 (c)). From Figure 5.3 (c) and Figure 5.3 (d), looking at the intensity variation between different layers, it is obvious to distinguish layers from each other. The multi-region continuous max-flow (Potts model) is applied to segment both the upper part and lower part, the detail of this method is presented in the following. For the upper part, the NFL, GCL-IPL, INL, OPL and ONL-IS boundaries are segmented. On the other hand, OS and RPE boundaries are located for the lower part.

Graph cut is an interactive image segmentation method, which was first introduced by Boykov et al [Boykov and Jolly, 2001]. This method minimise a segmentation function, which consists of a regional term and a boundary term, to find the globally optimal cut of images. The regional term is defined by computing the likelihoods

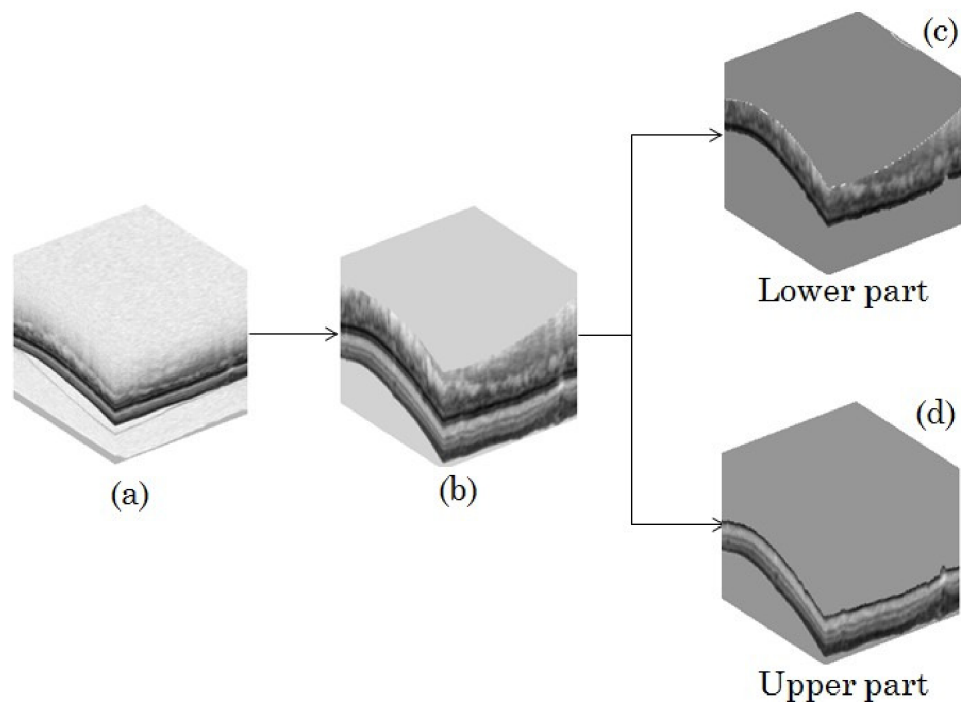


Figure 5.3: a) The de-noised 3D macular image. b) The segmented object image. c) The lower part of the segmented image across the IS boundary. d) The upper part of the segmented image across the IS boundary.

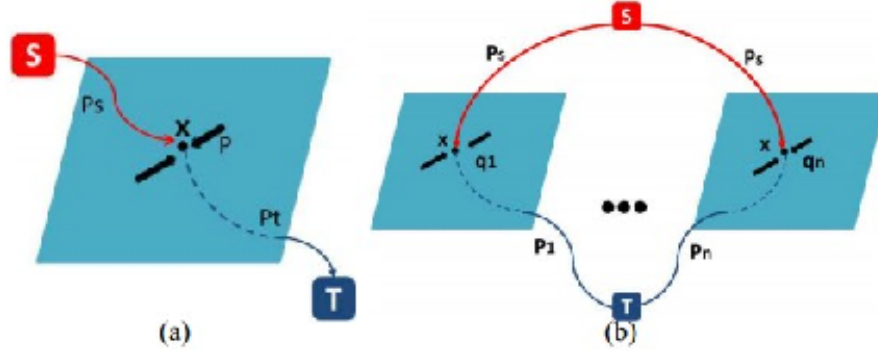


Figure 5.4: a) Graph construction for continuous max-flow and min cut with two labels; b) Graph construction for max-flow and min-cut with n labels.

of foreground (object) and background, while the boundary term is calculated from voxel intensities, textures, colours with smoothing. Here, the multi-region continuous max-flow (Potts model) is used to segment both the upper and lower part to obtain the NFL, GCL-IPL, INL, OPL and ONL-IS boundaries and OS and RPE boundaries, respectively.

Graph construction and Min-cut

Each 3D macular image is represented by a graph $G(\nu, \xi)$ consisting of a set of vertices ν and a set of edges $\xi \subset \nu \times \nu$. The graph contains two terminal vertices: the source s (foreground) and the sink t (background). There are two types of edges: spatial edges and terminal edges. The spatial edges (n -links) link two neighbour vertices except terminal vertices (s or t), and the terminal edges link the terminals s or t to each voxel in the image, respectively. In other words, each voxel $p \in \nu \setminus \{s, t\}$ is connected to terminal s called s -link, and linked to terminal t called t -link. Each edge $e \in \xi$ is assigned a weight $w_e \geq 0$.

A cut is a subset of edges $C \in \xi$, that separates the macular image into two or more disjoint regions. It is through assigning each vertex to the source s or the sink t to cut

the graph into two disjoint regions, called s-t cut. The mathematical expressions are:

$$\nu = \nu_s \cup \nu_t, \quad \nu_s \cap \nu_t = \emptyset \quad (5.7)$$

The optimal cut minimises the sum of edge weights. The corresponding cut-energy is defined as:

$$\min_{C \subset \xi} \sum_{e \in C} w_e \quad (5.8)$$

Let $A = (A_1, \dots, A_p, \dots, A_P)$ be a binary vector, and A_p labels p voxel in the graph to be object ("O") or background ("B"). According to Boykov et al [Boykov and Jolly, 2001], the energy function is defined as:

$$E(A) = \lambda \cdot R(A) + B(A) \quad (5.9)$$

where $R(A)$ is regional term, $B(A)$ is the boundary term. λ is a nonnegative coefficient, which represents the importance of $R(A)$. According to the the voxel intensities of the selected seeds, the intensity distributions are: $Pr(I|O)$ and $Pr(I|B)$. The regional penalty $R_p(\cdot)$ assigns the likelihood of voxel p to object and foreground as:

$$\begin{aligned} R_p(obj) &= -\ln Pr(I_p|O), \\ R_p(bkg) &= -\ln Pr(I_p|B) \end{aligned} \quad (5.10)$$

The regional term can be expressed as:

$$R(A) = \sum_{p \in P} R_p(A_p) = - \sum_{p \in O} \ln Pr(I_p|O) - \sum_{p \in B} \ln Pr(I_p|B) \quad (5.11)$$

The boundary term $B(A)$ is formulated as:

$$B(A) = \sum_{\{p,q\} \in N} B_{\{p,q\}} \cdot \delta(A_p, A_q) \quad (5.12)$$

where $\delta(A_p, A_q) = 1$ if $A_p = A_q$, and otherwise is equal to 0. The boundary penalty $B_{\{p,q\}}$ is defined as:

$$B_{\{p,q\}} \propto \exp\left(-\frac{(I_p - I_q)^2}{2\sigma^2}\right) \cdot \frac{1}{\text{dist}(p, q)} \quad (5.13)$$

The $B_{\{p,q\}}$ is large when the intensities of voxel p and q are similar and the $B_{\{p,q\}}$ is close to 0 when two are different.

Multi-region Potts model

The continuous max-flow convex related Potts model was proposed by Yuan et al [Yuan et al., 2010] to segment the image into n disjoint regions $\{\Omega_i\}_{i=1}^n$. This model modified the boundary term of the original model by calculating the perimeter of each region. The segmentation functional is modified as:

$$E(A) = R(A) + \alpha B(A) = \sum_{i=1}^n \int_{\Omega_i} C_i(x) dx + \alpha \sum_{i=1}^n |\partial\Omega_i| \quad (5.14)$$

$$s.t. \quad \bigcup_{i=1}^n \Omega_i = \Omega; \quad \Omega_p \cap \Omega_q = \emptyset \quad p \neq q \quad (5.15)$$

where $|\partial\Omega_i|$ is the length of the perimeter of each disjoint region Ω_i , $i=1 \dots n$, and α is a positive weight to give the trade-off between the two terms; the function $C_i(x)$ is the cost of region Ω_i with $C_i(x) = |I(x) - l_i|$, where $l_1 \dots l_n$ are the given constants. By using the piecewise constant Mumford-Shah function, $E(A)$ can be rewritten as:

$$E(A) = \sum_{i=1}^n \int_{\Omega} u_i(x) C_i(x) dx + \alpha \sum_{i=1}^n \int_{\Omega} |\nabla u_i| dx \quad (5.16)$$

$$s.t. \quad \sum_{i=1}^n u_i(x) = 1, \quad \forall x \in \Omega \quad (5.17)$$

where $u_i(x)$, $i=1 \dots n$, indicates the region to which the voxel x belongs,

$$u_i(x) = \begin{cases} 1, & x \in \Omega_i \\ 0, & x \notin \Omega_i \end{cases}, i = 1 \dots n \quad (5.18)$$

The convex relaxation is introduced to solve the Potts model based image segmentation as:

$$\min_{u \in S} E(A) \quad (5.19)$$

where S is the convex constrained set of

$$\{u(x) = (u_1(x), \dots, u_n(x)) \in \Delta_+, \forall x \in \Omega\}, \quad (5.20)$$

and Δ_+ is simplex set, for example:

$$\text{for } \forall x \in \Omega, \quad \sum_{i=1}^n u_i(x) = 1; \quad u_i(x) \in [0, 1], \quad i = 1 \cdots n. \quad (5.21)$$

This multi-terminal 'cut' problem as above functional is solved by using a continuous multiple labels max-flow algorithms [Yuan et al., 2010].

5.3 Experiments

The images used in this study were obtained with the Heidelberg SD-OCT Spectralis HRA imaging system (Heidelberg Engineering, Heidelberg, Germany) in Tongren Hospital. Non-invasive OCT imaging was performed on 13 subjects, with ages ranging from 20 to 85 years. This imaging modality has been widely used in clinics and hospitals to diagnose retinal diseases. This imaging system provides 3D image with 256 B-scans, 512 A-scans, 992 pixels in depth and 16 bits per pixel. It is time-consuming to do the manual grading for all the B-scans of the 13 subjects. Therefore, the ground truth was specified by human experts by manually labelling a number of positions on a fixed grid and the rest pixels were interpolated.

5.3.1 Results

To provide a quantitative evaluation of our method, four performance measurements are selected by comparisons with the ground truth, (1) Signed mean error (μ_{unsign}), (2)

Surface	Signed difference (mean±SD)	Unsigned difference (mean±SD)
1	-0.75±1.67	1.65±2.12
2	0.69±1.73	1.43±2.17
3	0.73±1.34	1.22±1.93
4	-0.67±1.53	1.73±2.01
5	-0.93±1.18	1.81±2.32
6	1.53±1.45	2.23±1.93
7	1.29±1.81	1.23±2.13
8	0.79±1.01	1.12±1.37

Table 5.1: Signed and unsigned mean and SD difference between the ground truth and the proposed segmentation results for the eight surfaces, respectively.

Signed standard deviation (σ_{unsign}), (3) Unsigned mean error (μ_{sign}), and (4) Unsigned standard deviation (σ_{sign}). These metrics are defined as:

$$\begin{aligned}
\mu_{unsign} &= \frac{1}{M * N} \sum_{j=1}^M \sum_{i=1}^N |G_{i,j} - S_{i,j}| \\
\sigma_{unsign} &= \sqrt{\frac{1}{M * N} \sum_{j=1}^M \sum_{i=1}^N (G_{i,j} - S_{i,j} - \mu_{unsign})^2} \\
\mu_{sign} &= \frac{1}{M * N} \sum_{j=1}^M \sum_{i=1}^N (G_{i,j} - S_{i,j}) \\
\sigma_{sign} &= \sqrt{\frac{1}{M * N} \sum_{j=1}^M \sum_{i=1}^N (G_{i,j} - S_{i,j} - \mu_{sign})^2}
\end{aligned} \tag{5.22}$$

where $G_{i,j}$, $S_{i,j}$ are the ground truth and the proposed segmentation result of each surface at the (i, j) pixel; M and N are 25 and 512.

Our method successfully located eight intra-retinal surfaces of all the 13 3D macular images without any segmentation failures. The segmentation results are consistent with visual observations and are confirmed by the experts from the hospital as accurate.

The signed and unsigned mean and standard deviation (SD) difference between the ground truth and the proposed segmentation results of the eight surfaces are given in Table 5.1. In terms of the signed difference, the surface 4 gives the best performance

Layers	Average thickness	Absolute thickness difference (mean \pm SD)	Relative thickness difference (mean \pm SD)
NFL	15.99	1.75 \pm 1.77	-1.05 \pm 2.12
GCL+IPL	25.88	2.11 \pm 1.83	1.17 \pm 1.83
INL	14.59	1.79 \pm 1.93	-0.97 \pm 1.72
OPL	8.48	1.73 \pm 2.13	0.67 \pm 1.54
ONL+IS	26.19	1.83 \pm 2.21	1.19 \pm 1.75
OS	10.72	1.95 \pm 2.68	1.37 \pm 1.86
RPE	17.24	1.69 \pm 1.73	-1.09 \pm 2.11
Overall	119.07	1.98 \pm 1.69	-0.93 \pm 1.79

Table 5.2: Average thickness of the 7 layers and overall of all the 30 volume images, absolute thickness and relative thickness difference between the ground truth and the proposed segmentation results of the 7 layers and overall from all the data.

(-0.67 \pm 1.53); while in terms of the unsigned difference, the surface 3 performs the best, it achieves around 1.22 \pm 1.93.

Table 5.2 shows the average thickness and overall thickness of the seven layers of the 30 volume images, besides that the absolute thickness and relative thickness difference between the ground truth and the proposed segmentations of the seven layers of the 30 images are calculated and showed. In terms of the average thickness of the Table 5.2, the overall is around 119.07; the GCL+IPL and ONL+IS layers are 25.88 and 26.19, respectively, as they include two layers, the thinnest layer is OPL (8.48). The absolute thickness difference and relative thickness difference of the overall are 1.98 \pm 1.69 and -0.93 \pm 1.79, respectively.

Figure 5.5 shows an example of eight intra-retinal layers segmented result on an example B-scan. Three examples of 3D segmented results are demonstrated in Figure 5.6. Figure 5.7 illustrates the segmented results of 12 example B-scans from a segmented 3D macular, and Figure 5.7 (a)-(m) are from 30th to 230th B-scans, respectively.

The retinal thickness maps of all the layers are important indicators for diagnosis and understanding of retinal pathologies. Therefore, after an accurate segmentation of the eight retinal boundaries, we generate the thickness maps of seven retinal layers.

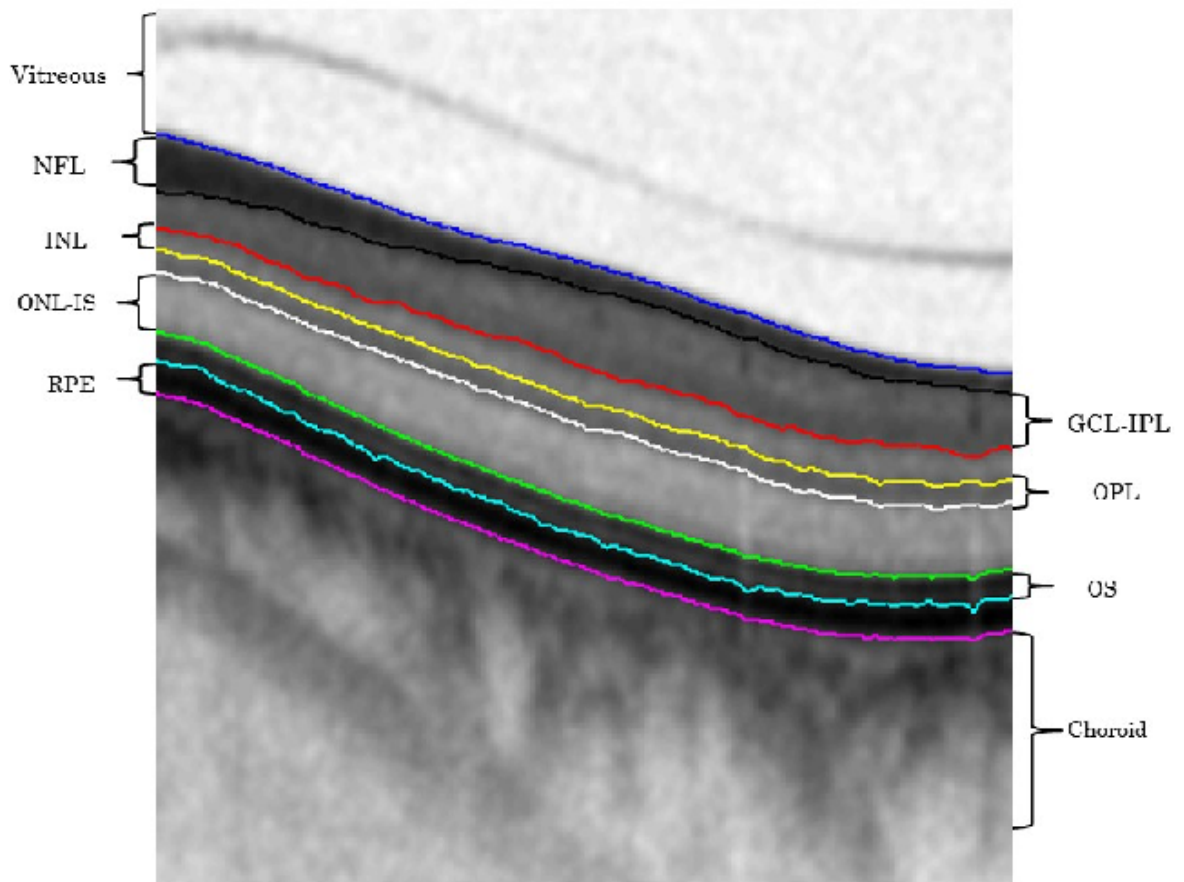


Figure 5.5: Illustration of eight intra-retinal layers segmented result on an example B-scan from top to bottom: 1. Vitreous, 2. NFL, 3. GCL-IPL, 4. INL, 5. OPL, 6.ONL-IS, 7. OS, 8. RPE, 9. Choroid.

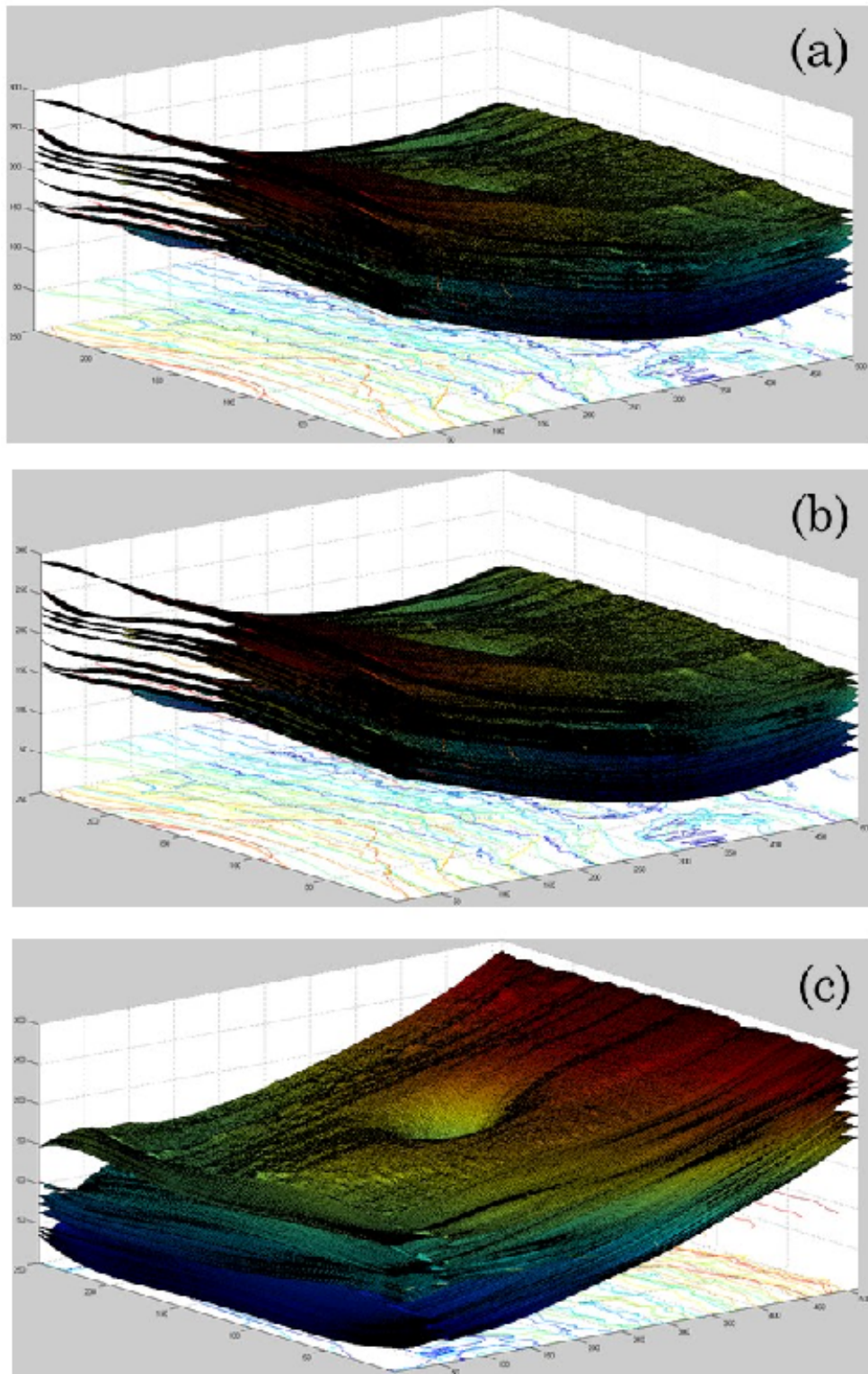


Figure 5.6: Three examples of 3D visualisation of eight surfaces.

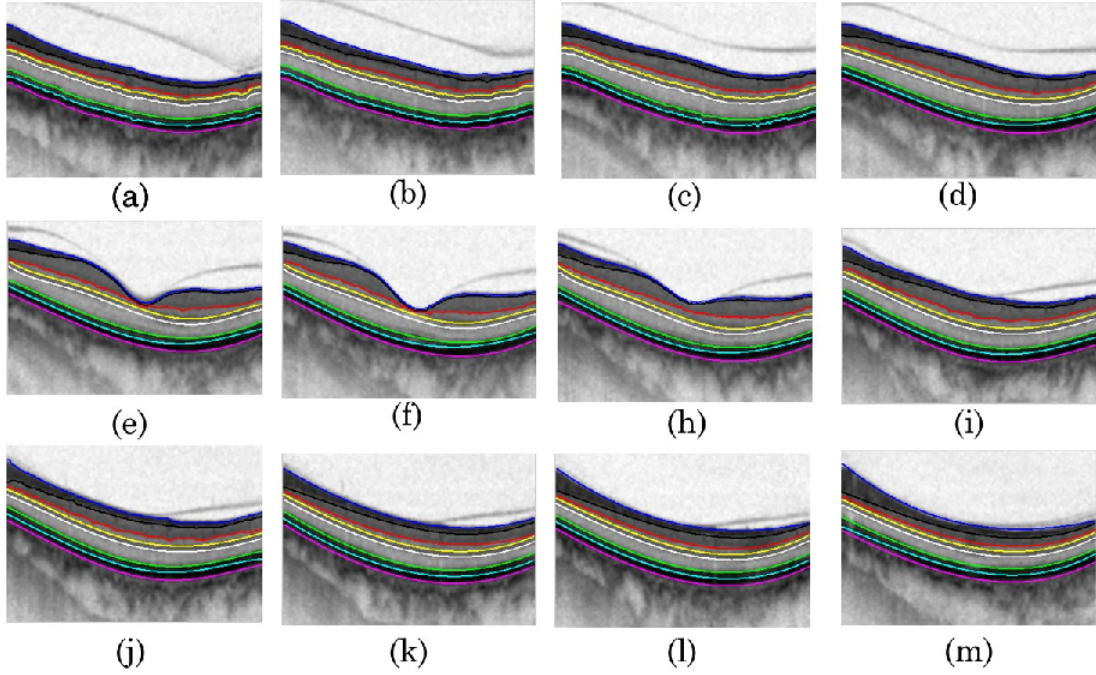


Figure 5.7: Twelve B-scan segmentation results from an example 3D segmented macular, (a)-(m) are 10th, 30th, 50th, 70th, 90th, 110th, 130th, 150th, 170th, 190th, 210th, 230th B-scans, respectively.

Figure 5.8 shows the thickness maps of all the retinal layers, which includes thickness maps of layer 1 to layer 5.8, layers above OS and total retinal layers.

The proposed approach was implemented on MATLAB R2011b on Intel(R) Core(TM) i5-2500 CPU, clock of 3.3GHz, and 8G RAM memory. The computational complexity is $O(n^2)$, n is the image.

5.4 Conclusions

In this chapter, we have presented a novel hybrid intra-retinal layer segmentation method, which includes a hysteresis thresholding method, the CV model based level set method, and the Potts model based multi-region continuous max-flow method. According to the characteristics of different layers, different methods are applied to segment different layers accurately and efficiently. This was implemented with a typical

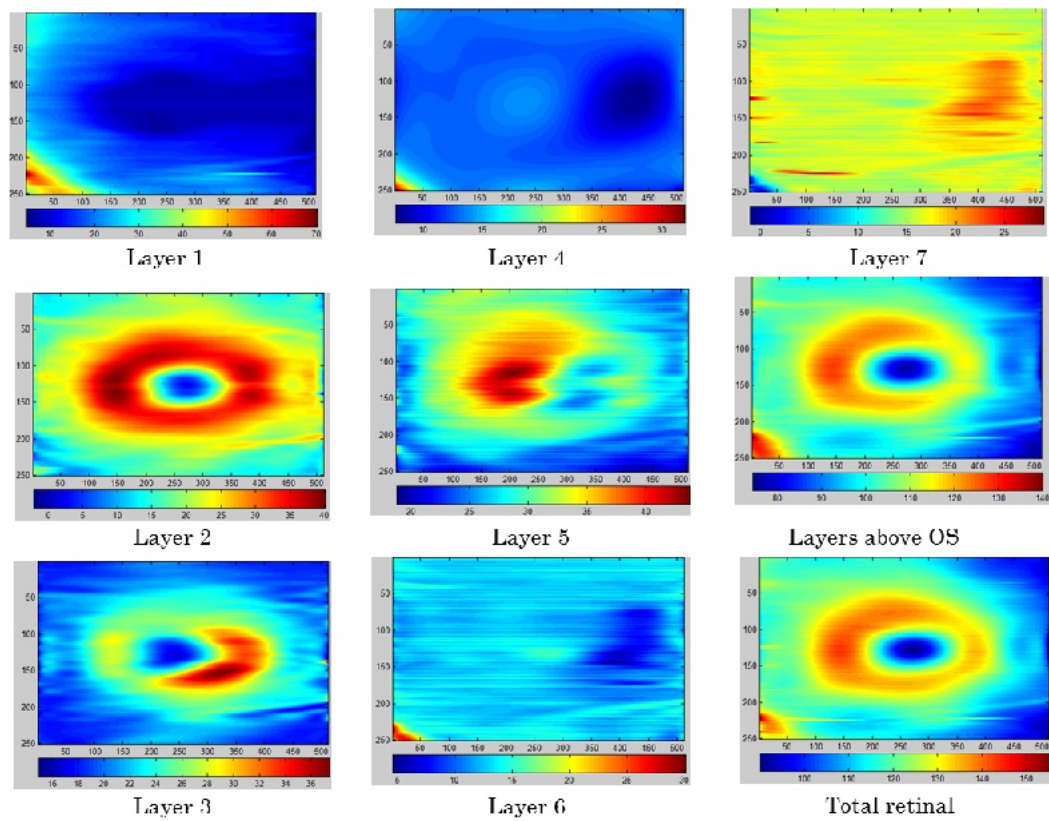


Figure 5.8: Examples of thickness maps of 7 retinal layers, layers exclude choroid layer and total layers. The seven layers are 1. NFL, 2. GCL-IPL, 3. INL, 4.OPL, 5.ONL-IS, 6. OS, 7. RPE

two-staged process: de-noising step and segmentation step. The nonlinear anisotropic diffusion approach and ellipsoidal averaging filter are used to filter the speckle noise and enhance the contrast between the layers as a preprocessing. The segmentation results show that our approach can detect seven layers accurately for 3D macular images with no failure.

The overall segmentation process may look over complicated as it involves three different methods at different stages, namely the level set method, the hysteresis thresholding method and the multi-region continuous max-flow method. It may seem much more concise if a single method is used to simultaneously segment all layers. However, our experiments show that such an approach would demand much higher memory and much longer computation time for the algorithms to run, simply because of the high volume of 3D images. If methods such as sub-sampling are used to reduce the data size and computation time, the accuracy of segmentation would be degraded. In contrast, our approach is able to deliver a better performance with less computation. In particular, the level set method first segments the volume region containing all the 6 middle layers, the simple, fast hysteresis thresholding method partitions this region further into two parts along the easiest boundary between the ONL-LS and OS layers, and finally the multi-region max-flow method is used to segment the individual layers in the upper and lower parts.

The macula is one of the most important areas in the retina. Retinal structures of macula provide important information is important for ophthalmologists to diagnose some eye diseases in early stage. It is necessary and important to extract and analyse these structure information. In this chapter, the hybrid method is proposed and applied to detect seven intra-retinal layers from 3D macular images. However, eye disease such as glaucoma mainly affects the optic nerve head in the early stages, which is considered as another important area of the retina. The intra-retinal layer segmentation from 3D optic nerve head images is the topic of the next chapter.

Chapter 6

Segmentation of Intra-retinal Layers in Optic Nerve Head Images

The intra-retinal layer information of 3D macular images is one of the most important information for ophthalmologists. The method for segmenting layers from 3D macular images was presented in chapter 5. The intra-retinal layer information from 3D optic nerve head images is another important information for eye diseases diagnosis. In this chapter, we propose an automated segmentation method to detect intra-retinal layers in SD-OCT images around the optic nerve head acquired from a high resolution RTVue-100 SD-OCT (Optovue, Fremont, CA, USA). This method starts by removing all the OCT imaging artifacts including the speckle noise and enhancing the contrast between layers using the 3D nonlinear anisotropic diffusion filter. Afterwards, we combine the level set method, k-means and MRF method to segment three intra-retinal layers around the optical nerve head. The segmentation results show that our method can effectively delineate the surfaces of the retinal tissues in the noisy 3D optic nerve head images.

The work included in this chapter was previously published in [Wang et al., 2015c], lead-authored by the author of this thesis, who made substantial contributions to the conception, data collection and processing and writing-up, and sole contributions to the implementation and result analysis.

6.1 Introduction

Several medical image processing techniques are designed and applied to extract useful information from OCT data, such as retinal layers, retinal vessels, retinal lesions, optic nerve head, optic cup and neuro-retinal rim, to help ophthalmologists to perform more accurately and efficiently the diagnosis of eye diseases. In this work, we focus on the intra-retinal layer segmentation of 3D retinal images obtained from around the macular and the optic disc head.

There are two main reasons for intra-retinal layer segmentation [Garvin et al., 2009]: First, the morphology and thickness of each intra-retinal layer are important indicators for assessing the presence of ocular disease. For example, the thickness of the nerve fiber layer can be used to indicator the patient is glaucoma. Second, intra-retinal layer segmentation improves the understanding of the pathophysiology of the systemic diseases. For example, the damage of the nerve fiber layer can provide an indication of brain damage [Garvin et al., 2009].

In this chapter, we propose an automatic approaches to segmenting intra-retinal layers from optic nerve head images. Markov Random Field (MRF) and level set method are used to segment retinal layers for 3D optic nerve head images. Firstly, the nonlinear anisotropic diffusion approach is applied to de-noise the optic nerve head images and enhance the contrast between intra-retinal layers. Then, the level set method is used to segment the retinal layer area. After that, the initial segmentation is obtained by using the k-means method. Because of the inhomogeneity and blood vessel shadows, the k-means method cannot segment all layers well. Therefore, MRF

method is used to improve the initial segmentation through iteration until it converges or reaches the maximum iteration.

This chapter is organised as follows. A detailed description of the proposed method for 3D OCT optic nerve head images is presented in Section 2. The experimental results are shown in Section 3. Finally, conclusions are drawn in Section 4.

6.2 Method

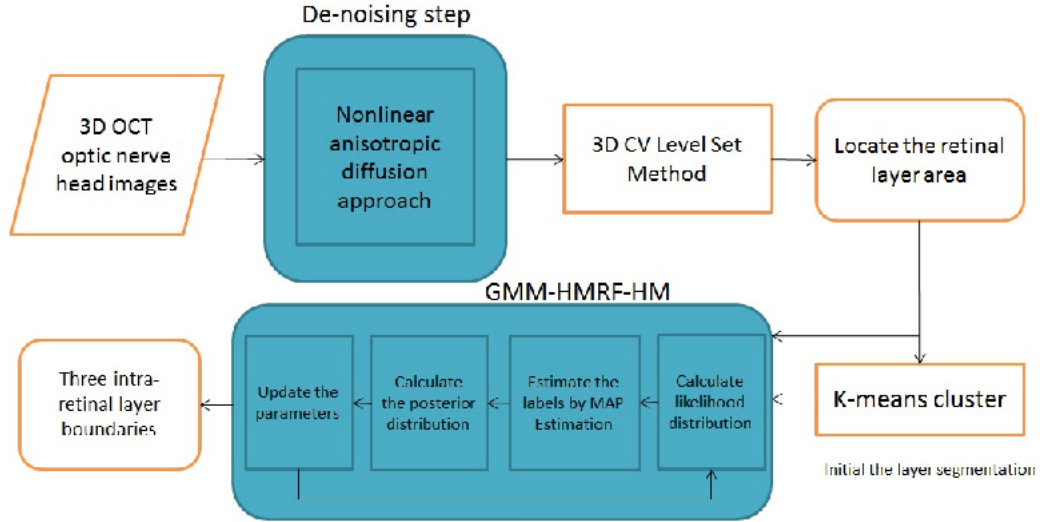


Figure 6.1: Block diagram of retinal layers segmentation process for 3D optic nerve head images.

Figure 6.1 shows the process of layer segmentation for 3D optic nerve head images. The intra-retinal layers for optic nerve head images are segmented by two major steps: preprocessing step and layer segmentation step. During the preprocessing step, the nonlinear anisotropic diffusion approach is applied to 3D optic nerve head images to remove speckle noise and enhance the contrast between retinal layers and background. Intra-retinal layers are segmented by two major steps: preprocessing step and layer segmentation step. At the second step, four intra-retinal layers are segmented by using a combination of methods, which include level set method, K-means cluster and MRF.

The OCT imaging of the retinal is affected by speckle noise. The conventional

anisotropic diffusion approach (Perona-Malik) [Gerig et al., 1992] is used to remove the speckle noise and sharpen the boundaries of the retinal layers during the preprocessing process. The nonlinear anisotropic diffusion filter is defined as Page 86. In this study, the classical region based Chan-Vese model (See Page 35) [Chan and Vese, 2001] is used to locate the boundaries of vitreous and choroid layer from 3D optic nerve head images because it works well when there is large gradient between retinal tissues and background.

6.2.1 RNFL and RPE layers segmentation

After locating the boundaries of the vitreous and choroid layers, we define a region that includes all the layers. In order to reduce the computation load and increase the speed of the segmentation, we cut the retinal area out along the top and bottom layer boundaries. The K-means cluster is used to initialise the reduced image I_s into k classes $S = \{S_1, S_2, \dots, S_k\}$:

$$A = \arg \min_S \sum_{i=1}^k \sum_{I_s(p) \in S_i} \|I_s(p) - \mu_i\|^2 \quad (6.1)$$

where μ_i is the mean intensity in S_i .

However, the k-means cluster fails to accurately locate all the layers due to the blood vessel shadows and intensity inhomogeneities. Therefore, MRF is applied to update the initial input A through iteration until it converges or reaches the maximum iteration. There are four main steps of this method: first we calculate the likelihood distribution according to the initialisation information; then we estimate the labels using MAP method; after that, the posterior distribution is calculated and the parameter set is updated.

The MRF was first introduced to segment brain MR images [Zhang et al., 2001]. Given a 3D image $B = (b_1, \dots, b_i, \dots, b_N)$, where N is the total number of voxels and each b_i is a grey level voxel intensity, and $A = (a_1, \dots, a_i, \dots, a_N)$ ($a_i \in L$) is corresponding initial label of each voxel of the image. For example $L = \{0, 1\}$, the image is segmented into two regions. The RNFL and RPE layers are segmented by using MRF method.

Here, we set $L = \{0, 1, 2, 3\}$.

EM algorithm is used to estimate the parameter set $\Theta = \{\theta_l | l \in L\}$. It is assumed that the voxel intensity b_i follows the Gaussian Mixture Model with C components parameters θ_{a_i} given the label a_i :

$$P(b_i|a_i) = G_{mix}(b_i; \theta_{a_i}) \quad (6.2)$$

Based on the conditional independence assumption of b , the joint probability can be expressed as:

$$P(B|A) = \prod_{i=0}^N P(b_i|a_i) = \prod_{i=0}^N G_{mix}(b_i; \theta_{a_i}) \quad (6.3)$$

Start: The initial GMM with g components parameter set Θ^0 is learned from the labels A and image data B . The parameters can be expressed as:

$$\theta_l = (\mu_{l,1}, \sigma_{l,1}, \omega_{l,1}), \dots, (\mu_{l,C}, \sigma_{l,C}, \omega_{l,C}) \quad (6.4)$$

And the weighted probability of the GMM is:

$$\begin{aligned} G_{mix}(b_i; \theta_{a_i}) &= \sum_{c=1}^C \omega_{a_i,c} G(b_i; \mu_{a_i,c}, \sigma_{a_i,c}) \\ &= \sum_{c=1}^C \frac{\omega_{a_i,c}}{\sqrt{2\pi\sigma_{a_i,c}^2}} \exp\left(-\frac{(b_i - \mu_{a_i,c})^2}{2\sigma_{a_i,c}^2}\right) \end{aligned} \quad (6.5)$$

E-step: At the t^{th} iteration, we can obtain the parameters Θ^t , and the conditional expectation can be deduced as:

$$\begin{aligned} Q(\Theta|\Theta^t) &= E [\ln P(A, B|\Theta) | B, \Theta^t] \\ &= \sum_{A \in L} P(A|B, \Theta^t) \ln P(A, B|\Theta) \end{aligned} \quad (6.6)$$

where L is the set of all possible labels, and $P(A, B|\Theta)$ can be rewritten as:

$$P(A, B|\Theta) = P(A|B)P(B|\Theta) \quad (6.7)$$

M-step: Next let parameter set Θ^{t+1} is estimated through maximising $Q(\Theta|\Theta^t)$:

$$\Theta^{t+1} = \arg \max_{\Theta} Q(\Theta|\Theta^t) \quad (6.8)$$

The next let $\Theta^{t+1} \rightarrow \Theta^t$, and repeat from E-step.

It is assumed that the prior probability can be written as:

$$P(A) = \frac{1}{Z} \exp(-U(A)) \quad (6.9)$$

where $U(A)$ is the prior energy function. We assume that:

$$\begin{aligned} P(B|A, \Theta) &= \prod_i P(b_i|a_i, \theta_{a_i}) = \prod_i G_{mix}(b_i; \theta_{a_i}) \\ &= \frac{1}{Z'} \exp(-U(B|A)) \end{aligned} \quad (6.10)$$

Under these assumptions, the MRF algorithm [Wang, 2012] is given below:

1. Initialise the parameter set Θ^0 .
2. Calculate the likelihood distribution $P^t(b_i|a_i, \theta_{a_i})$.
3. Estimate the labels by MAP estimation using the current parameter Θ^t :

$$\begin{aligned} A^{(t)} &= \arg \max_{A \in L} \{P(B|A, \Theta^{(t)})P(A)\} \\ &= \arg \min_{A \in L} \{U(B|A, \Theta^{(t)}) + U(A)\} \end{aligned} \quad (6.11)$$

Given A and Θ , the likelihood energy (also called unitary potential) is

$$U(B|A, \Theta) = \sum_{i=1}^N U(b_i|a_i, \Theta) = \sum_{i=1}^N \left[\frac{(b_i - \mu_{a_i})^2}{2\sigma_{a_i}^2} + \ln \sigma_{a_i} \right] \quad (6.12)$$

The prior energy function $U(A)$ is defined as:

$$U(A) = \sum_{g \in G} V_g(A) \quad (6.13)$$

where $V_g(A)$ is the clique potential and G is the set of all possible cliques. For 3D image, we assume that each voxel has at most 26-neighbors: the voxel in its 26-neighborhood in 3D.

$$\begin{aligned} G = \{ & (x \pm 1, y, z), (x, y \pm 1, z), (x, y, z \pm 1), \\ & (x \pm 1, y \pm 1, z), (x \pm 1, y, z \pm 1), \\ & (x, y \pm 1, z \pm 1), (x \pm 1, y \pm 1, z \pm 1), \} \end{aligned} \quad (6.14)$$

The clique potential is defined as:

$$V_g(x_i, x_j) = \beta(1 - I_{x_i, x_j}) \quad (6.15)$$

where β is a constant coefficient set to 1/6. The function I_{x_i, x_j} is:

$$I_{x_i, x_j} = \begin{cases} 1, & \text{if } x_i = x_j \\ 0, & \text{if } x_i \neq x_j \end{cases} \quad (6.16)$$

Firstly, the initial estimation A^0 is calculated from the previous loop of the EM algorithm. Then, an iterative algorithm is developed to estimate the A^{k+1} provided A^k until $U(B|A, \Theta) + U(A)$ converges or reaches the maximum k .

4. Calculate the posterior distribution for all $l \in L$ and voxels b_i using Bayesian rule:

$$P^t(l|b_i) = \frac{G_{mix}(b_i; \theta_l)P(l|a_i^t)}{P^t(b_i)} \quad (6.17)$$

where the conditional probability $P(l|a_i^t)$:

$$P(l|a_{N_i}^t) = \frac{1}{Z} \exp\left(-\sum_{j \in N_i} V_g(l, a_j^t)\right) \quad (6.18)$$

where $a_{N_i}^t$ is the neighborhood configuration of a_i^t , and the intensity distribution function is:

$$P^t(b_i) = P(b_i|\theta^t) = \sum_{l \in L} G_{mix}(b_i, \theta_l)P(l|a_{N_i}^t) \quad (6.19)$$

5. Update the parameters by using $P(l|a_{N_i}^t)$

$$\begin{aligned} \mu_l^{(t+1)} &= \frac{\sum_i P^t(b_i)b_i}{\sum_i P^t(b_i)} \\ (\sigma_l^{(t+1)})^2 &= \frac{\sum_i P^t(b_i)(b_i - \mu_l^{(t+1)})^2}{\sum_i P^t(b_i)} \end{aligned} \quad (6.20)$$

6.3 Experiments

We tested the proposed method on SD-OCT optic nerve head images obtained with RTVue-100 SD-OCT (Optovue, Fremont, CA, USA) in Moorfields Eye Hospital. The

Surface	Signed difference (mean±SD)	Unsigned difference (mean±SD)
1	-0.42±0.65	0.83±0.79
2	1.01±1.13	1.43±1.98
3	0.51±1.14	1.02±1.62
4	-0.9±1.53	1.93±2.21

Table 6.1: Signed and unsigned mean and SD difference between the ground truth and the proposed segmentation results for the four surfaces, respectively.

ages of the enrolled subjects ranged from 20 to 85 years. This imaging modalities have been widely used in clinics and hospitals for diagnosing the glaucoma. This imaging system provides a 3D image with 16 bits per pixel and 101 B-scans, 513 A-scans, 768 pixels in depth. Our methods successfully segmented the four intra-retinal surfaces of all the 3D optical nerve head images without any segmentation failures. The signed and unsigned mean and standard deviation (SD) difference between the ground truth and the proposed segmentation results of the four surfaces are given in Table 6.1. In terms of the signed and unsigned differences, the first surface gives the best performance (-0.42 ± 0.65) and (0.83 ± 0.79), respectively.

To provide a quantitative evaluation of our method, four performance measurements are selected by comparing with the ground truth, (1) Signed mean error (μ_{unsign}), (2) Signed standard deviation (σ_{unsign}), (3) Unsigned mean error (μ_{sign}), and (4) Unsigned standard deviation (σ_{sign}). These metrics are defined on Page 94. Our method successfully located four intra-retinal surfaces for 3D optic disc images. The segmentation results are consistent with visual observations and are confirmed by the experts from the hospital as accurate.

Figure 6.2 shows two examples of three intra-retinal layers segmented results from a 3D OCT optic nerve head image which the layer 1 is a retinal nerve fiber layer, layer 2 includes Ganglion Cell Layer, Inner Plexiform Layer, Inner Nuclear Layer and Outer Nuclear Layer (GCL, IPL, INL and ONL), layer 3 is retinal pigment epithelium layer. Figure 6.2 (a) shows the 60th B-scan, which includes the optic disc region. In Figure

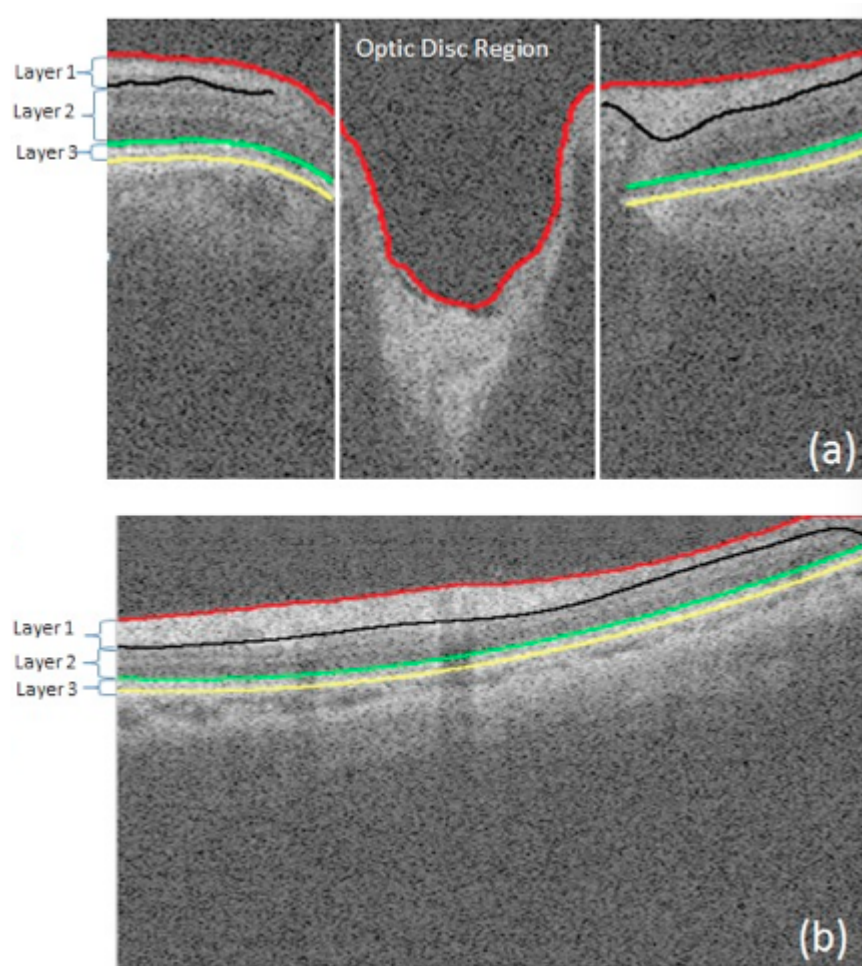


Figure 6.2: Illustration of three intra-retinal layers segmented results of two cross-sectional B-scans from a 3D OCT optic nerve head image. (a) the 60th B-scan, which includes the optic disc region, (b) the 10th B-scan. Layer 1: retinal nerve fiber layer (RNFL), Layer 2 includes Ganglion Cell Layer, Inner Plexiform Layer, Inner Nuclear Layer and Outer Nuclear Layer (GCL, IPL, INL and ONL), Layer 3: retinal pigment epithelium layer (RPE).

6.3, four segmented layer surfaces are illustrated in 3D, and the shape of the surfaces are hypothesised to be related with eye diseases. Three examples of 3D OCT optic nerve head image layer segmented results are demonstrated in Figure 6.4. Figure 6.4 illustrates the segmented results of 10 example B-scans from a segmented 3D optic nerve head image. These segmented segmentation results show that our method can efficiently and accurately detect each layer of the retina in the 3D retinal images around

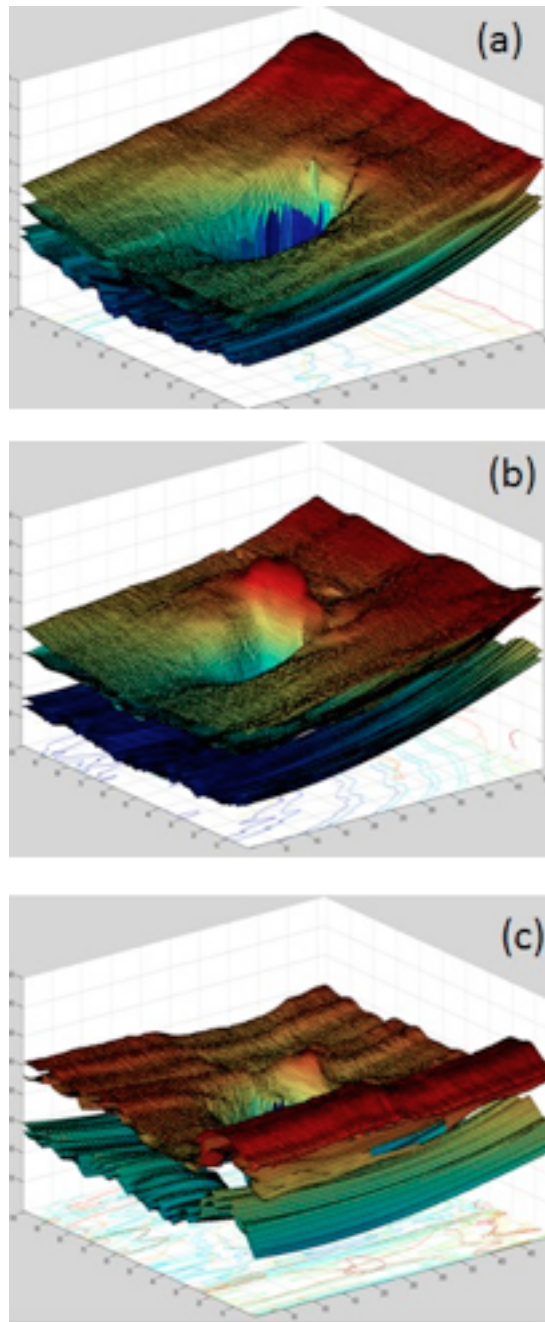


Figure 6.3: Three examples of 3D OCT optic nerve head image layers segmentation results. Four segmented layer surfaces of 3 different 3D images are visualised in 3D. The shape of the surfaces are hypothesised to be related with eye diseases.

the optic nerve head.

The RNFL thickness map is useful in discriminating glaucomatous eyes from normal

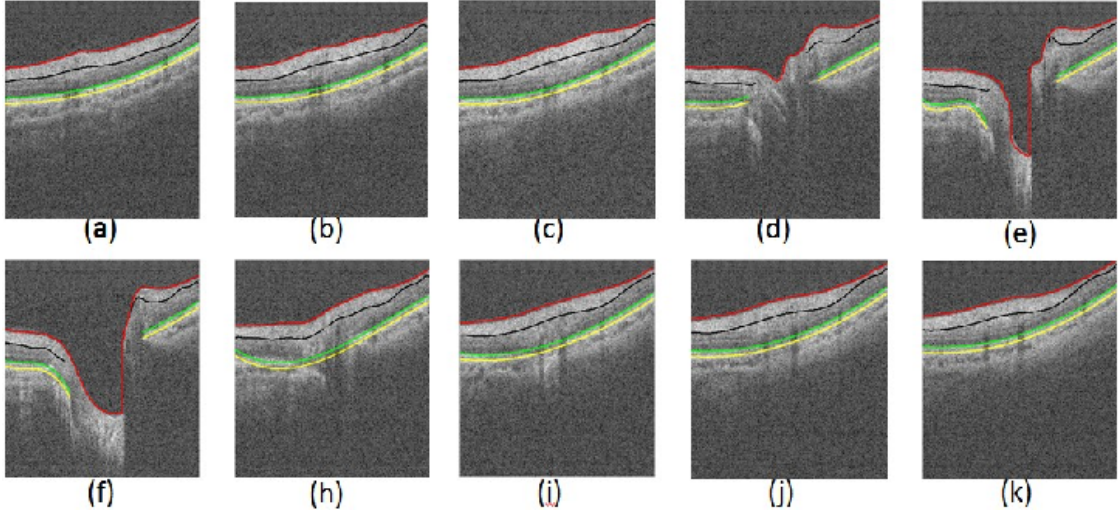


Figure 6.4: Ten B-scan segmentation results from an example 3D segmented optic nerve head image, (a)-(k) are 10th, 20th, 30th, 40th, 50th, 60th, 70th, 80th, 90th, 100th B-scans, respectively. According to the segmentation results on B-scans from the 3D retinal images around the optic nerve head, the efficiency and accuracy of our method are shown.

eyes. Therefore, the RNFL layer thickness map is generated after the segmentation of different retinal layers. With the thickness map of RNFL, we can distinguish the glaucomatous patient from normal subjects. Figure 6.5 shows two examples of the thickness map of RNFL of a healthy subject and a glaucomatous patient. In Figure 6.5 (a), we can observe a thick retinal nerve fiber layer, while Figure 6.5 (b) displays a thin retinal nerve fiber layer.

The proposed approaches are implemented on MATLAB R2011b. The average computation time of our algorithm is 208.45 seconds for a 3D optic never head image on Intel(R) Core(TM) i5-2500 CPU, clock of 3.3GHz. The computational complexity is $O(n^2)$, n is the image.

6.4 Conclusions

In this Chapter, an automated hybrid retinal layer segmentation method is presented for 3D optic nerve head images. This method was implemented with a typical two-staged

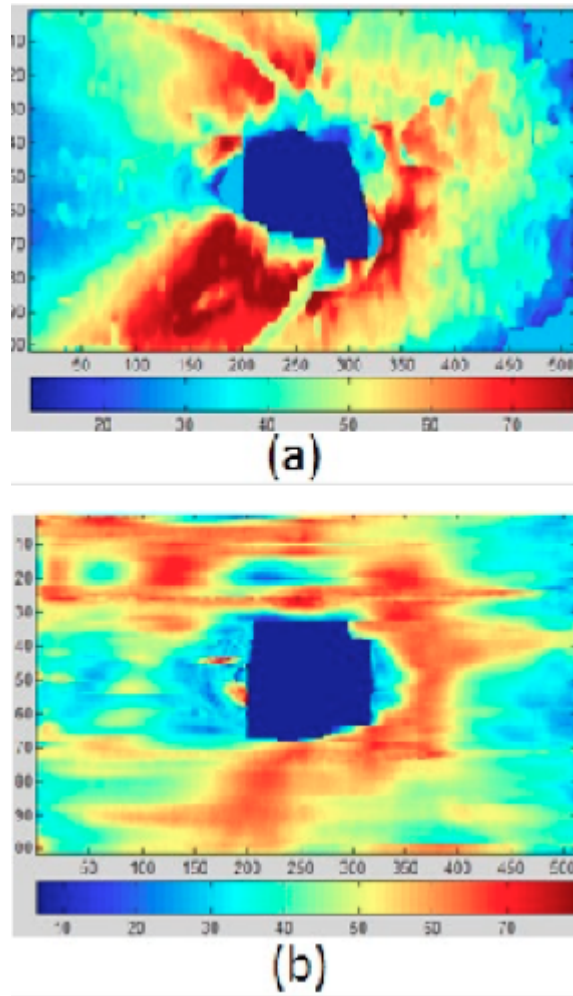


Figure 6.5: The thickness maps of retinal nerve fiber layer (RNFL) from two 3D optic nerve head image examples. The RNFL thickness map is useful in discriminating for glaucomatous eyes from normal eyes. (a) a healthy subject (b) a glaucomatous patient.

process: de-noising step and segmentation step. The nonlinear anisotropic diffusion approach is used to filter the speckle noise and enhance the contrast between the layers as a preprocessing step.

A novel hybrid intra-retinal layer segmentation method for 3D optic nerve head images has been presented. This method combines the CV model based level set, k-means cluster and the Gaussian Mixture Model based Markov Random Field. The segmentation results show that our approach can detect four surfaces accurately for 3D optic nerve head images.

It seems that the segmentation process is too complicated to involve three different methods, namely the level set method, k-means cluster and MRF. However, it is difficult or even impossible to segment all the layers simultaneously by using a single method because it requires larger computation memory and longer computation time for a high volume of 3D images. Although methods such as sub-sampling are applied to reduce the volume size, some important information may lose. Conversely, a better segmentation with less computation is obtained by using our method. More specifically, the CV model based level set method first segments the volume of retinal area, the k-means cluster method initialises the volume data into k regions, and the MRF method updates the initialisation to overcome the artifacts such the the blood vessel shadow and variation of the image intensity.

Two intra-retinal layer segmentation methods for 3D macular images and 3D optic nerve head images are presented respectively in chapters 5 and 6. The choroidal layer is a vascular layer located in the far rear between the retina and sclera, and provides the oxygen and nourishment to the retina. Because the location and medical function of this layer in the retina, the retinal structures of this layer will be easily affected if there is any disorder in the retina. Therefore, it is important to design an automation method for segmenting the choroidal layer for 3D macular images, which is the topic of the next chapter.

Chapter 7

Automatic Choroidal Layer Segmentation Using Level Set Method

We detected the intra-retinal layers from 3D macular images and 3D optic nerve head images by the proposed methods in chapters 5 and 6. The choroid is another important retinal layer that supplies oxygen and nourishment to the retina. The changes in thickness of the choroid have been hypothesised to relate to a number of retinal diseases in pathophysiology. Therefore, an automatic method is proposed for segmenting the choroidal layer from macular images by using the level set method. The distance regularisation and edge constraint terms are embedded into the level set method to avoid the irregular and small regions and keep information about the boundary between the choroid and sclera. Besides, the Markov Random Field method models the region term by correlating the single pixel likelihood function with neighbourhood information to compensate for the inhomogeneous texture and avoid the leakage due to the shadows of blood vessels cast during imaging process. Before that, the 3D nonlinear anisotropic diffusion filter is used to remove all the OCT imaging artifacts including

the speckle noise as well as to enhance the contrast. The effectiveness of this method is demonstrated through testing and comparing with manual segmented cross-sectional B-scans. The results show that our method can successfully and accurately estimate the choroidal bottom boundary.

The work included in this chapter has been submitted to publication [Wang et al., 2016]. The manuscript is lead-authored by the author of this thesis, who made substantial contributions to the conception, data collection and processing and writing-up, and sole contributions to the implementation and result analysis.

7.1 Introduction

The choroid is an important vascular layer and lies between the retina and the sclera. It contains connective tissues and blood vessels and provides oxygen and nourishment to the retina. The changes of the choroid are important indicators of many eye diseases, such as polypoidal choroidal vasculopathy, choroidal tumors and age-related macular degeneration (AMD). Therefore, it is important to segment the layers and reconstruct the retinal structure of the choroid and measure the changes of the choroid. Many commercial OCT imaging modalities are updated and used to capture the 3D choroid images, which provide a clearer structure of the choroid. However, due to the ultra-depth location of the choroid and the limitations of recent imaging instruments, the vascular structure and the boundary between the choroid and sclera in the images is not apparent in some locations.

It is time consuming or even impossible to manually delineate all the choroidal structures and layers for a large number of images because of the indistinct structures and boundaries in some areas. Therefore, automatic choroidal layer segmentation and reconstruction have attracted many researchers. Particularly, the changes of the choroidal thickness are directly or indirectly related with glaucoma, high myopia, neovascular and non-neovascular AMD, central serous chorioretinopathy and Vogt-

Koya-nagi-Harada disease. In this study, we mainly focus on layer segmentation and thickness measurement.

Many automatic or semi-automatic methods [Kajić et al., 2012, Hu et al., 2013, Tian et al., 2013, Alonso-Caneiro et al., 2013, Danesh et al., 2014, Esmaeelpour et al., 2014] for segmenting the choroidal boundary have been reported recently. Kajić et al. [Kajić et al., 2012] presented a statistical model based on texture and shape to automatically segment the choroid layer from OCT B-scans. Hu et al. [Hu et al., 2013] performed the choroid segmentation semi-automatically by using the graph search algorithm from 3D OCT volumes. Tian et al. [Tian et al., 2013] reported an automatic segmentation method for 2D enhanced depth imaging (EDI) OCT images. The choroidal-scleral interface is located by using the Dijkstra’s algorithm. This algorithm is used to find the shortest path for the graph, which is constructed by the valley pixels. Alonso-Caneiro et al. [Alonso-Caneiro et al., 2013] developed a dual probability gradient based method to segment the choroid layer automatically from the enhanced OCT B-scans. Danish et al. [Danesh et al., 2014] segmented the choroidal boundary using a multi resolution texture modelled graph cut method for 3D EDI OCT images.

It is difficult to perform reliable segmentation at some positions of the volume, because the boundary is indistinct. It is a challenge for edge based segmentation methods to perform reliable segmentation results at some positions of the volume. In order to keep the boundary smooth, the shape constraint term is embedded into the segmentation method. However, the constraint term of some methods is too strong to obtain good results, especially for irregular choroidal boundary images. Some area-based methods may not achieve a good performance on those low contrasts and indistinct boundary B-scans. Besides, the performance of some supervised methods depends on the variety of training images.

The aforementioned choroidal layer segmentation methods have their own limits and cannot perform equally well on images of varying quality acquired from different imaging modalities under different conditions. Besides, there are many difficulties in

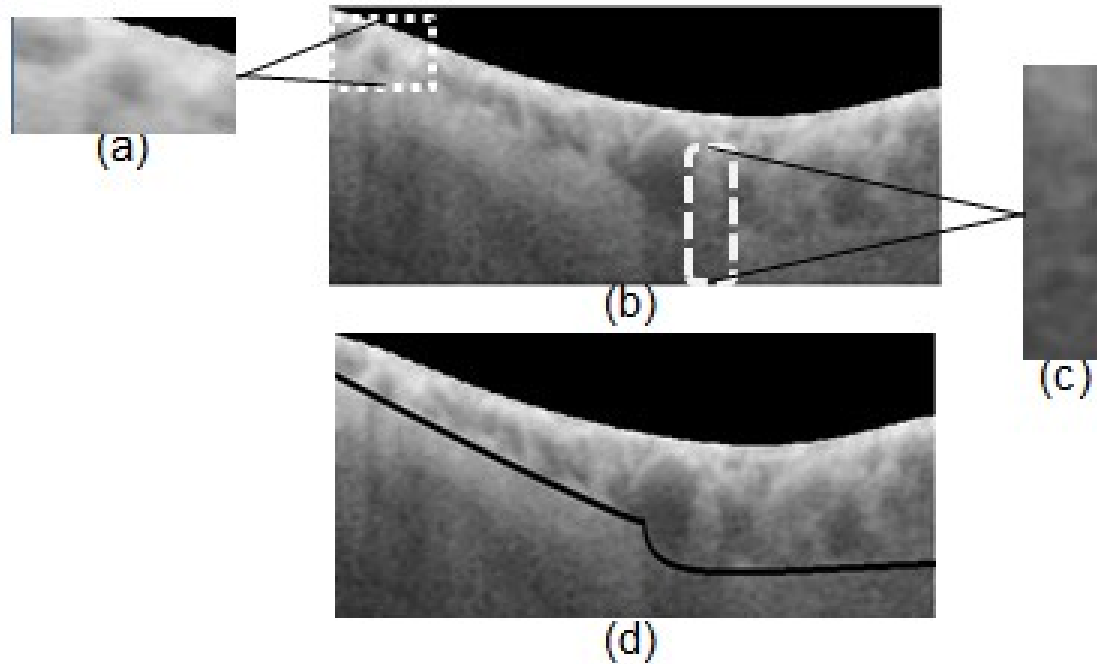


Figure 7.1: The challenge of the choroidal layer segmentation. (a) The original macular B-scan. (b) The inhomogeneous texture from the B-scan. (c) The inseparable histogram distribution of the background and object from the B-scan. (d) The ground truth of the B-scan.

segmenting the choroidal layer from macular images. Figure 7.1 shows examples of the challenges,

- The boundary between the choroid and sclera is not distinct. It is even invisible in some locations as shown in Figure 7.1 (c), thus the edge based segmentation method cannot accurately segment the layers;
- It is difficult to locate the choroid by using an intensity based segmentation method because of the inseparable histogram distribution between the choroid and sclera as Figure 7.1 (a);
- The intensity inhomogeneity and the inconsistent texture (Figure 7.1 (b)) of the choroid make region based and texture based segmentation ineffective because of the presence of the blood vessels in the choroid layer.

In order to overcome these difficulties, we present an automatic choroidal layer segmentation method. The baseline of the method is built on the level set framework, with a region based term, by using the Markov Random Field method to model the choroidal layer and sclera. The edge constraint term is obtained by calculating the the line integral of the edge function and the weighted area of the object region. The distance regularisation term is obtained by computing the contour length of the object region. The advantages of our method are the following:

1. It includes edge information which is still important for segmenting parts of the choroid.
2. We build the correlations between the neighbouring pixels and the pixel likelihood function by using the Markov Random Field method. It compensates for the intensity inhomogeneity of the choroid and avoids small regions caused by shadows cast by blood vessels. Furthermore, the prior information of the background and choroid is calculated and used to obtain the posterior probability to guide the contour to the desired boundary of the choroid.
3. Finally, the distance regularisation term is used to prevent small and irregular contours appearing during the iterations.

The contributions of this chapter are as follows, (1) The Markov Random Field model is embedded into the level set method to segment the background and choroidal layer by using a Gaussian Mixture Model (GMM) and incorporating the neighbouring information; (2) The prior model is constructed by using the GMM, and it is updated through each level set iteration instead of learning from a fixed training set; (3) In order to increase the speed of the level set method, we adapt the narrowband around the zero level set by using the gradient vector flow (GVF).

The remainder of this chapter is organised as follows. In Section 2, the proposed segmentation method is described. The experimental results are presented in Section 3. The last section draws the conclusions.

7.2 Methods

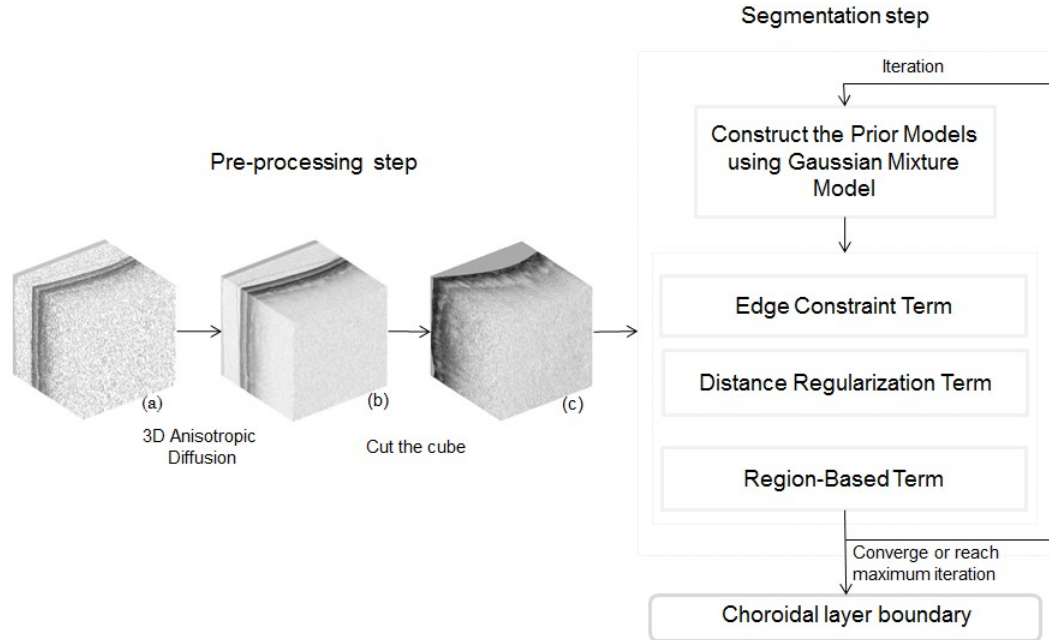


Figure 7.2: Block diagram of automatic choroidal layer segmentation. (a) The original macular OCT image. (b) The de-noised OCT image by using the 3D anisotropic diffusion method. (c) The chopped OCT image.

The choroidal layer is segmented using a typical two-step method, which includes a pre-processing step and a segmentation step. Figure 7.2 shows the overview of the automatic choroidal layer segmentation method. At the first step, the 3D anisotropic diffusion method [Gerig et al., 1992] is used to remove the speckle noise and to enhance the contrast between the background and object. We apply the region based term, edge constraint term and distance regularisation term based level set method to locate the choroidal layer boundary at the second step. Finally, the energy functional is minimised by using partial differential equations (PDE).

7.2.1 Pre-processing step

The OCT imaging process for eyes produces speckle noise and imaging artifacts. Figure 7.2 (a) shows the original 3D macular image, which contains a significant level of

speckle noise and artifacts. The conventional anisotropic diffusion approach (Perona-Malik) [Gerig et al., 1992] is used to remove the speckle noise and sharpen the contrast between the choroidal layer and sclera. The nonlinear anisotropic diffusion filter is defined as Page 86.

The de-noised image is shown in Figure 7.2 (b). However, it is impossible to remove all the imaging artifacts by using the de-noising method. In order to reduce the computational complexity and improve the computation efficiency, we cut this image into a small volume by removing all the background information. The boundary is acquired by using the graph cut method which was proposed in chapter 5, Figure 7.2 (c) shows the chopped OCT volume.

It is obvious that the bottom boundary of the choroidal layer is located below the retinal pigment epithelium boundary. Besides that, we hypothesise the shape of the choroidal lower boundary is similar to the boundary of the retinal pigment epithelium. Therefore, we initialise the potential choroidal layer area from the retinal pigment epithelium boundary to 130 pixels below this boundary. Let Ω be the image domain, the zero level set function $\phi(x, y, z)$ is initialised as:

$$\begin{cases} \phi(x, y, z) = -2, & \text{if } (x, y, z) \in \text{choroidal layer} \\ \phi(x, y, z) = 2, & \text{if } (x, y, z) \in \text{background} \\ \phi(x, y, z) = 0, & \text{if } (x, y, z) \in \partial\Omega \end{cases} \quad (7.1)$$

7.2.2 Level Set Method

Our purpose is to segment the choroidal layer from the reduced OCT image. The energy functional of our segmentation model is formulated as:

$$E(\phi) = E_M(\phi) + E_E(\phi) + E_R(\phi), \quad (7.2)$$

The first term E_M is a region-based term, in which the Markov Random Field method is used to incorporate the neighbouring pixels with the single pixel likelihood function to smooth and tighten the choroidal boundary and to avoid leakages from the boundary.

The second term E_E (see Page 37) incorporates the edge information to direct the initial contour to the boundary. Although the edge between the choroid and sclera is indistinct or even invisible at some locations, the edge information is still important in guiding the contour to the desired boundary. Therefore, we incorporated the edge-based information to assist the segmentation. In order to maintain the boundary of the choroid, the distance regularisation term (E_R) is added to the energy functional. $E_R(\phi)$ (See Page 71) computes the contour length of the zero level set function ϕ to smooth the boundary of the choroidal area.

Before that, the Gaussian Mixture Model based (GMM) prior model (See Page 51) is built according the initial level set function. The GMM parameter set is updated through the segmentation iterations by using the EM algorithm. We update the parameters with each iteration until they converges or a maximum iteration number is reached. This is in contrast with other methods that obtain the parameters from a training process. Unlike other methods, our method can update the parameters according to the characteristics of the input data itself.

Region-Based Term

Markov Random Fields have been used for image segmentation for decades. They were first introduced to segment Brain MR images by Zhang et al. [Zhang et al., 2001]. Chen [Chen, 2010] reported the Bayesian risk term based level set method for medical image segmentation. Yang et al. [Yang et al., 2015] improved Chen's method by incorporating the neighbouring pixel information and presented a MRF embedded level set method for 2D image segmentation by using a single Gaussian Mixture Model (GMM). Because the intensity inhomogeneity and inconsistent texture both of the choroidal area and background, it is difficult to model the complexity of the problem with a single Gaussian mixture model. Therefore, the mixture of Gaussian is integrated into the Markov Random Field method to accurately estimate the choroidal layer. Afterwards, a region-based term is used to correlate the neighbouring pixels with

the single pixel's likelihood function to keep the choroidal layer boundary smooth and tight and to avoid leakages. The region-based energy functional is formulated as:

$$E_M(\phi) = -\nu \int_{\Omega} \log(P(A|B)) dx dy dz \quad (7.3)$$

where $\nu \in \mathcal{R}$ is constant coefficients. This term calculates the average of negative log-likelihood of the posterior segmentation probability.

According to the Bayes theorem, $P(A|B)$ can be formulated as:

$$P(A|B) = \frac{P(B|A)P(A)}{P(B)} \quad (7.4)$$

where $P(B)$ is defined by the image itself and is a constant. Therefore, it can be rewritten as:

$$P(A|B) \propto P(B|A)P(A) \quad (7.5)$$

where $P(B|A)$ is the conditional segmentation probability, and $P(A)$ is the prior probability.

Based on the conditional independence assumption of b , the conditional segmentation probability $P(B|A, \Theta)$ can be expressed as:

$$\begin{aligned} P(B|A, \Theta) &= \prod_{i=0}^N P(b_i|a_i, \theta_{a_i}) = \prod_{i=0}^N G_{mix}(b_i; \theta_{a_i}) \\ &= \frac{1}{Z'} \exp(-U(B|A)) \end{aligned} \quad (7.6)$$

The weighted probability of the GMM is:

$$\begin{aligned} G_{mix}(b_i; \theta_{a_i}) &= \sum_{c=1}^C G_{mix}(b_i; \omega_{a_i,c}, \mu_{a_i,c}, \sigma_{a_i,c}) \\ &= \sum_{c=1}^C \omega_{a_i,c} g(b_i; \mu_{a_i,c}, \sigma_{a_i,c}) \\ &= \sum_{c=1}^C \frac{\omega_{a_i,c}}{\sqrt{2\pi\sigma_{a_i,c}^2}} \exp\left(-\frac{(b_i - \mu_{a_i,c})^2}{2\sigma_{a_i,c}^2}\right) \\ &= \sum_{c=1}^C \omega_{a_i,c} \exp\left(\frac{-\log(2\pi\sigma_{a_i,c}^2)}{2} + \frac{-(b_i - \mu_{a_i,c})^2}{2\sigma_{a_i,c}^2}\right) \end{aligned} \quad (7.7)$$

According to the Jensen's inequality, if $\sum_{c=1}^C \omega_{a_i,c} = 1$, we can generate the following formulation:

$$-\log\left(\sum_{c=1}^C \omega_{a_i,c} g(b_i; \theta_{a_i,c})\right) \leq -\sum_{c=1}^C \omega_{a_i,c} \log(g(b_i; \theta_{a_i,c})) \quad (7.8)$$

According to the formulation, it indicates that minimising the right-hand term will lead to the minimisation of the left term. Therefore, the conditional log-likelihood energy function $U(B|A, \Theta)$ can be defined by:

$$\begin{aligned} U(B|A, \Theta) &= \sum_{i=0}^N \omega_{a_i} U(b_i|a_i, \Theta) \\ &= \sum_{i=0}^N \sum_{c=1}^C \omega_{a_i,c} \left[\frac{(b_i - \mu_{a_i,c})^2}{2\sigma_{a_i,c}^2} + \frac{1}{2} \log(2\pi\sigma_{a_i,c}^2) \right] \end{aligned} \quad (7.9)$$

The prior probability $P(A)$ is defined as:

$$P(A) = P(\phi) = \frac{1}{Z} \exp(-U(\phi)) \quad (7.10)$$

where the prior energy function $U(\phi)$ is defined as:

$$U(\phi) = \sum_{n \in N_{26}} V_n(\phi) \quad (7.11)$$

where $V_n(\phi)$ is the clique potential and N_{26} is the set of all possible cliques (See Page 106).

Finally, the region-based term can be rewritten as:

$$\begin{aligned} E_M(\phi) &= \nu \int_{\Omega} \{U(B|A, \Theta) + U(A)\} dx dy dz \\ &= \nu \left\{ \int_{\Omega} \{U(B|A, \Theta_0) + U(A)\} H(-\phi) dx dy dz + \right. \\ &\quad \left. \int_{\Omega} \{U(B|A, \Theta_1) + U(A)\} H(\phi) dx dy dz \right\} \end{aligned} \quad (7.12)$$

where $H(\phi)$ is the Heaviside function and is defined as:

$$H(\phi) = \begin{cases} 1, & \phi \geq 0, \\ 0, & \phi < 0, \end{cases} \quad (7.13)$$

The main contribution of this part is that we construct the region-based term by using the GMM based MRF method and embedded into the level set method.

7.2.3 Partial Differential Equation based Energy Minimisation

The energy terms defined as a region-based term, an edge based term and a distance regularisation term are substituted into 7.2. Our energy model of $E(\phi)$ can be rewritten as:

$$\begin{aligned}
E(\phi) = & \nu \left\{ \int_{\Omega} \{U(B|A, \Theta_0) + U(A)\} H(-\phi) dx dy dz + \right. \\
& \int_{\Omega} \{U(B|A, \Theta_1) + U(A)\} H(\phi) dx dy dz \left. + \right. \\
& \lambda \int_{\Omega} g \delta(\phi) |\nabla \phi| dx dy dz + \alpha \int_{\Omega} g H(-\phi) dx dy dz + \\
& \left. \lambda_R \int_{\Omega} \delta(\phi) |\nabla \phi| dx dy dz \right.
\end{aligned} \tag{7.14}$$

According to the Euler-Lagrange differential equation [Aubert and Kornprobst, 2006], the energy minimisation problem $\frac{\partial E(\phi)}{\partial \phi}$ can be reformulated as:

$$\frac{\partial \phi}{\partial t} = - \frac{\partial E(\phi)}{\partial \phi} \tag{7.15}$$

and the corresponding gradient flow equation is defined as:

$$\begin{aligned}
\frac{\partial \phi}{\partial t} = & \nu \left\{ - \{U(B|A, \Theta_0) + U(A)\} + \right. \\
& \{U(B|A, \Theta_1) + U(A)\} \delta(\phi) + \\
& \left\{ \lambda (\nabla g |\nabla \phi| + g \operatorname{div} \left(\frac{\nabla \phi}{|\nabla \phi|} \right) + \alpha g) \delta(\phi) + \right. \\
& \left. \left. \lambda_R \operatorname{div} \left(\frac{\nabla \phi}{|\nabla \phi|} \right) \right\}
\end{aligned} \tag{7.16}$$

where $\operatorname{div}(\cdot)$ is the divergence operator, which is used to calculate the curvature of the evolving curve by using the spatial derivatives ϕ up to the second order.

Finally, the level set equation can be reformed as:

$$\begin{aligned}
\phi(t+1) = & \phi(t) + \nabla t \left\{ \nu \left\{ - \{U(B|A, \Theta_0) + U(A)\} + \right. \right. \\
& \{U(B|A, \Theta_1) + U(A)\} \delta(\phi) + \\
& \left\{ \lambda (\nabla g |\nabla \phi| + g \operatorname{div} \left(\frac{\nabla \phi}{|\nabla \phi|} \right) + \alpha g) \delta(\phi) + \right. \\
& \left. \left. \lambda_R \operatorname{div} \left(\frac{\nabla \phi}{|\nabla \phi|} \right) \right\} \right.
\end{aligned} \tag{7.17}$$

where ∇t is the time step, and t is the temporal index.

In order to reduce the computational cost of a level set method, the narrowband around the zero level set is implemented instead of updating ϕ in the full image domain. The gradient vector flow (GVF) method [Xu and Prince, 1998] is used instead of the sparse field method [Jalba et al., 2013] to construct the narrowband around the zero level set. The GVF method preserves a diffusion of the gradient feature information and avoids the leakage of the boundary by estimating more comprehensive narrow band around ϕ with the sparse field method. According to [Xu and Prince, 1998], the vector flow field $\vec{V}(x, y, z) = [u(x, y, z), v(x, y, z), w(x, y, z)]$ is defined to minimise an energy function as follows:

$$\epsilon = \int \mu |\nabla \vec{V}|^2 + |\nabla \bar{f}|^2 |\vec{V} - \nabla \bar{f}|^2 dx dy dz \quad (7.18)$$

where μ is a regularisation parameter, f is the edge map of the Heaviside function H ,

$$f = G_\sigma(x, y, z) * H(\phi(x, y, z)) \quad (7.19)$$

where $G_\sigma(x, y, z)$ is a three-dimensional Gaussian function with standard deviation σ . The first term is smoothing term and the second term is the data term, which is minimised when $V = \nabla f$.

The numerical implementation of this energy function problem is formulated as:

$$\begin{aligned} u^{t+1}(x, y, z) = & \mu \nabla^2 u^t(x, y, z) - [u^t(x, y, z) - f_x(x, y, z)] \\ & [f_x(x, y, z)^2 + f_y(x, y, z)^2 + f_z(x, y, z)^2] \end{aligned} \quad (7.20)$$

$$\begin{aligned} v^{t+1}(x, y, z) = & \mu \nabla^2 v^t(x, y, z) - [v^t(x, y, z) - f_y(x, y, z)] \\ & [f_x(x, y, z)^2 + f_y(x, y, z)^2 + f_z(x, y, z)^2] \end{aligned} \quad (7.21)$$

$$\begin{aligned} w^{t+1}(x, y, z) = & \mu \nabla^2 w^t(x, y, z) - [w^t(x, y, z) - f_z(x, y, z)] \\ & [f_x(x, y, z)^2 + f_y(x, y, z)^2 + f_z(x, y, z)^2] \end{aligned} \quad (7.22)$$

Finally, in order to simulate a wider narrowband, the Dirac delta function $\delta(\phi)$ can be rewritten as:

$$\delta(\phi) = u(x, y, z) + v(x, y, z) + w(x, y, z) \quad (7.23)$$

The novelty of this part is that we try to compute the narrowband around the zero level set by using the GVF, which can efficiently estimate more comprehensive narrowband than the sparse field method and increase the calculation speed.

7.3 Experiments

The macular images were obtained at Tongren Hospital, Beijing, China by using the Heidelberg SD-OCT Spectralis HRA imaging system (Heidelberg Engineering, Heidelberg, Germany). This dataset includes thirteen 3D OCT images. Thirteen subjects participated in this research. The ages of the subjects ranged from 20 to 85 years. This imaging modalities protocol has been widely used to diagnose retinal diseases and provides 3D images with 256 B-scans, 512 A-scans, 992 pixels in depth and 16 bits per pixel. Besides that, 20 B-scans of each volume were randomly selected and manually labelled by experts as the ground truth.

In order to evaluate the performance of our segmentation method, we compare the segmented results with the ground truth using three performance metrics. Two common metrics of error used to evaluate the performance of our segmentation were the signed and unsigned mean difference. Figure 7.3 shows the signed and unsigned mean and standard deviation (sd) between the ground truth and the proposed segmentation results of the bottom choroidal boundary of 13 images in this dataset. In terms of the segmentation error of the bottom choroidal boundary, the mean signed difference is 0.72 ± 1.26 and the mean unsigned difference is around 0.87 ± 1.51 . Furthermore, Figure 7.5 compares the mean signed and unsigned mean and standard deviation (sd) between the ground truth and the segmentation results from different methods of the bottom choroidal boundary in this dataset. Our method achieved the best results, compared to the other methods.

Finally, Dice's coefficient was used to measure the similarity between the segmen-

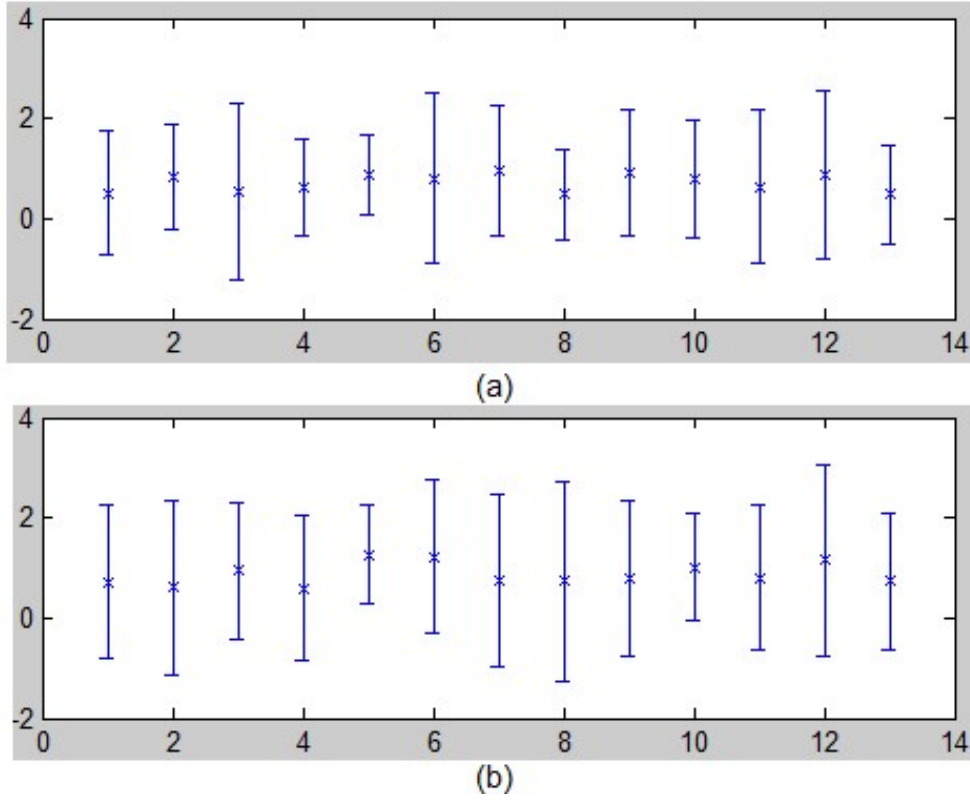


Figure 7.3: The segmentation error of the bottom choroidal layer boundary of the dataset. (a) The signed mean and standard deviation(sd) difference between the ground truth and the proposed segmentation results for the bottom choroidal boundary (b) The unsigned mean and sd difference between the ground truth and the proposed segmentation results for the bottom choroidal boundary.

tation results and the ground truth. The coefficient is defined as:

$$s = \frac{2|A \cap B|}{|A| + |B|} \quad (7.24)$$

where A and B are the segmented choroidal region and the manual labelled choroidal region, respectively. The Dice's coefficient of the dataset was calculated and plotted in Figure 7.4. The mean Dice's coefficient of 13 images in the dataset is around 92% with the standard deviation around 3%. The best Dice's coefficient value is around 96% in the dataset, while the worst is around 87%. Besides that, the mean Dice's coefficient of the dataset was calculated and compared with different methods including the proposed method in Figure 7.6.

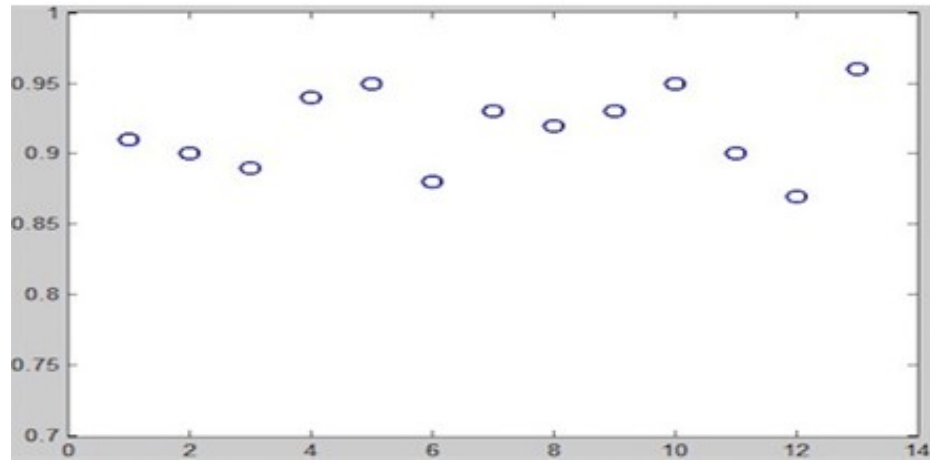


Figure 7.4: The Dice's coefficient of the choroidal layer between the proposed method and the ground truth.

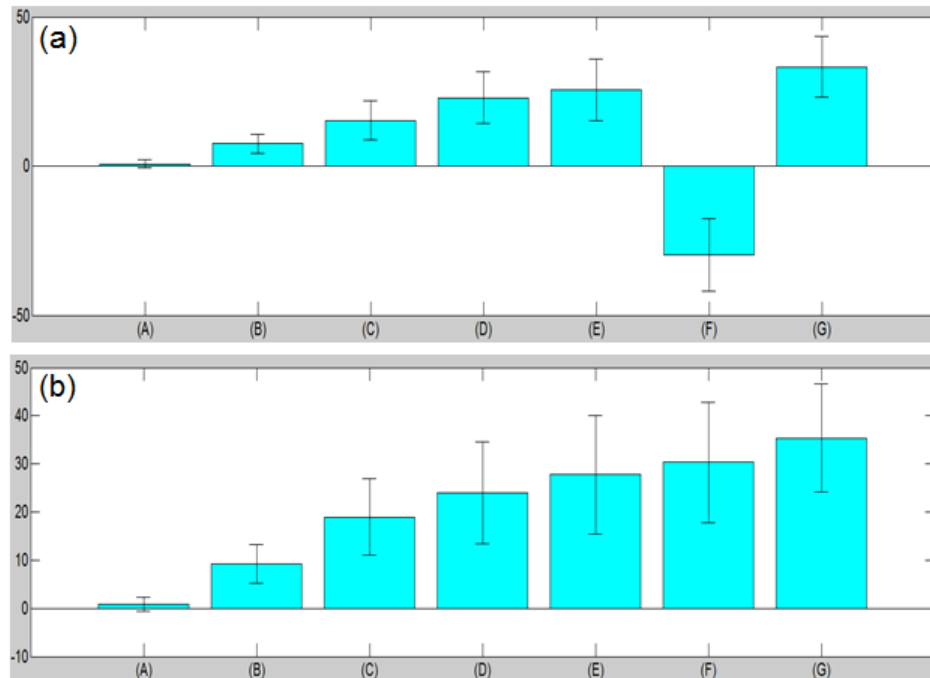


Figure 7.5: The mean segmentation error of the bottom choroidal layer boundary of the different methods, including the proposed method (A), GMM and MRF based Level Set Method (LSM) (B), MRF (C), Graph Cut method (D), Canny Edge detection (E), K-means algorithm (F), and Chan-Vese LSM (G). (a) The mean signed mean and standard deviation (sd) difference between the ground truth and the segmentation results (b) The mean unsigned mean and sd difference between the ground truth and the segmentation results.

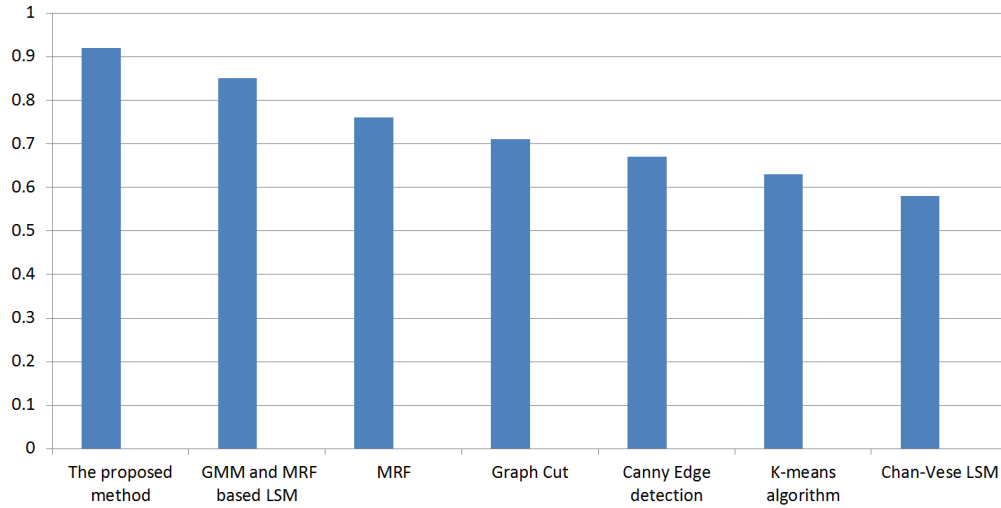


Figure 7.6: The mean Dice's coefficient of the choroidal layer between the methods and the ground truth, including the proposed method, GMM and MRF based LSM, MRF, Graph Cut, Canny Edge detection, K-means algorithms, and Chan-Vese LSM.

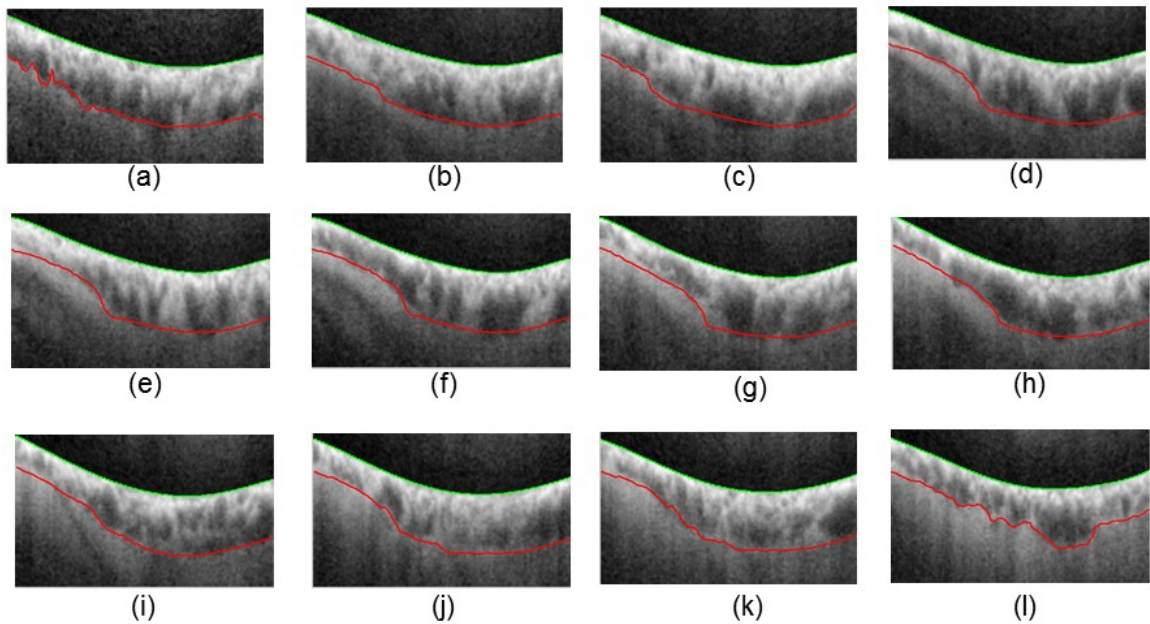


Figure 7.7: A choroid layer segmented example. (a)-(l) are the 10th, 30th, 50th, 70th, 90th, 110th, 130th, 150th, 170th, 190th, 210th, 230th B-scans with the segmented choroidal bottom boundary marked in red, respectively.

It is important to note that a number of parameters are required to be set in the proposed approach. We have used a simple trial-and error method for this. In our

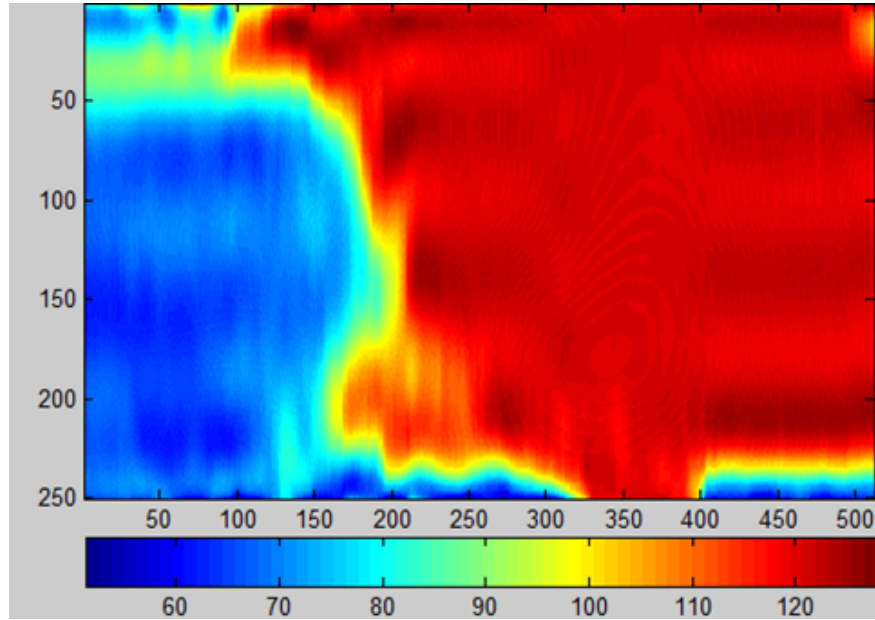


Figure 7.8: Choroidal thickness map of the choroidal layer from this segmented example.

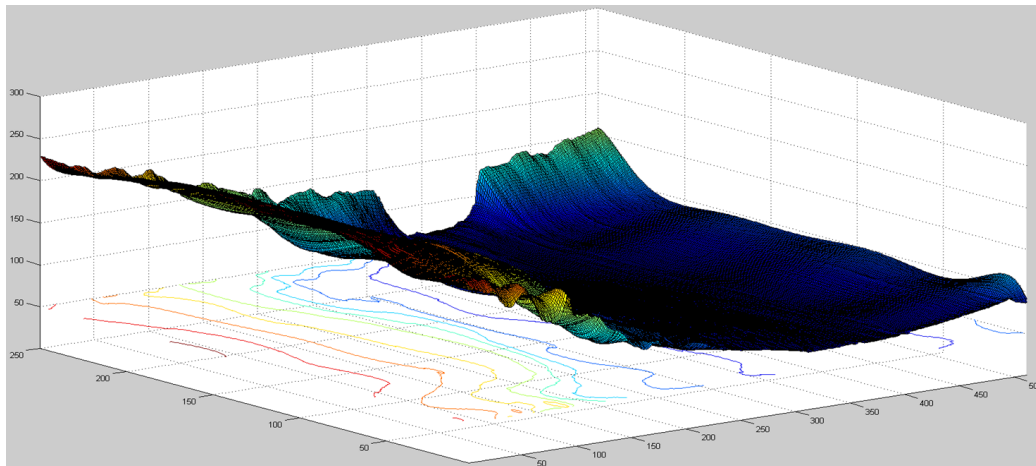


Figure 7.9: 3D view of the segmented choroidal bottom boundary from this example.

experiments, inappropriate parameter settings did affect the segmentation performance and occasionally failed to produce the desired results. However, we believe this is a common issue for all the level set based methods.

According to the experimental results, our segmentation method can estimate and segment the choroidal boundary efficiently on all 13 images with low error. Figure

7.7 (a)-(l) shows 12 B-scans with the segmented choroidal bottom boundary marked in red from a choroidal layer segmented volume. Besides, two ways of visualising the segmented choroidal boundary are shown in Figure 7.8. The thickness map of the choroidal layer is calculated and displayed in Figure 7.8. Figure 7.9 shows the shape of the bottom choroidal boundary in 3D, which is irregular shape compared to the other layers in the retina. The computational complexity is $O(n^2)$, n is the image.

7.4 Conclusions

According to the choroidal characteristics, there are three main challenges in segmenting the choroidal layer: (1) The contrast between the choroid and sclera is weak. (2) The intensity of this layer is inhomogeneous and the texture of this layer is inconsistent because of the blood vessels inside the layer. (3) The histogram distribution between the choroidal layer is inseparable.

In this study, we have presented an automatic choroidal layer segmentation method for 3D OCT volume scans. In the first step, we use the anisotropic diffusion filter to remove the speckle noise and enhance the contrast between the choroid and sclera. Afterward, the zero contour function is initialised according to the prior information from the choroidal layer. Based on the zero contour, the Gaussian Mixture Model (GMM) is used to model both the choroidal area and the background. The region-based term is embedded into the level set energy function by using the Markov Random Field method to build correlations between the neighbouring pixels with the single pixel log-likelihood function. Furthermore, the edge constraint term and distance regularisation term are merged into the level set function to direct the contour to the desired boundary avoiding small and irregular contours.

The choroid layer segmentation method has been evaluated against the manually labelled dataset from Tongren Hospital. The experimental results show that the proposed algorithm has the following advantages: (i) The GMM used to model the sclera

and background is incorporated into the MRF modelled term, which adequately models the intensity inhomogeneity of the choroid. (ii) The neighbouring information is modelled into the region based term to avoid small regions and smooth the boundary. (iii) The edge constraint term is embedded into the energy function to direct the contour to the desired boundary. (iv) The distance regularisation term is modelled into the energy function to avoid small and irregular contours.

The contributions of our method are: (1) The region based term, incorporating the neighbouring pixel information with the single pixel log-likelihood function by using the Markov Random Field, is modelled the level set method; (2) The GMM is constructed according to each level set iteration update; (3) Finally, the GVF method is used to estimate a more comprehensive narrowband around the zero level set to increase the speed of a segmentation.

Chapter 8

Conclusions and Future Work

During the last few decades, retinal imaging technology has developed dramatically. This has enabled ophthalmologists to have a clearer view of the vascular structure and tissues in the retina. Changes of the vascular structure are important indicators of different eye diseases as well as systemic diseases including diabetes, diabetes retinopathy, age-related macular degeneration, and other inherited retinal degenerations. It is time consuming or even impossible to hand label all the retinal structures due to the large amount of data, and the irregular retinal structure shapes. Therefore, a powerful and robust retinal image analysis tool is necessary and important to extract important retinal structures in order to aid in diagnosis and treatment.

Fundus imaging and OCT imaging systems are two of the most widely used imaging modalities in clinics and eye hospitals, so retinal structure analysis tool for 2D fundus and 3D OCT images is increasingly important in aiding ophthalmologists to detect and diagnose eye diseases and prevent further deterioration. Therefore, in this Ph.D. project, some fully automated retinal structure extraction methods are presented for both 2D fundus images and 3D OCT images, which are acquired by using different fundus cameras and OCT imaging systems.

The aim of the thesis is to build a retinal structure analysis tool for retinal images including both 2D and 3D images. The first part of my project is mainly focused on the

fundus image analysis. Two different methods were proposed to segment blood vessels and optic discs from these images. In the second part of the project, intra-retinal layers are detected and segmented from 3D macular and optic nerve head images. Our proposed methods are evaluated on several public fundus datasets including the DRIVE, STARE, and DIARETDB, and 3D OCT images collected from Tongren Hospitals (Beijing, China) and Moorfields Eye Hospital (London, United Kingdom), and compared with alternative methods. The experimental results show that our methods can detect and segment all the retinal structures accurately and efficiently.

8.1 Retinal Structures Extraction from Fundus Images

In the first part of the Ph.D. project, our aim was to detect and segment some obvious retinal structures from fundus images. Two automated methods were designed to extract the blood vessels and optic discs from these images. In chapter 3, the bayesian level set method was applied to segment the blood vessels from these images, and the region enhanced level set method was proposed to segment the optic discs from these images in chapter 4.

The blood vessel segmentation method is a typical three staged process together with the pre-processing and post-processing. At the pre-processing stage, we remove the noise due to the high luminosity and optic disc interference and retain vessels inside the optic disc, which is considered as a challenge in the blood vessel segmentation area. In the post-processing stage, some background pixels misclassified as blood vessel pixels were removed by using the length filter. During the segmentation process, the hybrid region terms including the CV region term and Gaussian Mixture term are embedded into the bayesian level set method with the distance regularisation term to maximise the region information, compensate for the intensity inhomogeneity, and avoid the background noise. The negative log likelihoods of the blood vessels and background probabilities are computed according to the prior GMM parameters as a Gaussian

Mixture region term, and the GMM parameters set was updated through the level set iteration.

The effectiveness of this method is demonstrated through testing and comparing with state-of-the-art methods on two public datasets DRIVE and STARE. The experimental results show that our method offers several advantages over other methods in the following. First, our method performs equally well on different datasets and on both healthy and unhealthy images. Normally, it is difficult to obtain as good segmentation results on these unhealthy images as healthy images. Second, our method is able to segment the blood vessels inside the optic disc and remove the noise of the optic disc boundary, which is generally considered a challenge in vessel segmentation area. Third, our method extracts all the big blood vessels and most of the small branches. Besides, our segmentation method has more than 95% average accuracy on both the DRIVE and STARE datasets.

There are two main parts of the optic disc segmentation method, namely includes the optic disc centre detection and optic disc extraction. In the optic disc centre detection part, the template matching method is applied to approximately locate the centre of the optic disc. Then, the morphologic based method is used to segment the big vessels. Finally, the centroid of the optic disc is re-estimated by using these blood vessel information. In the optic disc extraction part, the level set method, which incorporates the edge constraint term, shape prior term and distance regularisation term, was designed to segment the optic disc. The shape prior term is applied to compensate for intensity inhomogeneities inside the optic disc due to the shadows remaining after the blood vessel removal. The edge information is extracted from the vessel removed image and is modified into the energy function to assist the segmentation. The distance regularisation term is applied to keep the optic disc boundary smooth.

The proposed method was evaluated on three public datasets, the DRIVE, DIARETDB0 and DIARETDB1, with a total of 259 images. None of the three datasets provides the ground truth for the optic discs. In order to evaluate the performance of

our segmentation method, hand labelling ground truths were created for all of the three datasets according to expert guidance. The effectiveness of our method is compared with alternative methods using three public datasets. The experimental results show that our method outperforms state-of-the art methods on these datasets. The overlapping rate between the segmentation results and ground truth is over 88% on these datasets. Our method has several advantages over alternative methods as shown by the experiments. In the first place, our method addresses the obstruction of the vessels inside the optic disc and the intensity inhomogeneity, which are considered as the main factors affecting the segmentation of the optic disc. In the second place, our method performs the segmentation well for both regular and irregular optic disc shapes.

8.2 Retinal Structures Extraction from OCT images

In the second part of the Ph.D. project, our aim is to locate and extract retinal structures from 3D OCT images. Three automated methods were designed to segment the intra-retinal layers from 3D OCT images, which were acquired from different imaging modalities. The layers were imaged around the optic nerve head and macular area. Chapter 5 provides the hybrid method based automatic layer segmentation for 3D OCT macular images. This is followed by a discussion of the intra-retinal layers segmentation from 3D optic nerve head images in chapter 6. In chapter 7, the choroidal layer is located and segmented by using the level set based method from 3D macular images.

In the first part of the OCT image analysis, eight boundaries of retinal layers were detected and segmented from 3D macular images by a hybrid method which includes CV region term based level set method, hysteresis thresholding method, multi-region continuous max-flow based graph cut approaches. The method starts by removing all the OCT imaging artifacts including the speckle noise and by enhancing the contrast between layers using 3D nonlinear anisotropic filters. Due to the stair-casing, a byproduct of the anisotropic method, the ellipsoidal averaging filter is used to remove

the noise. Because the gradient between the retinal tissue and background is large and the basic CV model based level set method works well in this situation, this method is applied to segment the retinal area by locating the boundaries of the vitreous and choroid.

Because of the high contrast between the OS layer and the IS layer, the boundary of IS layer is segmented by using the 3D hysteresis thresholding method, which two threshold values and a loop are used to provide more connected segmentations. After that, the 3D retinal area is split into two parts to reduce the size. It ensures that the computation load will be reduced and the speed of the segmentation will be increased. Finally, a multi-region continuous max-flow (Potts model) based graph cut method is used to segment intra-retinal layers into two parts. Our proposed method was evaluated on 13 3D macular images acquired with Heidelberg SD-OCT Spectralis HRA imaging system (Heidelberg Engineering, Heidelberg, Germany) in Tongren Hospital (Beijing, China). The experimental results show that our method can successfully and accurately segment eight boundaries without any failure.

In the second part of the OCT image research, four boundaries of retinal layers were located and extracted from 3D optic nerve head images by using an automated segmentation method, which combines the 3D nonlinear anisotropic filter, CV based level set method, k-means clustering method and MRF method. This method is a typical two step processing method together with de-noising step and segmentation step. The de-noising process removes all the OCT imaging artifacts including the speckle noise and enhances the contrast between layers by using the 3D nonlinear anisotropic filtering method. According to the characteristics of the image itself, different methods are combined and applied to achieve the segmentation more efficiently and accurately. Because the contrast between the retinal area and background is high, the basic CV model based level set method is applied to locate and segment the retina area by detecting the vitreous and choroidal boundaries.

In order to reduce the computational complexity and increase the segmentation

speed, the volume of the retinal area is obtained by removing all the background. Then, the k-means clustering method is applied to locate the layers approximately as an initialisation for the next step, because the contrast between the different layers is relatively high. However, due to the shadows of the blood vessels, imaging artifacts and intensity inhomogeneities of the image, the k-means method fails to locate all the layers accurately enough. After that, MRF is used to update the initial input by considering the neighbouring information from the k-means through iteration until convergence or the maximum number of iterations is reached. Our 3D optic nerve head images were acquired with RTVue-100 SD-OCT (Optovue, Fremont, CA, USA) from Moorfields Eye Hospital (London, Unite Kingdom). In order to prove the effectiveness and efficiency of our method, we test the proposed method on the data. According to experimental results, our method can accurately segment four layer boundaries over the optic nerve head.

Both the methods we proposed for intra-retinal layer segmentation from 3D macular images and optic nerve head images may look over complicated because they involve different methods at different stages. The first method includes the CV model based Level Set Method, the hysteresis thresholding method and multi-region continuous max-flow graph cut method for the first method, and the second one includes the CV model based level set method, the k-means clustering method and MRF. It may look much more concise if a single method is applied simultaneously to detect all retinal boundaries. According to our experiments, such an approach would demand much higher memory and longer computation time or even fail to segment due to the limit of the computation memory because of the high volume of the data.

In order to segment all the layers simultaneously, many alternative methods reduce the data size by using the sub-sampling method. However, the sub-sampling method may get rid of some important information. Therefore, our approach is able to deliver a better performance with less computational time. More specifically for the first method, the level set method first segments the volume region containing all the 6 middle layers.

The simple and fast hysteresis thresholding method partitions this region further into two parts along the easiest boundary between the ONL-LS and OS layers, and finally the multi-region max-flow method is used to segment the individual layers in the upper and lower parts. While for the second method, the CV model based level set method first segments the volume of retinal area, the k-means cluster method initialises the volume data into k regions, and the MRF method updates the initialisation to overcome artifacts such as the blood vessel shadow and variation of the image intensity.

The choroid is an important layer which supplies oxygen and nourishment to the retina. The changes of the choroidal thickness have been hypothesised to relate to a number of retinal diseases within the pathophysiology. Therefore, in the final part of OCT image analysis, an automatic method based on the level set method was proposed to segment the choroidal layer from 3D macular images, which are acquired from the Heidelberg SD-OCT Spectralis HRA imaging system (Heidelberg Engineering, Heidelberg, Germany) in Tongren Hospital (Beijing, China). This method is a typical two-step method, which includes the pre-processing step and segmentation step. At the pre-processing step, the 3D anisotropic diffusion method is applied to remove the imaging artifacts including the speckle noise and to enhance the contrast between the background and object. In order to reduce the computational complexity and improve the computational efficiency, we cut this original volume down into a small volume along the retinal pigment epithelium boundary, which was segmented by using the method proposed in chapter 7.

There are some challenges in locating and segmenting the choroidal layer: (1) the boundary between the choroid and sclera is not distinct and is even invisible in some locations, (2) the histogram distribution between the choroid and sclera is inseparable, (3) the grey level intensity of the choroid is inhomogeneous and the texture of the choroid is inconsistent, because of the blood vessels in this layer and immaturity of the imaging techniques. Therefore, an automatic choroidal layer segmentation based on the level set method was proposed to overcome these challenges by integrating the

MRF based region based term, edge constraint term and distance regularisation term. The region term is modelled in the level set method by using the MRF method, which correlates the single pixel likelihood function with neighbourhood information to compensate for the inhomogeneous texture and avoid leakage due to the shadows of the blood vessels. The edge constraint term is embedded to keep the edge information between the choroid and sclera, while the distance regularisation is combined to avoid irregular and small regions. The effectiveness of this method is demonstrated by comparison with manual segmented cross-sectional B-scans. The experimental results show that our method can efficiently and accurately locate and segment the choroidal bottom boundary.

The contributions of the method are illustrated in the following: (1) The Gaussian Mixture Model (GMM) used to model the sclera and background is incorporated into the MRF modelled term, which adequately models the intensity inhomogeneity of the choroid. (2) The neighbouring pixel information with the single pixel log-likelihood function are modelled into the level set method by using the Markov Random Field; (3) The GMM parameter set is updated with each level set iteration according to the characteristics of the input data itself; (4) The Gradient Vector Flow method is applied to estimate a more comprehensive narrowband around the zero level set to increase the speed of the segmentation.

8.3 Contributions of the Project

In order to achieve our aims, the main contributions that we have made are summarised in the following:

1. A Bayesian level set method was proposed and implemented to segment the blood vessels from retinal images. This method is based on the region enhanced level set method with the hybrid region terms and the distance regularisation term. The blood vessel information is extracted by using two different region terms including

the Chan-Vese region term and Gaussian Mixture region term from two different inputs. The distance regularisation term is used to remove background noise due to intensity inhomogeneity. According to the input image itself, the Gaussian Mixture region term calculates the negative log likelihood of the blood vessels and background probabilities respectively to achieve better segmentation results.

2. A level set based segmentation method was designed to segment optic discs from retinal images. This method incorporates the edge-based term, distance regularisation term and shape-prior term into the basic level set method to achieve better segmentation results. According to the prior shape information of the optic disc, the shape prior term is incorporated into the level set method to maintain and constrain the shape of the optic disc and compensate the intensity inhomogeneity inside of the optic disc. Furthermore, the edge-based term maintains the edge information of the optic disc, while the distance regularisation term avoids the background noise due to intensity inhomogeneity.
3. A hybrid method including the hysteresis thresholding method, level set method and multi-region continuous max-flow approaches was proposed and implemented to segment eight intra-retinal boundaries from 3D macular images. According to the characteristics of the intra-retinal layers, different methods are applied to detect the specific layers efficiently and accurately. It may sound much more concise if a single method is used to simultaneously segment all layers because the overall segmentation process may look over complicated as this method involving three different methods. However, it demands much higher memory and much longer computation time or is even impossible due to the memory limit of the computer through our experiments because of the high volume of 3D images.
4. The level set method and Markov Random Field method were combined to segment four intra-retinal boundaries from 3D optic nerve head images. The basic 3D CV model based level set method is applied to locate the retinal layer area,

while the MRF method is used to detect the retinal boundaries inside the retinal area by considering the neighbouring information according to the initialisation from the K-means method. According to the characteristics of the data itself, the two methods are sequentially applied to segment the four boundaries more efficiently and accurately. Even though it is more simple to use one single method to segment all the layers simultaneously, due to the memory and computation issues of one single method because of a high volume of 3D data, the combination of methods achieve better segmentation results with less computation time.

5. A segmentation method was proposed to detect the choroidal layer from 3D macular images based on the level set method, which incorporates the edge constraint term, distance regularisation term and Markov Random Field modelled term. Because the boundary between the choroid and sclera is visible at some locations, the edge constraint term is merged into this method to keep the edge information. The markov random modelled term is used to compensate the intensity inhomogeneity of the choroid and avoid small regions due to the blood vessel shadows by building the correlations between the neighbouring pixels and pixel likelihood function. The distance regularisation term is applied to avoid small and irregular contours. This method can predict the choroidal boundary accurately and efficiently.

8.4 Comparison of Proposed Methods

In order to extract important retinal structures from retinal images including 2D fundus images and 3D OCT images to assist ophthalmologists to diagnose eye diseases, three different methods were proposed based on the level set method and two different methods were proposed by using the Chan-Vese model based level set method. The comparison of five different methods is summarised in the following.

The intra retinal layers are segmented by using two different hybrid methods from

3D OCT macular and optic nerve head images respectively in chapter 5 and 6. In order to reduce the computational load and save the computational memory, both methods use the basic Chan-Vese model based level set method to locate the region of interest for further calculation. Some other low-level image processing methods, such as canny edge detection, thresholding method, watershed segmentation and so on, may achieve similar results for some cases. However, the performances of the segmentation results by those low-level image processing methods are not consistent good due to the variational intensity and texture of the dataset. After that, a simple hysteresis thresholding method is used to locate one of the most obvious boundary in the region of interest for the layers segmentation from macular images, while for the layers extraction from optic nerve head images the K-means method is used to initialise the layers in the region of interest. The region of interest of the macular image is divided into two smaller volumes through the boundary which was segmented. Finally, the graph cut method is applied to this two volumes to locate all other boundaries for macular images, while for the optic nerve head images the Markov Random Field method is applied to refine the initialisation through iterations to detect all boundaries. Both proposed methods use the combination of different methods to segment the intra retinal layers accurately and efficiently according to the characteristics of the data itself.

Three different terms are modelled and embedded into the level set method to solve three different image segmentation problems. For the first one in chapter 3, the region enhanced level set method is proposed by using the Gaussian mixture region term and Chan-Vese region term to extract the region information. We apply this method to extract the blood vessel information from 2D fundus images. This method could perform good segmentation results for those 2D and 3D images with slightly low contrast between the object and background and reasonable intensity inhomogeneity. For the second one in chapter 4, the prior shape based level set method is proposed by using the shape constraint term and edge based term to extract the object with strong model of shape. This method is applied to segment the optic disc from 2D fundus

image. Apart from that, this method would perform well for those 2D and 3D images with strong model of object shape. For the final one in chapter 7, the prediction model based level set method is proposed by using the Markov Random Field based term and edge based term to predict and segment the object. Here, this method is applied to locate the choroidal layer from 3D macular images. It can be used to segment those images, in which boundary of the object is indistinct boundary at some of the places and the texture and intensity of the object is inconsistent.

In the first part of the thesis, we focus on 2D fundus image analysis. In terms of the blood vessel segmentation method in chapter 3, the hybrid region term based level set method is used to maximise all the blood vessel information and minimise the background information. Because the blood vessel region in fundus images is relatively distinct from the background region, a Gaussian mixture term is used to model the background and blood vessels according to the image itself. The Chan-Vese region term is used to enhance the region information with the Gaussian mixture term. The method is proposed for segmenting an object that distinguishes from the background with reasonable intensity inhomogeneity. However, the hybrid region based level set method cannot be used to accurately segment the optic disc because the optic disc is not a region based problem. The optic disc has a strong model of shape with high intensity inhomogeneity, a shape constraint term is modelled into the level set method with an edge term and a distance regularisation term to detect the optic disc in chapter 4. The shape constraint term is used to constrain the shape of the segmentation result and overcome the intensity inhomogeneity. The edge term is used to derive the zero level set function close to the boundary of the optic disc. The method is proposed for detecting an object with strong shape model.

In the second part of the thesis, we move on to 3D OCT image analysis. The hybrid methods are proposed to segment the intra-retinal layers from 3D macular images and 3D optic nerve head images in chapters 5 and 6. The graph cut method is applied to segment the layers from 3D macular images, while the MRF method is

applied to segment the layers from 3D optic nerve head images. In order to reduce the computational complexity, the background of the OCT image is removed and the Chan-Vese region based level set method is applied to locate the retina. The boundaries of some layers of the optic nerve head image are disconnected around the optic nerve head, the graph cut method may not perform well on this problem. However, the the Markov Random Field method can segment the boundaries with disconnections in the middle accurately. The intensity distribution of some layers of 3D macular images is relative similar, the Markov random field method may not perform well for this problem. The graph cut can detect the boundaries with low intensity variation.

Finally, the choroidal layer segmentation method is proposed in chapter 7. Because the far rear location of the choroidal layer and the immature imaging system, the boundary of the choroidal layer is indistinct. An estimation method is necessary to estimate the boundary of the choroidal layer. Therefore, the Markov Random Field method is modified into the level set method with an edge based term and a distance regularisation term. The Markov random field term is used to model the choroidal layer and the background according to the image itself to estimate the choroidal boundary. The edge based term is used to retain the edge information of the image itself. This method is proposed to locate an object with unclear edge information at some positions.

8.5 Limitations and Future Work

In the last decade, medical imaging analysis has been dramatically increased in the clinical applications aiding ophthalmologists in accurately diagnosing different kinds of disease. Retinal imaging analysis is one of the hottest topics in medical image analysis. Many different automatic methods were presented to extract and segment retinal structures from 2D and 3D retinal images, which are acquired from different imaging modalities including both fundus cameras and OCT imaging systems. However, the

major limitations of our research are in the following:

1. Because we do not have direct cooperation with clinics or hospitals, we can not obtain the data we need. For example, we need more data with specific eye disease. If we have a large dataset including normal and un-normal data, we can design different methods to understand the specific eye disease better.
2. Due to limited advices from ophthalmologists, we may not know the first hand information about what clinics or hospitals need. According to these requirements, we can design the algorithms to solve the problem in real.
3. Due to the limitation of the hardware of the desktop, we can not improve the calculation speed by using multi-core processing or graphic processing unit programming.

There are many other potential directions of research in the retinal image analysis. Some of the most potential research directions are concluded and discussed in the following.

1. OCT image de-noising: Similar to many other imaging modalities, OCT imaging systems introduce lots of speckle noise during the imaging process. Many de-noising methods have already been presented, such as median filter, wavelet filter, anisotropic diffusion filter and so on. However, these methods may still have some room for improvement. Therefore, some more powerful and efficient de-noising methods are useful and necessary, which can filter out all noise and keep all the tissue structures of the data. Such methods can makes the structure extraction easier and more efficient.
2. Retinal image registration from time series: In order to monitor the progress of eye diseases and to detect even tiny changes through the time series on the image taken around the same area of retina, the registration methods are ur-

gently needed for 2D and 3D images, which are acquired from different imaging modalities.

3. Retinal image registration from different modalities: Retinal images obtained from some imaging systems can provide more obvious retinal structures than other imaging modalities, for example the fundus images show more obvious blood vessel and optic disc information than OCT images. The registration method for retinal images acquired from two different imaging systems is necessary and important to align the mutual information on these images.
4. Blood vessel segmentation and reconstruction from choroidal layer: The choroid is the vascular layer and located between the retina and sclera. The choroidal vessel segmentation makes it available to visualise and measure the choroidal structure and morphological information, which is important for improving the understanding of the pathogenesis of circulation-related ocular diseases.
5. Disease decision making: It is useful and necessary to Investigate the correlation between the choroidal thickness map and choroidal diseases, and to build the relationship between the vascular structures in the choroidal layer and the choroidal diseases.

Bibliography

[eye, 2015] (2015). xii, 9, 10

[mac, 2015] (2015). xiii, 32

[Abdel-Ghafar and Morris, 2007] Abdel-Ghafar, R. and Morris, T. (2007). Progress towards automated detection and characterization of the optic disc in glaucoma and diabetic retinopathy. *Informatics for Health and Social Care*, 32(1):19–25. 65

[Abràmoff et al., 2010] Abràmoff, M. D., Garvin, M. K., and Sonka, M. (2010). Retinal imaging and image analysis. *Biomedical Engineering, IEEE Reviews in*, 3:169–208. 2, 3, 14, 15, 40, 41, 42

[Alberti et al., 1998] Alberti, K., Davidson, M. B., DeFronzo, R. A., Drash, A., Genuth, S., Harris, M. I., Kahn, R., Keen, H., Knowler, W. C., Lebovitz, H., et al. (1998). Report of the expert committee on the diagnosis and classification of diabetes mellitus. *Diabetes Care*, 21:S5. 29

[Alonso-Caneiro et al., 2013] Alonso-Caneiro, D., Read, S. A., and Collins, M. J. (2013). Automatic segmentation of choroidal thickness in optical coherence tomography. *Biomedical optics express*, 4(12):2795–2812. 116

[Alwan et al., 2011] Alwan, A. et al. (2011). *Global status report on noncommunicable diseases 2010*. World Health Organization. 33

- [Aubert and Kornprobst, 2006] Aubert, G. and Kornprobst, P. (2006). *Mathematical problems in image processing: partial differential equations and the calculus of variations*, volume 147. Springer Science & Business Media. 55, 72, 73, 87, 88, 124
- [Azzopardi et al., 2015] Azzopardi, G., Strisciuglio, N., Vento, M., and Petkov, N. (2015). Trainable cosfire filters for vessel delineation with application to retinal images. *Medical image analysis*, 19(1):46–57. 47, 57
- [Berne et al., 2008] Berne, R. M., Koeppen, B. M., and Stanton, B. A. (2008). *Berne and Levy Physiology*. Elsevier Brasil. xii, 12
- [Boykov and Jolly, 2001] Boykov, Y. Y. and Jolly, M.-P. (2001). Interactive graph cuts for optimal boundary & region segmentation of objects in nd images. In *Computer Vision, 2001. ICCV 2001. Proceedings. Eighth IEEE International Conference on*, volume 1, pages 105–112. IEEE. 88, 91
- [Caselles et al., 1993] Caselles, V., Catté, F., Coll, T., and Dibos, F. (1993). A geometric model for active contours in image processing. *Numerische mathematik*, 66(1):1–31. 37
- [Caselles et al., 1997] Caselles, V., Kimmel, R., and Sapiro, G. (1997). Geodesic active contours. *International journal of computer vision*, 22(1):61–79. 38, 39
- [Chalana et al., 1996] Chalana, V., Linker, D. T., Haynor, D. R., and Kim, Y. (1996). A multiple active contour model for cardiac boundary detection on echocardiographic sequences. *Medical Imaging, IEEE Transactions on*, 15(3):290–298. 75
- [Chan and Vese, 2001] Chan, T. F. and Vese, L. A. (2001). Active contours without edges. *Image processing, IEEE transactions on*, 10(2):266–277. 36, 51, 54, 66, 87, 104

- [Chanwimaluang and Fan, 2003] Chanwimaluang, T. and Fan, G. (2003). An efficient blood vessel detection algorithm for retinal images using local entropy thresholding. In *Circuits and Systems, 2003. ISCAS'03. Proceedings of the 2003 International Symposium on*, volume 5, pages V–21. IEEE. 55
- [Chaudhuri et al., 1989] Chaudhuri, S., Chatterjee, S., Katz, N., Nelson, M., and Goldbaum, M. (1989). Detection of blood vessels in retinal images using two-dimensional matched filters. *IEEE Transactions on medical imaging*, 8(3):263–269. 46, 49, 57, 58
- [Chen, 2010] Chen, Y.-T. (2010). A level set method based on the bayesian risk for medical image segmentation. *Pattern Recognition*, 43(11):3699–3711. 121
- [Chiu et al., 2010] Chiu, S. J., Li, X. T., Nicholas, P., Toth, C. A., Izatt, J. A., and Farsiu, S. (2010). Automatic segmentation of seven retinal layers in sdoct images congruent with expert manual segmentation. *Optics express*, 18(18):19413–19428. 84
- [Chrástek et al., 2002] Chrástek, R., Wolf, M., Donath, K., Michelson, G., and Niemann, H. (2002). Optic disc segmentation in retinal images. In *Bildverarbeitung für die Medizin 2002*, pages 263–266. Springer. 65
- [Danesh et al., 2014] Danesh, H., Kafieh, R., Rabbani, H., and Hajizadeh, F. (2014). Segmentation of choroidal boundary in enhanced depth imaging octs using a multiresolution texture based modeling in graph cuts. *Computational and mathematical methods in medicine*, 2014. 116
- [Esmaeelpour et al., 2014] Esmaeelpour, M., Kajic, V., Zabihian, B., Othara, R., Ansari-Shahrezaei, S., Kellner, L., Krebs, I., Nemetz, S., Kraus, M. F., Hornegger, J., et al. (2014). Choroidal haller’s and sattler’s layer thickness measurement using 3-dimensional 1060-nm optical coherence tomography. *PLoS one*, 9(6):e99690. 116

- [Flammer et al., 2013] Flammer, J., Konieczka, K., Bruno, R. M., Virdis, A., Flammer, A. J., and Taddei, S. (2013). The eye and the heart. *European heart journal*, 34(17):1270–1278. 34
- [Friedman et al., 2004] Friedman, D. S., O’colmain, B., Munoz, B., Tomany, S., McCarty, C., De Jong, P., Nemesure, B., Mitchell, P., and Kempen, J. (2004). Prevalence of age-related macular degeneration in the united states. *Arch ophthalmol*, 122(4):564–572. 31, 32, 33
- [Fujimoto et al., 2000] Fujimoto, J. G., Pitris, C., Boppart, S. A., and Brezinski, M. E. (2000). Optical coherence tomography: an emerging technology for biomedical imaging and optical biopsy. *Neoplasia*, 2(1):9–25. 19
- [Fuller et al., 2007] Fuller, A. R., Zawadzki, R. J., Choi, S., Wiley, D. F., Werner, J. S., and Hamann, B. (2007). Segmentation of three-dimensional retinal image data. *Visualization and Computer Graphics, IEEE Transactions on*, 13(6):1719–1726. 83
- [Gao et al., 2015] Gao, J., Liang, Y., Wang, F., Shen, R., Wong, T., Peng, Y., Friedman, D. S., and Wang, N. (2015). Retinal vessels change in primary angle-closure glaucoma: The handan eye study. *Scientific reports*, 5. xiii, 28
- [Garvin et al., 2008] Garvin, M. K., Abramoff, M. D., Kardon, R., Russell, S. R., Wu, X., and Sonka, M. (2008). Intraretinal layer segmentation of macular optical coherence tomography images using optimal 3-d graph search. *Medical Imaging, IEEE Transactions on*, 27(10):1495–1505. 84
- [Garvin et al., 2009] Garvin, M. K., Abramoff, M. D., Wu, X., Russell, S. R., Burns, T. L., and Sonka, M. (2009). Automated 3-d intraretinal layer segmentation of macular spectral-domain optical coherence tomography images. *Medical Imaging, IEEE Transactions on*, 28(9):1436–1447. 82, 102

- [Gerig et al., 1992] Gerig, G., Kubler, O., Kikinis, R., and Jolesz, F. A. (1992). Non-linear anisotropic filtering of mri data. *Medical Imaging, IEEE Transactions on*, 11(2):221–232. 85, 86, 104, 119, 120
- [Gramatikov, 2014] Gramatikov, B. I. (2014). Modern technologies for retinal scanning and imaging: an introduction for the biomedical engineer. *Biomedical engineering online*, 13(1):52. 14, 18
- [Group et al., 2001] Group, A.-R. E. D. S. R. et al. (2001). A randomized, placebo-controlled, clinical trial of high-dose supplementation with vitamins c and e, beta carotene, and zinc for age-related macular degeneration and vision loss: Areds report no. 8. *Archives of ophthalmology*, 119(10):1417. 32
- [Guariguata, 2013] Guariguata, L. (2013). Contribute data to the 6th edition of the idf diabetes atlas. *Diabetes research and clinical practice*, 100(2):280–281. 29
- [Harjutsalo et al., 2013] Harjutsalo, V., Sund, R., Knip, M., and Groop, P.-H. (2013). Incidence of type 1 diabetes in finland. *Jama*, 310(4):427–428. 29
- [Holz and Spaide, 2010] Holz, F. G. and Spaide, R. F. (2010). *Medical retina: Focus on retinal imaging*. Springer Science & Business Media. 33
- [Hoover et al., 2000] Hoover, A., Kouznetsova, V., and Goldbaum, M. (2000). Locating blood vessels in retinal images by piecewise threshold probing of a matched filter response. *IEEE Transactions on Medical Imaging*, 19(3):203–210. 46, 47, 55, 56, 57, 58
- [Hu et al., 2013] Hu, Z., Wu, X., Ouyang, Y., Ouyang, Y., and Sadda, S. R. (2013). Semiautomated segmentation of the choroid in spectral-domain optical coherence tomography volume scans. *Investigative ophthalmology & visual science*, 54(3):1722–1729. 116

- [Huang et al., 1991] Huang, D., Swanson, E. A., Lin, C. P., Schuman, J. S., Stinson, W. G., Chang, W., Hee, M. R., Flotte, T., Gregory, K., Puliafito, C. A., et al. (1991). Optical coherence tomography. *Science*, 254(5035):1178–1181. 18, 21, 82
- [Huang et al., 2012] Huang, G., Qi, X., Chui, T. Y., Zhong, Z., and Burns, S. A. (2012). A clinical planning module for adaptive optics slo imaging. *Optometry and Vision Science*, 89(5):593. 18
- [Jaffe and Caprioli, 2004] Jaffe, G. J. and Caprioli, J. (2004). Optical coherence tomography to detect and manage retinal disease and glaucoma. *American journal of ophthalmology*, 137(1):156–169. 19
- [Jalba et al., 2013] Jalba, A. C., van der Laan, W. J., and Roerdink, J. B. (2013). Fast sparse level sets on graphics hardware. *Visualization and Computer Graphics, IEEE Transactions on*, 19(1):30–44. 125
- [JMJ, 2002] JMJ, R. (2002). Leading causes of blindness worldwide. *Bull Soc Belge Ophtalmol*, 283:19–25. 65
- [Joshi et al., 2011] Joshi, G., Sivaswamy, J., and Krishnadas, S. (2011). Optic disk and cup segmentation from monocular color retinal images for glaucoma assessment. *Medical Imaging, IEEE Transactions on*, 30(6):1192–1205. 66
- [Joshi et al., 2010] Joshi, G. D., Sivaswamy, J., Karan, K., and Krishnadas, S. (2010). Optic disk and cup boundary detection using regional information. In *Biomedical Imaging: From Nano to Macro, 2010 IEEE International Symposium on*, pages 948–951. IEEE. 66
- [Kaba et al., 2013] Kaba, D., Salazar-Gonzalez, A. G., Li, Y., Liu, X., and Serag, A. (2013). Segmentation of retinal blood vessels using gaussian mixture models and expectation maximisation. In *Health Information Science*, pages 105–112. Springer.

- [Kafieh et al., 2013] Kafieh, R., Rabbani, H., Abramoff, M. D., and Sonka, M. (2013). Intra-retinal layer segmentation of 3d optical coherence tomography using coarse grained diffusion map. *Medical image analysis*, 17(8):907–928. 84
- [Kajić et al., 2012] Kajić, V., Esmaeelpour, M., Považay, B., Marshall, D., Rosin, P. L., and Drexler, W. (2012). Automated choroidal segmentation of 1060 nm oct in healthy and pathologic eyes using a statistical model. *Biomedical optics express*, 3(1):86–103. 116
- [Kande et al., 2008] Kande, G. B., Subbaiah, P. V., and Savithri, T. S. (2008). Segmentation of exudates and optic disk in retinal images. In *Computer Vision, Graphics & Image Processing, 2008. ICVGIP'08. Sixth Indian Conference on*, pages 535–542. IEEE. 76, 77, 78
- [Kass et al., 1988] Kass, M., Witkin, A., and Terzopoulos, D. (1988). Snakes: Active contour models. *International journal of computer vision*, 1(4):321–331. 83
- [Kauppi et al., 2007] Kauppi, T., Kalesnykiene, V., Kamarainen, J.-K., Lensu, L., Sorri, I., Raninen, A., Voutilainen, R., Uusitalo, H., Kälviäinen, H., and Pietilä, J. (2007). The diaretdb1 diabetic retinopathy database and evaluation protocol. In *Proceedings of the British Machine Vision Conference 2007, University of Warwick, UK, September 10-13, 2007*. 73
- [Kauppi et al., 2006] Kauppi, T., Kalesnykiene, V., Kamarainen, J.-K., Lensu, L., Sorri, I., Uusitalo, H., Kälviäinen, H., and Pietilä, J. (2006). Diaretdb0: Evaluation database and methodology for diabetic retinopathy algorithms. *Machine Vision and Pattern Recognition Research Group, Lappeenranta University of Technology, Finland*. 73
- [Kichenassamy et al., 1995] Kichenassamy, S., Kumar, A., Olver, P., Tannenbaum, A., and Yezzi, A. (1995). Gradient flows and geometric active contour models. In

- Computer Vision, 1995. Proceedings., Fifth International Conference on*, pages 810–815. IEEE. 38
- [Kraus et al., 2012] Kraus, M. F., Potsaid, B., Mayer, M. A., Bock, R., Baumann, B., Liu, J. J., Hornegger, J., and Fujimoto, J. G. (2012). Motion correction in optical coherence tomography volumes on a per a-scan basis using orthogonal scan patterns. *Biomedical optics express*, 3(6):1182–1199. xii, 19
- [Kwon et al., 2009] Kwon, Y. H., Adix, M., Zimmerman, M. B., Piette, S., Greenlee, E. C., Alward, W. L., and Abramoff, M. D. (2009). Variance owing to observer, repeat imaging, and fundus camera type on cup-to-disc ratio estimates by stereo planimetry. *Journal of glaucoma*, 18(4):305–310. 46
- [Lalonde et al., 2001] Lalonde, M., Beaulieu, M., and Gagnon, L. (2001). Fast and robust optic disc detection using pyramidal decomposition and hausdorff-based template matching. *Medical Imaging, IEEE Transactions on*, 20(11):1193–1200. 65
- [Lang et al., 2013] Lang, A., Carass, A., Hauser, M., Sotirchos, E. S., Calabresi, P. A., Ying, H. S., and Prince, J. L. (2013). Retinal layer segmentation of macular oct images using boundary classification. *Biomedical optics express*, 4(7):1133–1152. 84
- [Lee et al., 2012] Lee, K., Abramoff, M. D., Garvin, M. K., and Sonka, M. (2012). Parallel graph search: application to intraretinal layer segmentation of 3-d macular oct scans. In *SPIE Medical Imaging*, pages 83141H–83141H. International Society for Optics and Photonics. 84
- [Li et al., 2007] Li, C., Kao, C.-Y., Gore, J. C., and Ding, Z. (2007). Implicit active contours driven by local binary fitting energy. In *Computer Vision and Pattern Recognition, 2007. CVPR'07. IEEE Conference on*, pages 1–7. IEEE. 37
- [Li et al., 2008] Li, C., Kao, C.-Y., Gore, J. C., and Ding, Z. (2008). Minimization of region-scalable fitting energy for image segmentation. *Image Processing, IEEE Transactions on*, 17(10):1940–1949. 37

- [Li et al., 2005] Li, C., Xu, C., Gui, C., and Fox, M. D. (2005). Level set evolution without re-initialization: a new variational formulation. In *Computer Vision and Pattern Recognition, 2005. CVPR 2005. IEEE Computer Society Conference on*, volume 1, pages 430–436. IEEE. 72
- [Li et al., 2010] Li, C., Xu, C., Gui, C., and Fox, M. D. (2010). Distance regularized level set evolution and its application to image segmentation. *Image Processing, IEEE Transactions on*, 19(12):3243–3254. 38, 39, 54, 70
- [Li and Chutatape, 2003] Li, H. and Chutatape, O. (2003). Boundary detection of optic disk by a modified asm method. *Pattern Recognition*, 36(9):2093–2104. 66
- [Li and Chutatape, 2004] Li, H. and Chutatape, O. (2004). Automated feature extraction in color retinal images by a model based approach. *Biomedical Engineering, IEEE Transactions on*, 51(2):246–254. 66
- [Li et al., 2015] Li, X., Jiang, D., Shi, Y., and Li, W. (2015). Segmentation of mr image using local and global region based geodesic model. *Biomedical engineering online*, 14(1):8. 39
- [Liew and Wang, 2011] Liew, G. and Wang, J. J. (2011). Retinal vascular signs: a window to the heart? *Revista Española de Cardiología (English Edition)*, 64(6):515–521. 35
- [Lim et al., 2014] Lim, L., Cheung, G., and Lee, S. (2014). Comparison of spectral domain and swept-source optical coherence tomography in pathological myopia. *Eye*, 28(4):488–491. 26
- [Lowell et al., 2004] Lowell, J., Hunter, A., Steel, D., Basu, A., Ryder, R., Fletcher, E., and Kennedy, L. (2004). Optic nerve head segmentation. *Medical Imaging, IEEE Transactions on*, 23(2):256–264. 65, 67

- [Lupascu et al., 2008] Lupascu, C. A., Tegolo, D., and Di Rosa, L. (2008). Automated detection of optic disc location in retinal images. In *Computer-Based Medical Systems, 2008. CBMS'08. 21st IEEE International Symposium on*, pages 17–22. IEEE, 76, 78
- [Marín et al., 2011] Marín, D., Aquino, A., Gegúndez-Arias, M. E., and Bravo, J. M. (2011). A new supervised method for blood vessel segmentation in retinal images by using gray-level and moment invariants-based features. *Medical Imaging, IEEE Transactions on*, 30(1):146–158. 57, 59
- [Martinez-Perez et al., 2007] Martinez-Perez, M. E., Hughes, A. D., Thom, S. A., Bharath, A. A., and Parker, K. H. (2007). Segmentation of blood vessels from red-free and fluorescein retinal images. *Medical image analysis*, 11(1):47–61. 57
- [Melmed et al., 2011] Melmed, S., Polonsky, K. S., Larsen, P. R., and Kronenberg, H. M. (2011). *Williams textbook of endocrinology: Expert consult*. Elsevier Health Sciences. 30, 31
- [Mendonça and Campilho, 2006] Mendonça, A. M. and Campilho, A. (2006). Segmentation of retinal blood vessels by combining the detection of centerlines and morphological reconstruction. *IEEE Trans Med Imaging*, 25(9):1200–13. 46, 47, 56, 57, 58
- [Mokwa et al., 2013] Mokwa, N. F., Ristau, T., Keane, P. A., Kirchof, B., Sadda, S. R., and Liakopoulos, S. (2013). Grading of age-related macular degeneration: comparison between color fundus photography, fluorescein angiography, and spectral domain optical coherence tomography. *Journal of ophthalmology*, 2013. 3
- [Mumford and Shah, 1989] Mumford, D. and Shah, J. (1989). Optimal approximations by piecewise smooth functions and associated variational problems. *Communications on pure and applied mathematics*, 42(5):577–685. 35, 66

- [Murakami and Yoshimura, 2013] Murakami, T. and Yoshimura, N. (2013). Structural changes in individual retinal layers in diabetic macular edema. *Journal of diabetes research*, 2013. 3
- [Nguyen et al., 2013] Nguyen, U. T., Bhuiyan, A., Park, L. A., and Ramamohanarao, K. (2013). An effective retinal blood vessel segmentation method using multi-scale line detection. *Pattern recognition*, 46(3):703–715. 47
- [Nichols et al., 2012] Nichols, M., Townsend, N., Luengo-Fernandez, R., Leal, J., Gray, A., Scarborough, P., and Rayner, M. (2012). European cardiovascular disease statistics 2012. *European Heart Network, Brussels, European Society of Cardiology, Sophia Antipolis*, page P104. 33
- [Niemeijer et al., 2004] Niemeijer, M., Staal, J., van Ginneken, B., Loog, M., and Abramoff, M. D. (2004). Comparative study of retinal vessel segmentation methods on a new publicly available database. In *Medical Imaging 2004*, pages 648–656. International Society for Optics and Photonics. 57
- [Niemeijer et al., 2007] Niemeijer, M., van Ginneken, B., Russell, S. R., Suttorp-Schulten, M. S., and Abramoff, M. D. (2007). Automated detection and differentiation of drusen, exudates, and cotton-wool spots in digital color fundus photographs for diabetic retinopathy diagnosis. *Investigative ophthalmology & visual science*, 48(5):2260–2267. xiii, 30, 31
- [Novo et al., 2009] Novo, J., Penedo, M. G., and Santos, J. (2009). Localisation of the optic disc by means of ga-optimised topological active nets. *Image and Vision Computing*, 27(10):1572–1584. 65
- [of Health, 2000] of Health, D. (2000). National service framework for coronary heart disease. 33, 34
- [Organization, 1988] Organization, W. H. (1988). Coding instructions for the who/pbl eye examination record (version iii). *Geneva: WHO*. 82

- [Osareh et al., 2002] Osareh, A., Mirmehdi, M., Thomas, B., and Markham, R. (2002). Colour morphology and snakes for optic disc localisation. In *The 6th medical image understanding and analysis conference*, pages 21–24. BMVA Press. 65
- [Ouyang et al., 2013] Ouyang, Y., Heussen, F. M., Keane, P. A., Sadda, S. R., and Walsh, A. C. (2013). The retinal disease screening study: prospective comparison of nonmydriatic fundus photography and optical coherence tomography for detection of retinal irregularities. *Investigative ophthalmology & visual science*, 54(2):1460. 2
- [Pallawala et al., 2004] Pallawala, P., Hsu, W., Lee, M. L., and Eong, K.-G. A. (2004). Automated optic disc localization and contour detection using ellipse fitting and wavelet transform. In *Computer Vision-ECCV 2004*, pages 139–151. Springer. 65
- [Park et al., 2006] Park, B., Lawrence, K. C., Windham, W. R., and Smith, D. P. (2006). Performance of hyperspectral imaging system for poultry surface fecal contaminant detection. *Journal of Food Engineering*, 75(3):340–348. 16
- [Pratondo et al., 2016] Pratondo, A., Chui, C.-K., and Ong, S.-H. (2016). Robust edge-stop functions for edge-based active contour models in medical image segmentation. *Signal Processing Letters, IEEE*, 23(2):222–226. 39
- [Quigley and Broman, 2006] Quigley, H. A. and Broman, A. T. (2006). The number of people with glaucoma worldwide in 2010 and 2020. *British Journal of Ophthalmology*, 90(3):262–267. 27, 28, 29
- [Resnikoff et al., 2004] Resnikoff, S., Pascolini, D., Etya’ale, D., Kocur, I., Pararajasegaram, R., Pokharel, G. P., and Mariotti, S. P. (2004). Global data on visual impairment in the year 2002. *Bulletin of the world health organization*, 82(11):844–851. 3

- [Ricci and Perfetti, 2007] Ricci, E. and Perfetti, R. (2007). Retinal blood vessel segmentation using line operators and support vector classification. *Medical Imaging, IEEE Transactions on*, 26(10):1357–1365. 57, 59
- [Roychowdhury et al., 2015] Roychowdhury, S., Koozekanani, D., and Parhi, K. (2015). Iterative vessel segmentation of fundus images. 57, 58, 59, 61
- [Saine and Tyler, 2002] Saine, P. J. and Tyler, M. E. (2002). *Ophthalmic photography: retinal photography, angiography, and electronic imaging*, volume 132. Butterworth-Heinemann Boston. xii, 14, 16
- [Schuman, 2008] Schuman, J. S. (2008). Spectral domain optical coherence tomography for glaucoma (an aos thesis). *Transactions of the American Ophthalmological Society*, 106:426. xiii, 20, 21, 22, 26, 27
- [Sekhar et al., 2008] Sekhar, S., Al-Nuaimy, W., and Nandi, A. K. (2008). Automated localisation of retinal optic disk using hough transform. In *Biomedical Imaging: From Nano to Macro, 2008. ISBI 2008. 5th IEEE International Symposium on*, pages 1577–1580. IEEE. 65
- [Seo et al., 2004] Seo, J., Kim, K., Kim, J., Park, K., and Chung, H. (2004). Measurement of ocular torsion using digital fundus image. In *Engineering in Medicine and Biology Society, 2004. IEMBS'04. 26th Annual International Conference of the IEEE*, volume 1, pages 1711–1713. IEEE. 76, 78
- [Smith et al., 2008] Smith, B., Saad, A., Hamarneh, G., and Moller, T. (2008). Recovery of dynamic pet regions via simultaneous segmentation and deconvolution. *Analysis of Functional Medical Image Data (MICCAI functional)*, pages 33–40. 88
- [Soares et al., 2006] Soares, J. V., Leandro, J. J., Cesar, R. M., Jelinek, H. F., and Cree, M. J. (2006). Retinal vessel segmentation using the 2-d gabor wavelet and supervised classification. *Medical Imaging, IEEE Transactions on*, 25(9):1214–1222. 47, 57, 58, 61

- [Sopharak et al., 2008] Sopharak, A., Uyyanonvara, B., Barman, S., and Williamson, T. (2008). Automatic detection of diabetic retinopathy exudates from non-dilated retinal images using mathematical morphology methods. *Computerized medical imaging and graphics*, 32:720–727. 76, 78
- [Staal et al., 2004] Staal, J., Abràmoff, M. D., Niemeijer, M., Viergever, M. A., and van Ginneken, B. (2004). Ridge-based vessel segmentation in color images of the retina. *Medical Imaging, IEEE Transactions on*, 23(4):501–509. 46, 47, 55, 56, 57, 59, 73
- [Stapor et al., 2004] Stapor, K., Świtonski, A., Chrástek, R., and Michelson, G. (2004). Segmentation of fundus eye images using methods of mathematical morphology for glaucoma diagnosis. In *Computational Science-ICCS 2004*, pages 41–48. Springer. 76, 77, 78
- [Sun et al., 2012] Sun, K., Chen, Z., and Jiang, S. (2012). Local morphology fitting active contour for automatic vascular segmentation. *Biomedical Engineering, IEEE Transactions on*, 59(2):464–473. 37
- [Tang et al., 2006] Tang, Y., Li, X., von Freyberg, A., and Goch, G. (2006). Automatic segmentation of the papilla in a fundus image based on the cv model and a shape restraint. *Pattern Recognition, 2006. ICPR 2006. 18th International Conference on*, 1:183–186. 67
- [Thylefors et al., 1995] Thylefors, B., Negrel, A., Pararajasegaram, R., and Dadzie, K. (1995). Global data on blindness. *Bulletin of the World Health Organization*, 73(1):115. 27
- [Tian et al., 2013] Tian, J., Marziliano, P., Baskaran, M., Tun, T. A., and Aung, T. (2013). Automatic segmentation of the choroid in enhanced depth imaging optical coherence tomography images. *Biomedical optics express*, 4(3):397–411. 116

- [Van Trigt, 1853] Van Trigt, A. (1853). *Dissertatio ophthalmologica inauguralis de speculo oculi. Trajecti ad Rhenum, PW van de Weijer.* xii, 14, 15
- [Walter et al., 2002] Walter, T., Klein, J.-C., Massin, P., and Erginay, A. (2002). A contribution of image processing to the diagnosis of diabetic retinopathy: Detection of exudates in color fundus images of the human retina. *IEEE Transactions on Medical Imaging*, 21(10):1236–1243. 75, 76, 78
- [Wang et al., 2015a] Wang, C., Kaba, D., and Li, Y. (2015a). Level set segmentation of optic discs from retinal images. *Journal of Medical and Bioengineering Vol*, 4(3). 64
- [Wang and Li, 2016] Wang, C. and Li, Y. (2016). Blood vessel segmentation from retinal images using the level set method. (Under Review). 46
- [Wang et al., 2015b] Wang, C., Wang, Y., Kaba, D., Wang, Z., Liu, X., and Li, Y. (2015b). Automated layer segmentation of 3d macular images using hybrid methods. In *Image and Graphics*, pages 614–628. Springer. 81
- [Wang et al., 2015c] Wang, C., Wang, Y., Kaba, D., Zhu, H., Lv, Y., Wang, Z., Liu, X., and Li, Y. (2015c). Segmentation of intra-retinal layers in 3d optic nerve head images. In *Image and Graphics*, pages 321–332. Springer. 102
- [Wang et al., 2016] Wang, C., Wang, Y., and Li, Y. (2016). Automatic choroidal layer segmentation using markov random field and level set method. (Under Review). 115
- [Wang, 2012] Wang, Q. (2012). Gmm-based hidden markov random field for color image and 3d volume segmentation. *arXiv preprint arXiv:1212.4527*. 106
- [Welfer et al., 2013] Welfer, D., Scharcanski, J., and Marinho, D. R. (2013). A morphologic two-stage approach for automated optic disk detection in color eye fundus images. *Pattern Recognition Letters*, 34(5):476–485. 76, 77, 78

- [Wong et al., 2008] Wong, D., Liu, J., Lim, J., Jia, X., Yin, F., Li, H., and Wong, T. (2008). Level-set based automatic cup-to-disc ratio determination using retinal fundus images in argali. In *Engineering in Medicine and Biology Society, 2008. EMBS 2008. 30th Annual International Conference of the IEEE*, pages 2266–2269. IEEE. 66
- [Wong et al., 2004] Wong, T. Y., Shankar, A., Klein, R., Klein, B. E., and Hubbard, L. D. (2004). Prospective cohort study of retinal vessel diameters and risk of hypertension. *bmj*, 329(7457):79. 2
- [Xu and Prince, 1998] Xu, C. and Prince, J. L. (1998). Snakes, shapes, and gradient vector flow. *Image Processing, IEEE Transactions on*, 7(3):359–369. 125
- [Xu et al., 2007] Xu, J., Chutatape, O., Sung, E., Zheng, C., and Chew Tec Kuan, P. (2007). Optic disk feature extraction via modified deformable model technique for glaucoma analysis. *Pattern recognition*, 40(7):2063–2076. 66
- [Yang et al., 2015] Yang, X., Gao, X., Tao, D., Li, X., and Li, J. (2015). An efficient mrf embedded level set method for image segmentation. *IEEE transactions on image processing: a publication of the IEEE Signal Processing Society*, 24(1):9–21. 121
- [Yazdanpanah et al., 2009] Yazdanpanah, A., Hamarneh, G., Smith, B., and Sarunic, M. (2009). Intra-retinal layer segmentation in optical coherence tomography using an active contour approach. In *International Conference on Medical Image Computing and Computer-Assisted Intervention*, pages 649–656. Springer. 71
- [Yazdanpanah et al., 2011] Yazdanpanah, A., Hamarneh, G., Smith, B. R., and Sarunic, M. V. (2011). Segmentation of intra-retinal layers from optical coherence tomography images using an active contour approach. *Medical Imaging, IEEE Transactions on*, 30(2):484–496. 83

- [Yuan et al., 2010] Yuan, J., Bae, E., Tai, X.-C., and Boykov, Y. (2010). A continuous max-flow approach to potts model. In *Computer Vision–ECCV 2010*, pages 379–392. Springer. 92, 93
- [Zana and Klein, 2001] Zana, F. and Klein, J.-C. (2001). Segmentation of vessel-like patterns using mathematical morphology and curvature evaluation. *Image Processing, IEEE Transactions on*, 10(7):1010–1019. 46
- [Zhang et al., 2010] Zhang, B., Zhang, L., Zhang, L., and Karray, F. (2010). Retinal vessel extraction by matched filter with first-order derivative of gaussian. *Computers in biology and medicine*, 40(4):438–445. 57, 58
- [Zhang et al., 2001] Zhang, Y., Brady, M., and Smith, S. (2001). Segmentation of brain mr images through a hidden markov random field model and the expectation-maximization algorithm. *Medical Imaging, IEEE Transactions on*, 20(1):45–57. 104, 121
- [Zhao et al., 1996] Zhao, H.-K., Chan, T., Merriman, B., and Osher, S. (1996). A variational level set approach to multiphase motion. *Journal of computational physics*, 127(1):179–195. 54
- [Zhao et al., 2015] Zhao, Y., Rada, L., Chen, K., Harding, S., and Zheng, Y. (2015). Automated vessel segmentation using infinite perimeter active contour model with hybrid region information with application to retina images. 37, 47, 57, 59
- [Zhu et al., 2010] Zhu, H., Crabb, D. P., Schlottmann, P. G., Ho, T., and Garway-Heath, D. F. (2010). Floatingcanvas: quantification of 3d retinal structures from spectral-domain optical coherence tomography. *Optics express*, 18:24595–24610. 83
- [Zhu and Rangayyan, 2008] Zhu, X. and Rangayyan, R. M. (2008). Detection of the optic disc in images of the retina using the hough transform. In *Engineering in Medicine and Biology Society, 2008. EMBS 2008. 30th Annual International Conference of the IEEE*, pages 3546–3549. IEEE. 65